

---

A CABLE ACTUATED FLEXIBLE DIGIT WITH TACTILE FEEDBACK FOR USE IN  
CLINICAL APPLICATIONS

PAUL STEPHEN SLACK

Master of Philosophy

ASTON UNIVERSITY

December, 2004

This copy of the thesis has been supplied on condition that anyone who consults it is understood to recognise that its copyright rests with its author and that no quotation from the thesis and no information derived from it may be published without proper acknowledgement.

---

**ASTON UNIVERSITY**

**THESIS SUMMARY**

**A CABLE ACTUATED FLEXIBLE DIGIT WITH TACTILE FEEDBACK FOR  
USE IN CLINICAL APPLICATIONS**

**by Paul Stephen Slack**

**Master of Philosophy**

**2004**

Much development has been initiated in the past few years with the improvement in micro-technologies and sensing techniques. These methods have been applied to a cable actuated flexible digit which has been designed in an effort to further develop upon the existing need for sensory feedback in surgical procedures. The shape of the device is controlled by strain gauge sensors mounted along an internal stiffening member. The system controller has been developed using Robust H-infinity synthesis pertaining to typical frequencies during surgical procedures. Neural networks that are able to predict load positions along the digit have been constructed for both the non-actuated and actuated systems, thus providing the ability for the surgeon to detect tissue properties in Minimally Invasive Surgical procedures. Both systems proved extremely accurate in their predictions at low frequencies, suggesting that the prediction efficiency might be comparable for other surface parameters and at higher frequencies in other non-medical applications.

**Keywords:** Haptics, Minimally Invasive Surgery, H-infinity, Neural Network

---

## **ACKNOWLEDGMENTS**

First, I would like to thank Professor Peter N. Brett for providing me with the opportunity to work on such a highly innovative project, and for his guidance and support in its development. I would also like to thank Professor Barrie Jones and Dr. Jaroslav Svoboda for their encouragement to study at Aston University. Finally, I would like to acknowledge the help that I received from all my colleagues in the Medical Engineering and Dynamics and Controls Research Groups for providing ideas and a stimulating research environment.

This project has been funded by the Commonwealth Scholarship Commission.

---

## TABLE OF CONTENTS

<b>1</b>	<b>Introduction.....</b>	<b>12</b>
1.1	Overview .....	12
1.2	Thesis Outline.....	13
1.3	Background of Distributive Tactile Sensing .....	14
<b>2</b>	<b>Cable Actuated Flexible Digit Design .....</b>	<b>16</b>
2.1	System Requirements.....	16
2.2	System Design .....	18
2.2.1	Sectional Supports .....	21
2.2.2	Stiffening Member.....	22
2.2.3	Mounting Base Design .....	22
2.2.4	Motor Bracket .....	22
2.2.5	Motor Standoff.....	23
2.2.6	Motor Pulley and Cable Guide.....	23
2.2.7	Outer Housing .....	23
2.3	Sensing Methods and Installation .....	23
2.3.1	Strain Gauge Sensors.....	24
2.3.2	Sensor Installation .....	27
2.4	Actuator Selection.....	28
2.5	System Assembly.....	30
2.5.1	Strain Gauge Amplifier.....	30
2.5.2	Data Acquisition.....	31
2.5.3	Servo Driver Board.....	31
<b>3</b>	<b>Modeling of the Flexible Digit System .....</b>	<b>33</b>
3.1	Modeling of the Flexible Digit .....	34
3.1.1	Theoretical Modeling of the Digit.....	35
3.1.2	Experimental Modeling of the Digit.....	39
3.2	Modeling of the Actuator .....	43
3.2.1	Open Loop Theoretical Modeling of the Actuator.....	44

---

3.2.2	Motor Model (without Inertial Disc and Internal Gears).....	44
3.2.3	Motor & Inertial Disc Model .....	46
3.2.4	Closed Loop Experimental Modeling of the Actuator .....	48
3.3	Cable Modeling.....	53
3.4	Conversion Coefficients .....	56
3.4.1	K1 Derivation.....	56
3.4.2	K2 Derivation.....	60
3.4.3	K3 Derivation.....	62
3.5	Flexible Digit System Model (Strain Gauge #1) .....	64
3.6	Discussion.....	67
<b>4</b>	<b>Controller Design .....</b>	<b>68</b>
4.1	$H_\infty$ Control Overview.....	70
4.2	System Analysis.....	72
4.3	Design of Controller (SISO).....	75
4.4	Nominal $H_\infty$ Synthesis ( $\Delta = 0$ ) .....	77
4.5	Analysis of $T_{yw}$ and $T_{uw}$ transfer functions .....	81
4.6	Robustness Analysis ( $\Delta \neq 0$ ) .....	83
4.7	Alternative Filters Analysis .....	85
4.8	Discussion.....	88
<b>5</b>	<b>Digital Controller Design .....</b>	<b>89</b>
5.1	Digital Controller Design .....	91
5.1.1	Trapezoidal method .....	91
5.1.2	State Space Method .....	93
5.2	Implementation of the Digital Controller .....	95
5.3	Discussion.....	97
<b>6</b>	<b>Tactile Sensing of the Non-Actuated Digit .....</b>	<b>98</b>
6.1	Creating the Neural Network.....	99
6.2	Neural Networks .....	100
6.2.1	Neural Network Strategies.....	100

---

---

6.3	The Activation Function.....	103
6.4	Experimental Explanation .....	104
6.5	Load Positions and Weights .....	105
6.6	Data Normalization .....	107
6.7	Data Optimization .....	109
6.8	Training the Neural Network.....	110
6.9	Testing of the Optimized Network.....	113
6.10	Discussion.....	115
<b>7</b>	<b>Tactile Sensing of the Actuated Digit.....</b>	<b>116</b>
7.1	Experimental Explanation .....	118
7.2	Load Positions and Weights .....	119
7.3	Data Normalization .....	121
7.4	Training the Neural Network.....	122
7.5	Testing of the Optimized Network.....	124
7.6	Discussion.....	126
<b>8</b>	<b>Conclusion .....</b>	<b>127</b>
	<b>References.....</b>	<b>129</b>
	<b>Appendix A: Nomenclature .....</b>	<b>132</b>
	<b>Appendix B: Flexible Digit Mechanical Drawings .....</b>	<b>135</b>
	<b>Appendix C: Alternative Motor Selection .....</b>	<b>139</b>
	<b>Appendix D: PCI-DAS1602/16 Connector Diagram.....</b>	<b>140</b>
	<b>Appendix E: Trapezoidal Method .....</b>	<b>141</b>

---

---

## LIST OF FIGURES

<b>Figure 1.1,</b> Flexible Digit Layout.....	13
<b>Figure 2.1,</b> Dario's Arthroscope [16] .....	17
<b>Figure 2.2,</b> Flexible Digit Assembly .....	19
<b>Figure 2.3,</b> Strain Gauge in $\frac{1}{4}$ Bridge Configuration .....	26
<b>Figure 2.4,</b> Strain Gauge in $\frac{1}{2}$ Bridge Configuration .....	26
<b>Figure 2.5,</b> Strain Gauge in Full Bridge Configuration.....	26
<b>Figure 2.6,</b> Strain Gauge Position .....	27
<b>Figure 2.7,</b> Preliminary Torque Measurement Experiment .....	28
<b>Figure 2.8,</b> MILINST (#1-904) Servo Driver Board.....	32
<b>Figure 3.1,</b> Flexible Digit Layout.....	34
<b>Figure 3.2,</b> Flexible Digit Amplification Diagram.....	34
<b>Figure 3.3,</b> Flexible Digit Section Model .....	35
<b>Figure 3.4,</b> Flexible Digit Element.....	36
<b>Figure 3.5,</b> Flexible Digit's Pole-Zero and Bode Plots .....	41
<b>Figure 3.6,</b> Validation Plot of Measured versus Modeled.....	42
<b>Figure 3.7,</b> Motor Model .....	44
<b>Figure 3.8,</b> Armature Controlled Motor Model .....	45
<b>Figure 3.9,</b> Motor & Inertial Disc Model .....	46
<b>Figure 3.10,</b> Motor & Inertial Disc Model.....	47
<b>Figure 3.11,</b> Motor Step Response (Red –Experimental / Blue – Average).....	48
<b>Figure 3.12,</b> Modeled Validation Plot .....	49
<b>Figure 3.13,</b> Motor Range (0 - 219°) .....	50
<b>Figure 3.14,</b> Motor Pole-Zero and Bode Plots .....	52
<b>Figure 3.15,</b> Cable Tension Applied to Endoscope.....	53
<b>Figure 3.16,</b> Overall System .....	56
<b>Figure 3.17,</b> Strain Gauge Voltage vs Motor Angular Position Plot(red – fitted line) ....	62
<b>Figure 3.18,</b> Pole-Zero and Bode plot of the Plant Transfer Function G(s) .....	66
<b>Figure 4.1,</b> Bode Magnitude Plot of Closed Loop System without Controller.....	73

---

<b>Figure 4.2,</b> Bode Magnitude Plot of Plant Model .....	73
<b>Figure 4.3,</b> Root Locus Plot of Closed Loop System without Controller .....	73
<b>Figure 4.4,</b> Root Locus Plot of Plant Model .....	73
<b>Figure 4.5,</b> Singular Value Plot for $F(s)$ .....	76
<b>Figure 4.6,</b> Block Diagram of System Including $F(s)$ .....	76
<b>Figure 4.7,</b> Nominal System $P$ , Including $F(s)$ .....	76
<b>Figure 4.8,</b> Block Diagram of Nominal System $P$ .....	77
<b>Figure 4.9,</b> Root Locus Plot of the Controller.....	79
<b>Figure 4.10,</b> Singular Value Plot of the Controller .....	79
<b>Figure 4.11,</b> Exploded Pole-Zero Plots of the Plant and Controller .....	79
<b>Figure 4.12,</b> Singular Value Plot of $T_{zw}$ .....	80
<b>Figure 4.13,</b> Singular Value Plot of $T_{yw}$ .....	82
<b>Figure 4.14,</b> Singular Value Plot of $T_{uw}$ .....	82
<b>Figure 4.15,</b> Step Response of Closed Loop System $T_{yw}$ .....	82
<b>Figure 4.16,</b> Step Response of Closed Loop System $T_{uw}$ .....	82
<b>Figure 4.17,</b> Block Diagram of Nominal System ( $P,C$ ) .....	83
<b>Figure 4.18,</b> Singular Value Plot for $T_{pq}$ .....	84
<b>Figure 4.19,</b> $T_{uw}$ plot for 5Hz (0.85% error tolerance).....	85
<b>Figure 4.20,</b> $T_{uw}$ plot for 0.50 Hz(0.78% error tolerance).....	85
<b>Figure 4.21,</b> $T_{uw}$ plot for 39 Hz (22.48% error tolerance).....	85
<b>Figure 4.22,</b> $T_{uw}$ plot for 50 Hz (2.6% error tolerance).....	85
<b>Figure 4.23,</b> Root Locus Plot of the Controller.....	87
<b>Figure 4.24,</b> Singular Value Plot of the Controller .....	87
<b>Figure 5.1,</b> Block Diagram Representation of the Overall System.....	90
<b>Figure 5.2,</b> Trapezoidal Approximation of Digital Controller.....	91
<b>Figure 5.3,</b> Step Response of Closed Loop System with Digital Controller .....	92
<b>Figure 5.4,</b> Step Response Comparison of Closed Loop System Comparison.....	92
<b>Figure 5.5,</b> Step Response of Digital Controller (0.6 ms – 5 ms Sampling Times).....	94
<b>Figure 5.6,</b> Step Response of Digital Controller (1 ms – 10 ms Sampling Times).....	94
<b>Figure 5.7,</b> Step Response Comparison.....	95
<b>Figure 6.1,</b> Standard steps for implementing a neural network .....	100

---

---

<b>Figure 6.2,</b> A Combined Neural Network to predict three output parameters.....	101
<b>Figure 6.3,</b> A Parallel Neural Network (three nets to predict three output parameters).	101
<b>Figure 6.4,</b> Cascaded Neural Network (three nets to predict three output parameters) .	101
<b>Figure 6.5,</b> Hyperbolic Tangent Activation Function .....	103
<b>Figure 6.6,</b> Linear Saturated Activation Function.....	103
<b>Figure 6.7,</b> Load Configurations .....	105
<b>Figure 6.8,</b> Load positions along the flexible digit .....	106
<b>Figure 6.9,</b> Non-Normalized data for all the strain gauges, loads, and load position ...	108
<b>Figure 6.10,</b> Normalized data for all the strain gauges, loads and load position .....	108
<b>Figure 6.11,</b> Examples of Trained Networks .....	109
<b>Figure 6.12,</b> Neural Network Back Propagation Training Scheme.....	110
<b>Figure 6.13,</b> Error against iterations for 15 nodes, 50 epochs .....	111
<b>Figure 6.14,</b> Error for 5 to 60 hidden nodes.....	111
<b>Figure 6.15,</b> Error for 10-20 hidden nodes .....	111
<b>Figure 6.16,</b> Error for Learning Gradient between $10^{-1}$ - $10^{-9}$ .....	111
<b>Figure 6.17,</b> Predicted and Actual Test Data for Position determination.....	113
<b>Figure 6.18,</b> Percentage Error between the Actual and Predicted Test Data.....	113
<b>Figure 7.1,</b> Load Configurations .....	119
<b>Figure 7.2,</b> Load positions along the Flexible Digit.....	120
<b>Figure 7.3,</b> Non-Normalized data for all the strain gauges, loads, and load position ....	121
<b>Figure 7.4,</b> Error against iterations for 20 nodes, 50 epochs .....	122
<b>Figure 7.5,</b> Error for 5 to 60 hidden nodes.....	122
<b>Figure 7.6,</b> Error for 15-25 hidden nodes .....	123
<b>Figure 7.7,</b> Error for Learning Gradient between $10^{-1}$ - $10^{-9}$ .....	123
<b>Figure 7.8,</b> Predicted and Actual Test Data for Position determination.....	124
<b>Figure 7.9,</b> Percentage Error between the Actual and Predicted Test Data.....	124
<b>Figure B.1,</b> End Section.....	135
<b>Figure B.2,</b> End Clamp .....	135
<b>Figure B.3,</b> Mid Section.....	136
<b>Figure B.4,</b> Mounting Base .....	136
<b>Figure B.5,</b> Motor Bracket.....	137
<b>Figure B.6,</b> Motor Spacer .....	137

---

---

<b>Figure B.7, Cable Guide</b> .....	138
<b>Figure B.8, Motor Pulley</b> .....	138
<b>Figure D.1, PCI-DAS1602/16 Connector Diagram [29]</b> .....	140

---

## LIST OF TABLES

<b>Table 2.1,</b> Assembly Bill of Materials.....	20
<b>Table 2.2,</b> Data Acquisition Card Connection Detail.....	31
<b>Table 2.3,</b> Servo Connection Detail.....	32
<b>Table 3.1,</b> Derived parameters from endoscope release tests (without housing).....	40
<b>Table 3.2,</b> Derived parameters from endoscope release tests (with housing).....	40
<b>Table 3.3,</b> System Parameters .....	44
<b>Table 3.4,</b> Motor Position and theoretical digit deflection for each strain gauge .....	57
<b>Table 3.5,</b> Strain Gauge Location (measured from the base of the digit).....	58
<b>Table 3.6,</b> Motor Position and Experimental digit deflection for each strain gauge .....	58
<b>Table 3.7,</b> System Parameters .....	61
<b>Table 4.1,</b> Poles of the Closed and Open Loop Systems .....	74
<b>Table 4.2,</b> Pole and Transmission Zeros for the Controller .....	78
<b>Table 4.3,</b> Controller Poles and Transmission Zeros.....	87
<b>Table 6.1,</b> Position and Load Combinations .....	106
<b>Table 7.1,</b> Position and Load Combinations .....	120

---

## Chapter 1

### 1 Introduction

Much development has been done in the last 30 years [1] with respect to minimally invasive surgical (MIS) procedures. The benefits are unmistakable with less patient trauma, smaller incisions, less pain, shorter healing periods, reductions in the length of stay, lower costs, and reduced blood loss [2]. Development into surgical robotics procedures and predictive surgery furthers conventional methods with less patient injuries, faster operating times, and lead to more accurate diagnosis. Immerging technologies now complement existing surgical tools and offer methods of tactile feedback with the use of micro-sensors and micro-machining techniques. Whereas these methods used to be costly, they have now become quite affordable. These new smart systems assist and complement the surgeon's skills by offering better performance. The motivation for this thesis was to improve on existing MIS systems, by developing a method capable of detecting contact on a device that resembles an endoscope.

#### 1.1 Overview

A flexible digit with a sense of tactile feedback has been developed. The integrated system allows surgeon's to have a better perception of the operating environment. The device resembles and functions as does the tip of an endoscope, but improves on existing systems with the incorporation of sensors along its member that provide a sense of feeling and shape.

The mechanism for bending is a tensioned cable that creates a bending moment at the tip of a three section digit. The stiffening constraint incorporates pieces of spring steel within each digit section to counteract the bending moment. Strain gauges are positioned along the stiffening member (see **Figure 1.1**) and used as tactile sensing points.

The device was designed and manufactured as per the requirements of the system. Each of the components were modeled individually and combined in order to develop a suitable controller able to use the sensor's deflection as feedback. The system was

---

subjected to a series of tests which led to the creation of a suitable neural network. This network was able to predict the load position along the member's surface, thereby providing potential for discriminating against distributed loads and shapes.

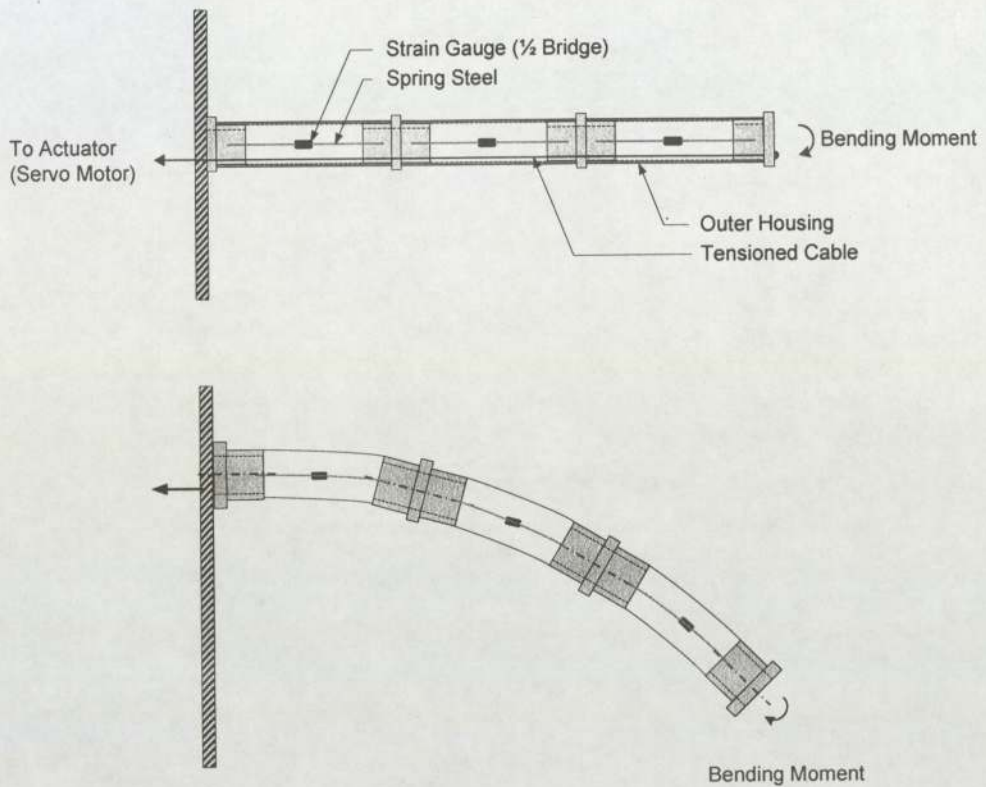


Figure 1.1, Flexible Digit Layout

## 1.2 Thesis Outline

The goal of this thesis is to design, develop and implement a device resembling an endoscope that mimics a human digit, and that incorporates a novel method of tactile feedback. The thesis has been organized in the following fashion:

- Chapter 2 outlines the system requirements and the design procedure.
- Chapter 3 models all components of the system individually before combining them in an overall system model.

- 
- Chapter 4 details the development of an  $H_\infty$  controller which robustly stabilizes the overall system.
  - Chapter 5 outlines the digitization procedure of the controller and its implementation.
  - Chapter 6 describes the development of a Neural Network to predict loads along the non-actuated device.
  - Chapter 7 takes the development of Chapter 6 one step further by developing a Neural Network to predict loads along an actuated device.
  - Chapter 8 concludes on all the findings from each of the thesis sections and suggests any future work that should be considered.
  -

### **1.3 Background of Distributive Tactile Sensing**

Touch and tactile sensing devices are becoming more prominent in surgical procedures. Their ability to assist the surgeon with a sense of feeling through a digital interface make them almost indispensable in today's surgical procedures. A tactile sensor is a device which measures spatial distribution forces perpendicular to a sensory area, and which is subsequently interpreted by some media [3]. These sensors are incorporated into intelligent machines to assist with teleoperation, image guidance, and pre-operative planning to mention only a few.

Most research studies conducted to date have incorporated multiple sensing devices distributed over a surface. The sensors in turn reconstruct the distributive forces over the sensory area using multiplexing methods that require strenuous computational ability. This is demonstrated by the high resolution pressure mapping systems developed by Tekscan (144 sensors per  $\text{cm}^2$ ) [4] that range from seating and positioning systems, to grasping and grip systems.

There exist many computational algorithms that can be used in distributive tactile sensing. The most prominent of these techniques include neural network and fuzzy logic. The use of a predictive neural network in clinical applications offers a means of determining the output of a highly non-linear system without the need for multiple sensing elements. Because of the complexity and non-linear nature of living tissue, neural networks are well suited for this application. They have been proven

---

successful in the prediction of outputs on a simply supported beam [5], [6], [7] by Ma and Brett. They have shown that conventional strain gauges can be incorporated on intelligent medical devices to provide sensory feedback to the surgeon.

Tongpadungrod et al. also demonstrate an approach to minimize the sensing elements without compromising efficiency [8].

Some work has already been done in the field of tactile sensing and force feedback in MIS devices. With recent developments in micro and computer technology, new sensing methods have paved the way for the widespread adoption of these improvements in existing surgical apparatus. An overview of computer integration into surgery has been presented by Dario and Taylor et al. in [9], [10]. Visual and tactile feedback is essential during surgery, and devices with this capability would prove extremely beneficial. Therefore attaching these micro-electromechanical sensors (MEMS) to the devices is the next logical step. Surveys relating the adoption of these sensors in MIS have been presented in both [11] and [12].

Unfortunately very little effort has been directed towards the development of these tactile feedback systems adapted to MIS. The majority of effort has been dedicated towards visual displays. A few successful devices have been constructed that have the ability to detect object presence, size, shape, position and distribution of force patterns, and even temperature. This derived information can further relate tissue hardness and texture. Work by Howe et al. [13] demonstrates the use of tactile and force feedback devices to detect palpations. Other work of Scilingo, Bicchi et al. described in [14], [15] has been conducted in the development of properties measurement of live tissues. The research led to the development of laparoscopic pliers which included force and position sensors.

Similar technology has been adapted to other surgical devices such as the arthroscope developed by Dario, D'Attanasio et al [16],[17], which includes cable actuated tip steering, tracking and collision detection. B.K.Y. Tam [18] has also presented a system that mimics a digit controlled by minimal sensing points and that deflects by varying internal pressure.

---

## Chapter 2

### 2 Cable Actuated Flexible Digit Design

Consider a device that resembles an endoscope that is capable of relaying tissue information to a surgeon in the form of tissue stiffness and shape detection. This would prove extremely beneficial during a surgical procedure by providing a sense of feeling and knowledge of the working environment.

The following Chapter outlines the design procedure of the cable actuated flexible digit with tactile sensing. The basic system requirements will be discussed, followed by the detail of each of the system's components. Preliminary calculations are performed that assist with the selection of the actuator, the range of motion, and sizing of the flexible digit. Any assumptions that have been made are also discussed to emphasize the design choice. The overall description of the system has been outlined as follows:

- The Flexible Digit's Design
- The Sensors
- The Actuator
- The Overall Flexible Digit's Assembly

#### 2.1 System Requirements

The cable actuated flexible digit must improve on existing systems outlined in **Section 1.3**. The objective is to design a flexible digit that would mimic an endoscope with a steerable tip. Most importantly, however, the digit should incorporate some form of tactile sensing that could measure disturbances acting along its members. Multiple sensing elements should be positioned within the digit that would provide the required feedback to control its deflection. Each would be able to detect and relay any information relating to external forces, as well as being able to sense edges and curvatures.

There are many options for steering the digit. One such method is controlling the air pressure within a hollow tube as was shown in [18]. This system, however, relies on

the member in tension, and relatively high pressures. Inserting a device such as this into the human body might cause some complications. Therefore, a cable driven option was chosen as the alternative. Dario [16] also demonstrated that a cable driven system could accomplish the task of tactile feedback. The system incorporated a series of universal joints or chains attached to one another. An actuation cable ran through guides along the edges of the joints (see **Figure 2.1**). One of Dario's objectives was to be able to measure disturbances along the digit, and to relay this information back to the surgeon or controller. He suggested Hall Effect sensors and strain gauges positioned towards the base of the steerable tip. However, the sensitivity of this system might not be as effective as if sensors were placed along the length of the steerable tip. Placing the sensors in this latter configuration would provide tactile feedback along the length of the digit, as opposed to just at the tip. The designed system should therefore attempt to improve upon Dario's method of compressing a flexible tip with cable actuation by including multiple sensing points.

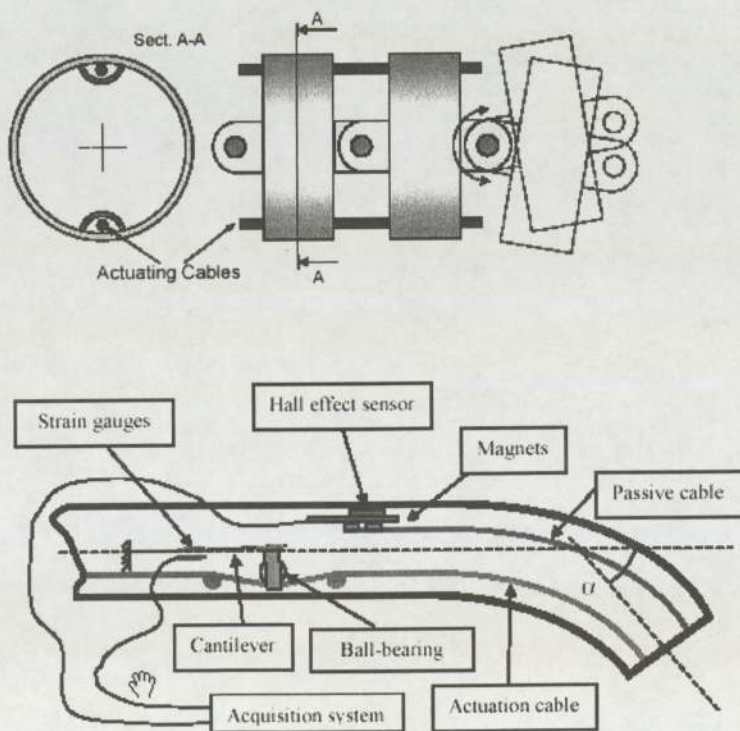


Figure 2.1, Dario's Arthroscope [16]

---

The designed member should be able to rotate in one axis, however for future designs, three axes would be desired. Because the digit would be cable actuated, it would operate in compression. For the purpose of this thesis only a single tensioned cable will be utilized, however in future designs, the system should incorporate two cable system to ensure rigidity of the member and ultimately its stability. In addition, the system should have a means of returning to its equilibrium position after actuation. This could be satisfied by including a stiffening member running through the centre of the digit.

The size of the digit would certainly constrain the possible sensing options. However, it is the proof of concept of the tactile sensing and method of control that is under study, and not the development of a medical device for surgery. Hence the size of the digit need not be restricted. In order to determine the effects that size has on the devices characteristics such as stiffness and stability, a sensitivity analysis should be conducted in the future.

Most importantly, however, the flexible digit should be designed in such a way that would ease its manufacturing and assembly, as economical as possible.

## **2.2 System Design**

A demonstrator system was manufactured to test the proof of concept. This consisted of three cables running through several guides in a bellowed tube. The cables were connected at only one side and when tensioned, caused the flexible digit to deflect in the desired direction. The demonstrator proved successful in its ability to deflect the digit in a desired direction. However, due to material selection in its construction, and dimensions chosen, the stiffness of the system was too great. The cable tensions required for movement were extremely large. Based on the findings with the demonstrator, an actual system was designed. The digit dimensions were increased and the selected materials were chosen to reduce the overall system stiffness.

---

The following section will outline the design of all components of the cable actuated flexible digit. These designs were produced using Solid Works 3D modeling package. Designing the parts virtually ensured that they were accurately dimensioned, and virtually assembled. As a result, any interference between components was observed before any manufacturing or physical assembly was performed.

In keeping with the requirements of **Section 2.1**, the flexible digit has been designed into three sections. Each section provides a maximum  $30^\circ$  of rotation, for an overall  $90^\circ$  of rotation when fully assembled. The rotation of each section was limited to  $30^\circ$  to prevent plastic deformation within the spring steel stiffening member.

**Figure 2.2** shows the Solid Works design and the actual system assembly of the flexible digit. **Table 2.1** correlates the individual parts to their thesis sections. The part drawings of each of these components are included in **Appendix B**.

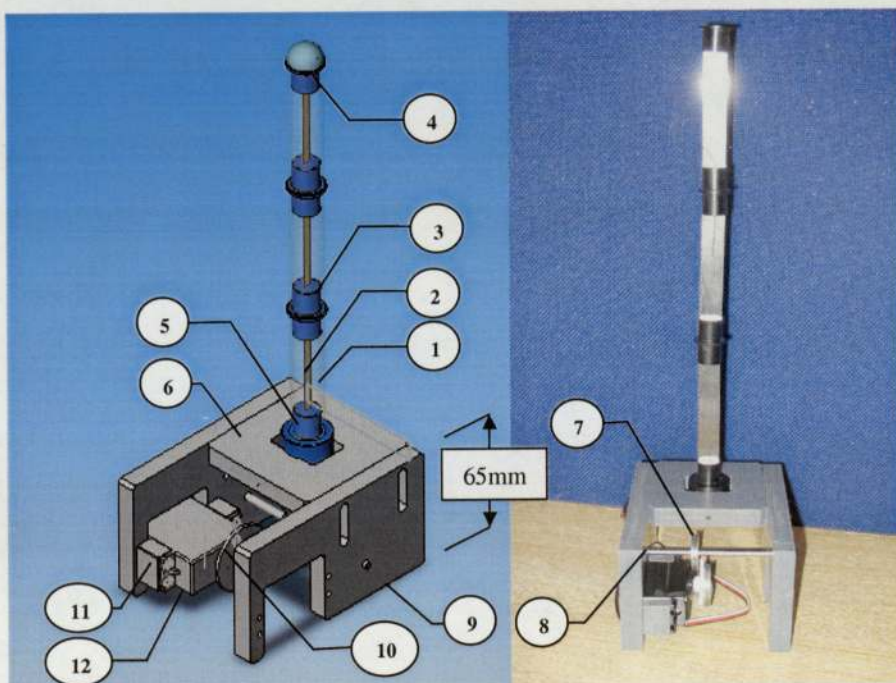


*Figure 2.2. Flexible Digit Assembly*

---

*Table 2.1, Assembly Bill of Materials*

<b>Balloon No.</b>	<b>Description</b>	<b>Section</b>
1	Outer Housing	2.2.7
2	Stiffening Member	2.2.2
3	Mid Section	2.2.1
4	End Section	2.2.1
5	End Clamp	2.2.1
6	Mounting Base	2.2.3
7	Cable Guide	2.2.6
8	Dowel Pin	
9	Motor Bracket	2.2.4
10	Motor Pulley	2.2.6
11	Motor Standoff	2.2.5
12	Actuator	2.4

---

### 2.2.1 Sectional Supports

The Mid-Sections, End Section, and End Clamp are manufactured from nylon to reduce the weight of the digit as much as possible. By reducing the weight of these components increases the natural frequency of the system, ensuring further stability. Each of the components has eight 0.042" (1.067 mm) diameter holes drilled through them. These provide guidance for the actuation cable(s) and feedback sensor wires. The outer housing, which protects the sensors from damage, is installed onto the shoulders of each section.

The End Clamp distinguishes itself from the other two members, as it is the base of the digit. Two flats have been milled on each side to facilitate clamping on the mounting base and keeping the flexible digit perpendicular with the Mounting Base.

A 0.015" (0.381 mm) slot has been cut out of the surface of each members shoulder, at a depth of 1 cm. This slot is designed for the insertion of the stiffening spring steel members. The spring steel is glued into these slots to prevent it from free floating and causing measurement inaccuracies.

---

### **2.2.2 Stiffening Member**

The stiffening member has a couple of purposes. The first is that it provides stiffness into the system, thereby increasing the natural frequency of the digit. It does so, by providing some resistance to the actuation cable. The second is that it will be the mounting surface for the sensors. Because of the nature of the digit, and that is only providing a single axis of rotation, a rectangular piece of spring steel (feeler stock) has been chosen. This stiffening member deflects around its larger axis of rotation.

A piece of spring steel is glued to each of the sectional supports within the provided slots. Each of the three sections are 8 cm long, 0.015" (0.381 mm) high and 0.5" (12.7 mm) wide. As mentioned previously, gluing prevents measurement inaccuracies, and the generation of additional twisting moments in other axes during cable actuation.

### **2.2.3 Mounting Base Design**

The mounting bases function is to fix the End Clamp by keeping its own surface perpendicular to the End Clamp's axis. It is manufactured from the same type of nylon material used for the sectional supports.

A cut-out has been milled from its centre face. This cut-out is slightly more oversized than the width of the End Clamp's flats to allow for proper alignment with the actuation cable. The positioning set screws provide the necessary adjustment for this alignment.

### **2.2.4 Motor Bracket**

The Mounting Bracket's attaches to the Mounting Base and ensures that the centre axis of the flexible digit is perpendicular to the level surface (vertical). The reason for this is to ensure that the digit does not deflect by its own weight when in its zero or equilibrium position. The Mounting Bracket is manufactured from the same type of nylon material used for the sectional supports.

The cut-outs are provided for motor clearance, and the threaded holes to each side of it, for the motor standoffs. The standoffs are necessary for the alignment of the

---

actuation cable with the flexible digit's central axis. Two slots have also been provided for tightening adjustments of the actuation cable.

### **2.2.5 Motor Standoff**

The Motor Standoff is manufactured from the same type of nylon material used for the sectional supports. The Mounting Standoffs attach to each side of the cut-out provided on the Motor Bracket. They ensure that the motor is sufficiently in line with the centre axis of the flexible digit.

### **2.2.6 Motor Pulley and Cable Guide**

The Cable Guide and Motor Pulley provide the necessary guide for the actuation cable (20 lb trace wire), and are manufactured from aluminium. The Motor Pulley attaches directly onto the servo motor, while the Cable Guide free floats on a dowel pin that fits between both Motor Brackets. One end of the actuation cable attaches to the Motor Pulley, while the other end attaches to the tip of the flexible digit.

### **2.2.7 Outer Housing**

The outer housing is made from an elastomeric material and has two purposes. The first is to protect the strain gauges from any contact, and to ensure that the wires don't get twisted or pulled. The second is to add stiffness and damping into the system which would increase the system stability. The damping would be almost non-existent without it.

## **2.3 Sensing Methods and Installation**

As explained in **Section 2.1**, there several technologies available for providing the necessary tactile feedback: Fibre-Bragg gratings, piezo-electric wires, and the conventional strain gauges. The following section introduces these options, however, concentrates mostly on the implementation of the strain gauges.

One of the issues with strain gauges versus a fibre-optic or piezo-electric counterpart is the size limitations of the overall system. The strain gauge option requires the flexible digit to be of a minimum length and diameter. Another issue is the cost.

---

Although they are quite cheap, the equipment needed to analyze the signals can bring the cost up substantially. Strain gauges are not well suited for some operating environments, which would interfere with their electrical signals. Finally the complexity of the setup for strain gauges is quite high. The procedure required for installation of these devices can be quite time consuming, and a greater expertise is required for the setup as well as calibration. Sensor alternatives should therefore be examined in the future that could improve on these traits. However, for the purpose of this thesis, it was only to demonstrate whether it was possible to discriminate and predict loads. Strain gauges are readily available, and therefore have been chosen for this application.

### 2.3.1 Strain Gauge Sensors

Strain gauges are one of the most commonly used tools of electrical measurement techniques that are applied to the measurement of mechanical quantities, more specifically strain. Strain can be by definition tensile or compressive. The measuring grid of the strain gauge is embedded between two layers of plastic strips. It consists of a thin metal foil which is electrically conductive. Typically the grid is wound from wires with 15-25  $\mu\text{m}$  of diameter [19]. As the grid is distorted due to an applied force, or temperature variation, the electrical resistance of the gauge is altered. This is due to the change in cross sectional area which is inversely proportional to the resistance of the wire per unit length.

The input-output relationship of a strain gauge is expressed as the gauge factor which is defined as the change in resistance,  $R$  for a given value of strain,  $\epsilon$ .

$$(E 2.1) \quad GaugeFactor(GF) = \frac{\delta R/R}{\delta \epsilon}$$

Strain gauges are widely used in industry for many applications where strain and temperature measurements are required. They are relatively cheap and generally robust once they are bonded to the surface of the object whose displacement is to be measured. The resistance of the gauge is usually measured by a D.C. Wheatstone

---

Bridge circuit and the displacement is inferred from the bridge output measurement. The voltage measured from the change in strain is quite small. Consequently amplification of the signal is needed. The amplification stage adds to the cost of the use of the strain gauges. However, most amplifiers have low pass filters built in that filter out unwanted noise. Noise is a concern for strain gauge measurements as the change in resistance due to a strain is extremely small. It is therefore imperative to use lead wires with the lowest resistance as possible. However, the issue of electrical interference and noise from external signals arises with lower resistance wires. The strain gauge measurements are thereby very susceptible to variations within similar measurements. The sensitivity of the measurements can be improved by considering the strain gauges in Wheatstone Bridge arrangements in  $\frac{1}{2}$  bridge or full bridge configurations (see **Figure 2.4**).

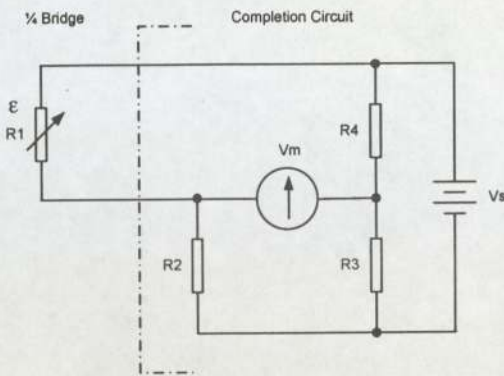


**Figure 2.3, Strain Gauge in 1/4 Bridge Configuration**

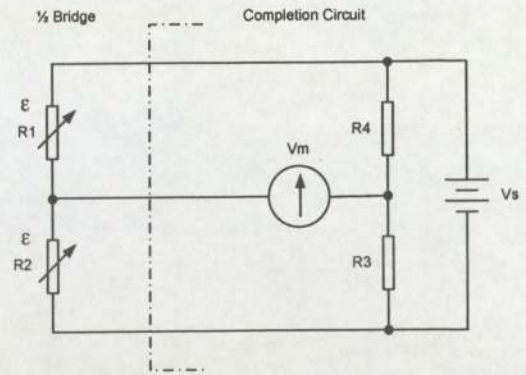


**Figure 2.4, Strain Gauge in 1/2 Bridge Configuration**

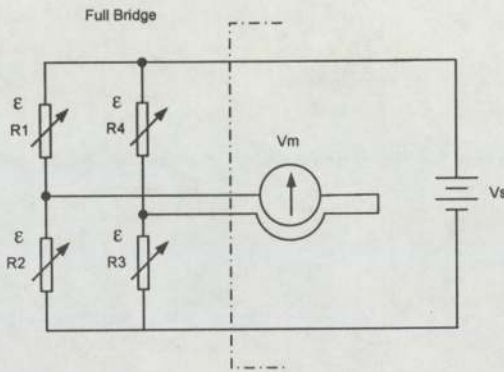


**Figure 2.5, Strain Gauge in Full Bridge Configuration**

The magnitude of the Output to Input ratio is increased in the following manner:

$$(E 2.2) \quad \frac{V_m}{V_s} = \frac{R_1 \times R_3 - R_2 \times R_4}{(R_1 + R_2)(R_3 + R_4)}$$

For the case where the circuit is in a full bridge configuration, with  $R_1 = R_3 = R + \Delta R$  &  $R_2 = R_4 = R - \Delta R$ , this ratio becomes:

$$(E 2.3) \quad \frac{V_m}{V_s} = GF \times \epsilon$$

---

Clearly we can see that if we attach gauges on opposite sides of the spring steel member, we get the compressive strain and tensile strains adding up, thereby increasing the sensitivity of the input to output ratio.

The half bridge configuration was used on the experimental system because of size constraints and strain gauge amplifier restrictions. R3 and R4 are equal, and have been set within the strain gauge amplifier. R1 and R2, on the other hand, are the resistance values of the strain gauges. This produces the following equation for this ratio of input to output:

$$(E\ 2.4) \quad \frac{V_m}{V_s} = \frac{GF}{4} \times 2\epsilon$$

### 2.3.2 Sensor Installation

With a strain gauge configuration chosen, the three sensors pairs can now be installed to the stiffening members. Two 120  $\Omega$  strain gauges were placed along each surface of all three stiffening members. Each gauge was positioned midway between the sectional supports as shown in **Figure 2.6**. The gauges were aligned in such a way so that they measure deflection along the flexible digits centre axis.



*Figure 2.6, Strain Gauge Position*

---

## 2.4 Actuator Selection

Before a motor is chosen, there are a few characteristics that must be specified. These include motor torque, desired speed of response, motor size, method of attaching to the motor shaft, motor voltage, method of motion controlling (position or velocity control), feedback method and precision, gearing, and price. Some of these specifications are not much concern for this application and therefore will not be discussed.

In order to determine the motor torque, we first need to determine what kind of load or tension in the cable is required to deflect the member to a desired angle. For this incremental loads were suspended at the end of the test rig (see **Figure 2.7**). The weight then determined the force necessary for deflection. These tests determined that a 1kg weight was just enough to rotate the demonstrator flexible digit 90 deg. This correlates to a 9.81 N force or approximately a 0.981 Nm moment arm at the end of the 10 cm digit, and a desired motor torque requirement of 1.72 Nm, assuming a torque arm of 1 cm on the motor pulley. Most small DC motors and servos specify a stall torque of less than 6 mNm. Therefore, some form of torque amplification is required in order to comply with the torque requirements, and prevent slip. A gearbox with a 300:1 ratio would clearly satisfy these requirements.

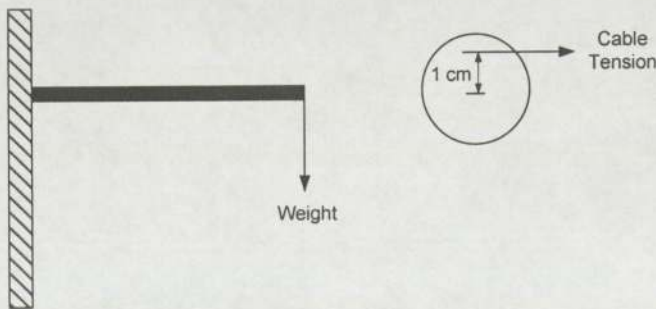


*Figure 2.7, Preliminary Torque Measurement Experiment*

When choosing the DC motor, it is necessary to determine which parameter that we wish to control: the velocity or the position. Position control is desired for this application. Therefore some method of position feedback to control the motor must be included in the design of the actuator system. Most DC motors use shaft encoders for position feedback. 1° accuracy is sufficient for this application. As such a shaft

---

encoder with approximately 500 pulses per revolution would satisfy this requirement. This corresponds to a  $0.72^\circ$  accuracy. Small servo motors used in toy cars, however, have internal circuitry designed for motor positioning using potentiometer feedback and Pulse Width Modulation (PWM). This saves the need for additional circuitry and additional components. These motors offer almost the same resolution as the DC motors, with approximately 500 positions over  $360^\circ$  of revolution.

The motor's nominal voltage has been chosen to be either 5 or 12V. The main reason for choosing this upper range is because 12 V voltage regulators are a very common. As well, most DC motors operate at around 12 V. Small servo motors available within the laboratory, however, only require 5 V. In addition several can be driven from a single servo driver board simultaneously.

The method for controlling the motor can be implemented by either developing a controller on a PIC microchip, developing the controller within MATLAB and using a data acquisition card to input and output the signals, or using an existing controller developed specifically for the motor. All of these methods are acceptable for implementing a Pulse Width Modulation (PWM) position controlled motor.

The Maxon DC motors satisfy all the requirements needed for this application, however they do cost substantially more than the conventional off the shelf servos (25 times more). The other benefit with the Maxon DC motors is that the motor characteristics will be known; whereas with the servos, the feedback control circuit and most motor characteristics are not known. However, as the objective of the thesis is to validate the proof of concept, a Futaba S-148 Servo motor (42 oz.in or 0.297 Nm of torque) has been chosen for the actuation of the flexible digit because it was readily available within the laboratory.

---

**Note:** The specification sheets for the Maxon DC Motor alternative is detailed in **Appendix C**.

---

---

## 2.5 System Assembly

All components of the system are connected in the configuration as shown in **Figure 2.2**. Tension in the cable is absolutely necessary to ensure accuracy of the desired angular position. This is achieved by the slotted screw holes attaching the Mounting Plate. The cable is attached to the Motor Pulley, wound around the Cable Guide, fed through the holes closest to the actuator on all the sectional supports, and secured at the End Section. This ensures that a positive actuation produces a bending of the digit towards the actuator. A second cable is also fed from the motor, around the Cable Guide, and through the holes farthest from the actuator. This extra cable provides extra stiffness to the system, improving the systems stability when subjected to perturbations or actuations. This cable is also secured to the End Section with a washer like device.

The wires from all six strain gauges are fed through all the sections available holes and soldered to a terminal block. Care was taken to ensure that the wires from strain gauges in the half-bridge configuration were kept together. The sensors are labeled from #1 to #3, where #1 is the pair of strain gauges closest to the End Clamp.

The flexible housing is placed over each of the three sections, and the digit calibrated to have all three sections aligned with one another in all axes, ensuring that the unit is perpendicular to the base.

### 2.5.1 Strain Gauge Amplifier

The resistance changes due to deflection of the flexible digit must be converted to a voltage so that they can be manipulated in software. Not only does it convert the resistance change to a voltage, but it amplifies the signal as well. The signals must be amplified sufficiently so that they can be read appropriately by the data acquisition card. The amplification is adjustable within the strain gauge amplifier, and has been set to 10,000. The resistance conversion is performed with the half bridge configuration described in **Section 2.3.1**.

---

The Fylde FE-366-TA amplifier with an internal low-pass filter set to a cut-off frequency of 470 Hz provides the necessary strain gauge amplification and bridge configuration that is required for this application.

### 2.5.2 Data Acquisition

The amplified voltage signals from each of the three  $\frac{1}{2}$  bridge configurations are connected to a 16 bit PCI-DAS1602/16 data acquisition card which has been set to accept input voltages between  $\pm 5$  V. This card which is recognized and configured within MATLAB's data acquisition toolbox, converts the analog voltage signals to digital form, so that they can be manipulated in software. The signal connection for each of the sensors pairs are described in **Table 2.2** and the connector diagram for the data acquisition card is detailed in **Appendix D**.

*Table 2.2, Data Acquisition Card Connection Detail*

Strain Gauge Amplifier	Wire Color	Data Acquisition Card	Pin #
Sensor 1	Black	Analog Input Ch 0 high	2
Sensor 2	Red	Analog Input Ch 1 high	4
Sensor 3	Brown	Analog Input Ch 2 high	6
Ground	Pink	Analog Ground	1

### 2.5.3 Servo Driver Board

The MILINST #1-904 servo driver board is, as the name suggests, a digital board that can drive up to eight servo motors at one time (see **Figure 2.8**). However, for this application, only one of its channels will be used for the actuation of the flexible digit. The driver requires a 9 V supply, and serial commands of 0 to 255 which control the pulse width sent to the servo. A serial command of 0 positions the servo in its 0° position, while a serial command of 255 positions the servo to its 180° position. The servo is attached to the 3-pin connector, whose pin-out is detailed in **Table 2.3**.

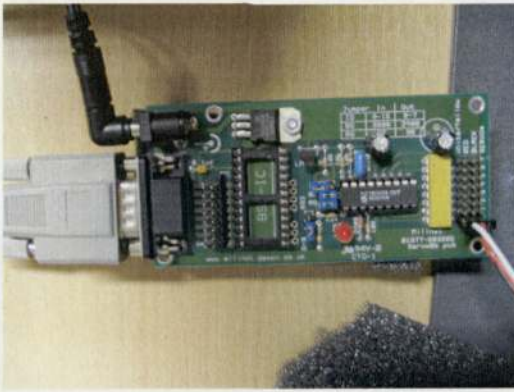


*Figure 2.8, MILINST (#1-904) Servo Driver Board*

*Table 2.3, Servo Connection Detail*

<b>Connection Colour</b>	<b>Description</b>
White	PWM control signal
Red	5 V Supply
Black	Ground

---

## Chapter 3

### 3 Modeling of the Flexible Digit System

The following Chapter outlines the modeling of the elements of the flexible cable actuated digit. Both theoretical and experimental modeling is completed for each of the sub-elements of the system. The models are transformed into the frequency domain, and combined to produce an overall open loop transfer function of the system. This is necessary for the design of the controller in **Chapter 4**.

There are essentially three components that make up the flexible digit system: the flexible digit, the actuator or the servomotor, and the cable. Each of these components are modeled separately both theoretically and experimentally. The theoretical modeling uses the equations of motion. The experimental modeling, however, uses the acquired data from the step response or release tests of the isolated sub-component from the rest of the system.

The digit beam element and the actuator are accurately modeled as second order systems. The cable, however, is modeled as a gain element, as we assume there is little or no elongation in the cable during deflection of the digit. Both the experimental and theoretical models of each sub-component are validated with their actual system to ensure the overall transfer function's uncertainty is minimized.

### 3.1 Modeling of the Flexible Digit

As presented in Section 2.3.2, the demonstrator flexible digit system has six strain gauge sensors mounted along its neutral axis; three on each side of the stiffening member. Each pair of these sensors is connected in half bridge configurations (see Figure 3.1). The sensor strain measured from a deflection of the digit is converted to a voltage potential across the bridge. This small voltage signal is then fed through a 470 Hz bandwidth low pass filter to a strain gauge amplifier. The resulting voltage signals from the amplifier are then connected to isolated input channels on the data acquisition card, and read into MATLAB. This system therefore relates the digit's deflection to a strain voltage. The signal amplification block diagram is shown in Figure 3.2.

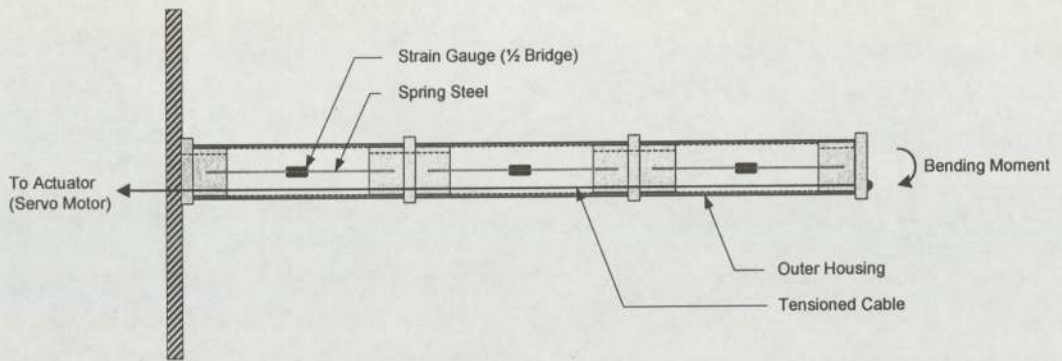


Figure 3.1, Flexible Digit Layout

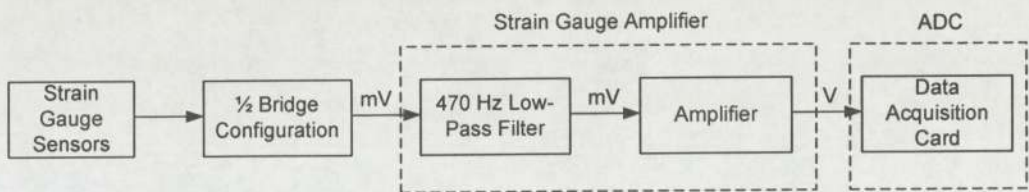


Figure 3.2, Flexible Digit Amplification Diagram

The overall objective, however, of the flexible digit model is to determine the correlation between the applied moment and the beam deflection. The maximum deflection of the beam,  $y_{\max}$ , is directly related to the moment created at the tip of the beam. This relation is derived from beam theory equations:

$$(E\ 3.1) \quad y_{\max} = \frac{Ml^2}{2EI} \quad [20]$$

As explained previously, the flexible digit beam element is modeled first theoretically. The digit is then modeled experimentally, by deflecting the beam element to a certain position and releasing it from rest. This release test produces a periodic time series, from which the dynamic parameters of the system are derived.

### 3.1.1 Theoretical Modeling of the Digit

The flexible digit can be considered for modeling purposes as a single beam fixed at one end, and free to deflect at the other (see **Figure 3.3**). The model must relate information on both the position along the beam, as well as its deflection at that point with respect to time, in order to develop a suitable controller. In addition, the model should be of a form that could be easily transferred from the time to the frequency domain. This is essential for integrating the system model within MATLAB, the tool used to develop the controller in **Chapter 4**.

The beam is considered to have a uniform cross section. The flexible digit is actuated by the cable which runs through its body. The cable is attached at one end to the servomotor and the tip of the beam at the other. Therefore as the system is actuated, a compressive force will be created at the cable attachment point. This force will be eccentric with respect to the neutral axis of the beam, and will vary depending on its curvature.

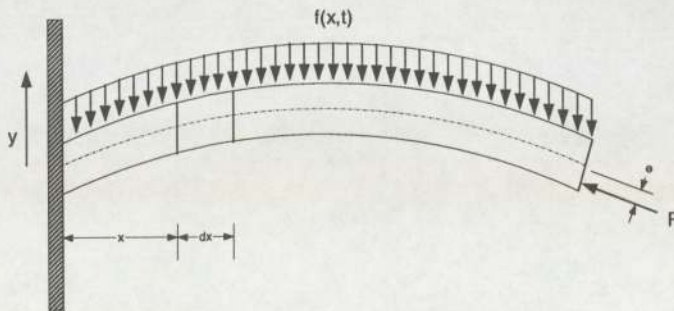


*Figure 3.3, Flexible Digit Section Model*

As a general model, we could include distributive forces,  $f(x,t)$ , acting against the beam. When dealing with the system as an endoscope, these forces could be the result of cable forces within the endoscope's walls, as well as any outside forces, such as those felt by blockages along its path. For now, however, if we neglect the distributed forces, we can apply the equations of motion with respect to an element within the beam, taking into account the shear,  $V$ , the bending moment,  $M$ , and any axial forces,  $P$  (see **Figure 3.4**).

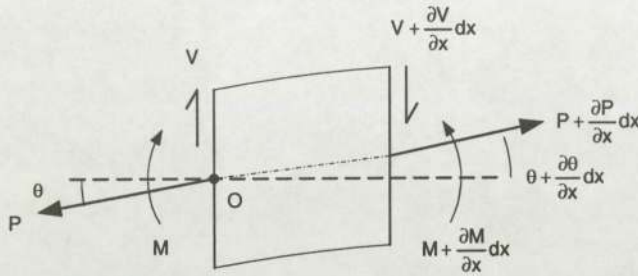


**Figure 3.4, Flexible Digit Element**

By taking the sum of forces and the sum of the moments around point "O", we end up with the following equations of motion for the endoscope element:

$$(E 3.2) \quad V - (V + dV) - P \sin \theta + (P + dP) \sin(\theta + d\theta) = \rho_m A dx \frac{\partial^2 y}{\partial t^2}$$

where  $y$  is the deflection of the beam at a certain position and time.

$$\sum M = 0 \quad \text{as there is no rotation}$$

$$(M + dM) - (V + dV)dx - M = 0$$

$$dM - Vdx - dVdx = 0$$

By assuming that  $dVdx$  is small in comparison to the other components, the following is derived,

---


$$(E 3.3) \quad \frac{dM}{dx} = V$$

In addition, assuming that we are dealing with small deflections, and from equation (E 3.2), the following equations are derived:

Recall that for small angles:

$$\left\{ \begin{array}{l} \theta \approx \sin \theta = \frac{\partial y}{\partial x} \\ d\theta = \frac{\partial \theta}{\partial x} dx \\ \quad = \frac{\partial^2 y}{\partial x^2} dx \end{array} \right.$$

$$-dV - P \frac{\partial y}{\partial x} + P \frac{\partial y}{\partial x} + P \frac{\partial^2 y}{\partial x^2} dx + dP \frac{\partial y}{\partial x} + dP \frac{\partial^2 y}{\partial x^2} dx = \rho A dx \frac{\partial^2 y}{\partial t^2}$$

Canceling terms, assuming that  $dP$  first and second derivative terms are very small, and dividing by  $dx$ , we are left with:

$$-\frac{dV}{dx} + P \frac{\partial^2 y}{\partial x^2} = \rho_m A \frac{\partial^2 y}{\partial t^2}$$

$$(E 3.4) \quad -\frac{dV}{dx} + P \frac{\partial^2 y}{\partial x^2} = \rho_m A \frac{\partial^2 y}{\partial t^2}$$

And from mechanics of a beam

$$M = EI \frac{\partial^2 y}{\partial x^2} \quad \& \quad \frac{\partial V}{\partial x} = \frac{\partial^2 M}{\partial x^2}$$

Therefore the previous equations combine with equation (E 3.4) to give

$$(E 3.5) \quad -\frac{\partial^4 y}{\partial x^4} EI + P \frac{\partial^2 y}{\partial x^2} = \rho_m A \frac{\partial^2 y}{\partial t^2}$$

---

In order to apply an appropriate controller to this model, we must first convert it into the frequency domain or s-space. This poses a challenge as the deflection  $y$  is a function of two variables: the position along the beam,  $x$ , as well as time,  $t$ . However this equation can be solved using Laplace Transforms or a separation of variables technique with the appropriate boundary and initial conditions.

#### Boundary Conditions

At  $x = 0$ ,  $y = 0$ ;

$$\left. \frac{\partial y}{\partial t} \right|_{t=0} = 0$$

#### Initial Conditions

At  $x = 0$ ,  $t = 0$  ,  $y = 0$

At  $x = L$ ,  $t = 0$ ,  $y = 0$

The solution becomes a Fourier summation, and we can clearly see from (E 3.5) that this type of modeling does not take into account damping. As a result, the simulated digit will vibrate indefinitely, when subjected to a disturbance force. A more accurate model could be derived by including the three sections as opposed to a single beam element. Experimental modeling must therefore be examined to predict the system performance more accurately.

---

### 3.1.2 Experimental Modeling of the Digit

The experimental modeling is conducted by performing release tests on the non-actuated digit with the cable removed. This requires deflecting the member to a known position and releasing it from rest. Modeling the digit in this fashion takes into account damping inherent in the system, something which had not been examined with the theoretical model. A time series is measured from the acquisition card and plotted within MATLAB. This plot of voltage (deflection) versus time provides us with a periodic plot with damping, from which the damping ratio and natural frequency of the system can be determined. These parameters characterize the system as a second order model.

The damping ratio is determined from the Percentage Overshoot (%OS) according to the following equation: [21]

$$\zeta = \frac{-\ln\left(\frac{\%OS}{100}\right)}{\sqrt{\pi^2 + \ln^2\left(\frac{\%OS}{100}\right)}}$$

The natural frequency can be approximated using the settling time of the system as well as the damping ratio determined previously. This is approximated according to the following equation: [21]

$$\omega_n = \frac{4}{T_s \zeta}, \text{ where } T_s \text{ is settling time.}$$

The settling time for the purpose of these approximations is determined as the time when the signal reaches 2% of its final value. Using these two parameters, the second order approximation of the system takes the following form: [21]

$$E(s) = \frac{\omega_n^2}{s^2 + 2\zeta\omega_n s + \omega_n^2}$$

where  $E(s)$  is the ratio of the applied moment created from deflection of the beam element, to strain voltage.

$$E(s) = \frac{V_Y(s)}{M(s)}$$

Just as a comparison, a series of release tests were conducted for two cases: first on the digit without any housing, and secondly on the digit with housing. We would expect the model of the digit with the housing to be more damped, as the housing is an elastomeric material. We would also expect the digit with housing to exhibit a slightly higher natural frequency ( $\omega_n$ ), as the stiffness of the system has been increased. The results from these tests have been tabulated in **Tables 3.1** and **3.2**.

*Table 3.1, Derived parameters from endoscope release tests (without housing)*

	%OS	$\zeta$	$\omega_d$ (rad/s)	$\omega_n$ (rad/s)
1	99.7485	0.0008	10.2033	10.2064
2	98.4458	0.0050	10.2199	10.2243
3	99.0778	0.0029	10.1016	10.1051
4	99.0893	0.0029	10.0274	10.0312
5	99.6572	0.0011	10.2432	10.2465
	Avg	0.0025		10.16271

*Table 3.2, Derived parameters from endoscope release tests (with housing)*

	%OS	$\zeta$	$\omega_d$ (rad/s)	$\omega_n$ (rad/s)
1	80.3603	0.0694	13.51803	13.5507
2	80.59.5973	0.0685	13.49483	13.5266
3	79.2905	0.0737	13.52961	13.5665
4	81.2984	0.0658	11.44893	11.4738
5	79.5477	0.0726	12.11106	12.1431
6	81.6063	0.0646	13.56471	13.5931
7	79.2594	0.0738	13.73075	13.7683
8	81.1544	0.0663	13.55301	13.5829
9	82.7165	0.0603	12.09236	12.1144
10	81.7328	0.0641	13.64718	13.6753
	Avg	0.06791		13.0995

Only the experimental data collected for the system with housing will be used for generation of the model, as this is how the system will operate when connected to the rest of the components of the flexible digit system. Based on the average of several

plots, the damping ratio and natural frequency of the isolated endoscope beam system has been found as 0.06791 and 13.0995 rad/s respectively. This provides us with the following transfer function:

$$E(s) = \frac{171.61}{s^2 + 1.782s + 171.61} \left( \frac{V}{Nm} \right)$$

We notice that the system without the housing has less damping, and a lower natural frequency. This was as predicted. **Figure 3.5** shows its bode magnitude and phase plots. The attenuation of the system appears to be around 20.3 rad/s. This indicates that most of the signal's energy is at frequencies lower than 3.23 Hz. We are interested in very low frequencies, generally below 5 Hz, thus demonstrating that this frequency is close to our range of interest.

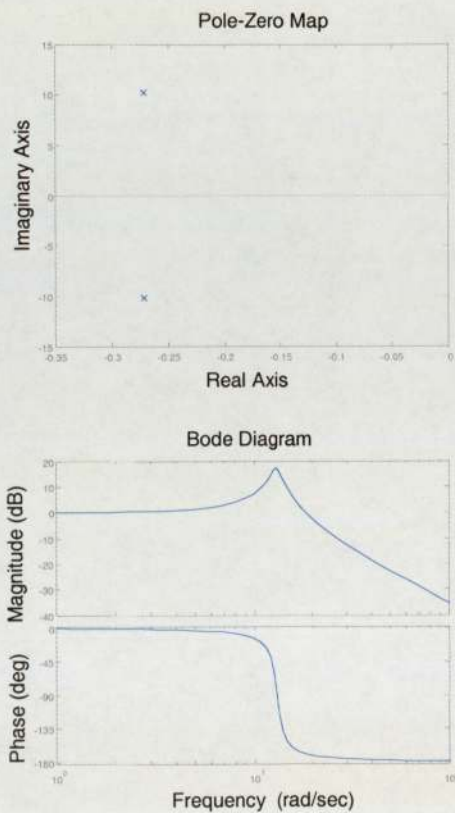


**Figure 3.5,** Flexible Digit's Pole-Zero and Bode Plots

The model for the digit with housing has been validated against the actual measured data and is shown for test #10 in **Figure 3.6**. The correlation between the two data

---

sets results in an accuracy between the actual and the modeled system of 99.10%. This was found using the “corr2” command within MATLAB. The error might be the consequence of the actual system being of higher order with non-dominant poles. However, for the purpose of modeling, it is well within acceptable limits.

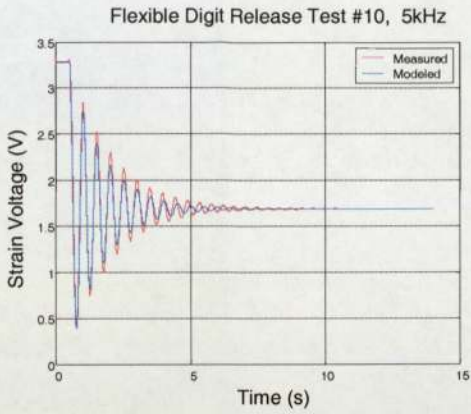


**Figure 3.6, Validation Plot of Measured versus Modeled**

---

## 3.2 Modeling of the Actuator

The following section outlines the steps taken in the modeling of the actuator for the flexible digit system. The actuator is a simple servo motor used in model airplanes and cars. The actuator has its own built in position control, which is controlled by Pulse Width Modulation (PWM). The pulse frequency is 52 Hz and the required pulse width is between 1 and 2 ms. This corresponds to between 10 and 20% of the pulse frequency.

One drawback of using this type of motor is that its angular position is controlled using internal hardware. This position control circuitry is not known, making it difficult to model theoretically. However, the feedback position measurement of the servomotor is measured using a rotary potentiometer, providing the necessary measurements to model the motor experimentally. The servomotor was altered to have three wires soldered to its contacts. The signals from these wires provide a direct relation between the voltage and the angular position of the motor.

The actuator is modeled first theoretically without any controller. Unfortunately the exact parameters of the actuator system are not known making it difficult to compare with the experimental model. However, some of these unknown parameters can be extracted from the experimental model, which will be derived thereafter.

### 3.2.1 Open Loop Theoretical Modeling of the Actuator

The open loop theoretical modeling of the actuator is presented in this section. The model generated provides a basis for establishing the relationships existing between the input voltage and the actuator angular position. The motor model is derived initially without an inertial load. However, in order to make the system more accurate, the motor model is then derived with the motor pulley (inertial load) and internal gearing.

As explained previously, the motor constants are not known. Therefore the models are derived solely with variables.

*Table 3.3, System Parameters*

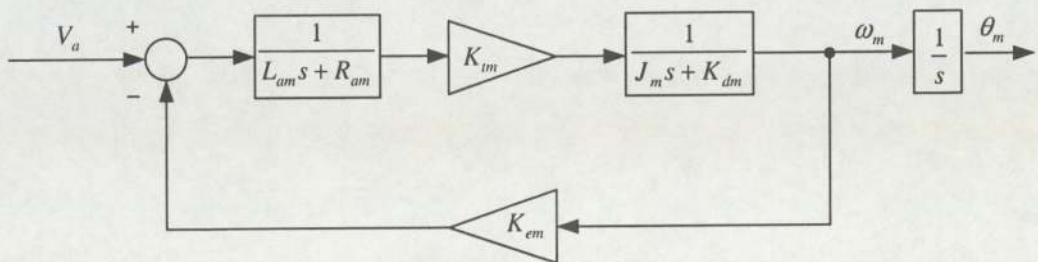
Motor		
Torque Constant	$K_{TM}$	Nm/s
Back-EMF Constant	$K_{EM}$	Nm/s
Rotor Inertia	$J_M$	$\text{kgm}^2$
Resistance	$R_{AM}$	$\Omega$
Inductance	$L_{AM}$	mH
Viscous Damping	$K_{DM}$	Nms

Inertial Disc		
Inertia	$J_{disc}$	$\text{kgm}^2$

### 3.2.2 Motor Model (without Inertial Disc and Internal Gears)

The armature controlled motor model is shown in **Figure 3.8** and the required transfer functions and equations are derived hereafter from **Figure 3.7**.



*Figure 3.7, Motor Model*

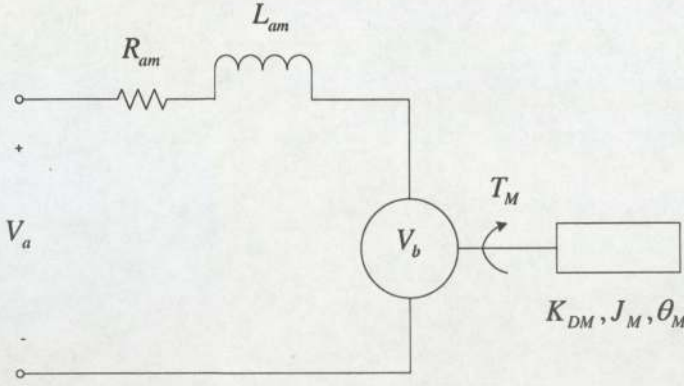


Figure 3.8, Armature Controlled Motor Model

From the block diagram of the motor model, we can determine the  $\frac{\omega_m(s)}{V_a(s)}$  and  $\frac{\theta_m(s)}{V_a(s)}$  transfer functions. These are as follows:

$$T_M(s) = K_{Tm} i_a(s)$$

$$V_b(s) = K_{Em} \omega_m(s)$$

$$i_a(s) = \frac{V_a(s) - V_b(s)}{L_a s + R_a}$$

$$\omega_m(s) = \frac{K_{Tm}}{(J_m s + K_{Dm})} \left[ \frac{V_a(s) - K_{Em} \omega_m(s)}{L_{am} s + R_{am}} \right]$$

$$\omega_m(s) [(J_m s + K_{Dm})(L_{am} s + R_{am}) + K_{Tm} K_{Em}] = K_{Tm} V_a(s)$$

$$\omega_m(s) = \frac{K_{Tm} V_a(s)}{[(J_m s + K_{Dm})(L_{am} s + R_{am}) + K_{Tm} K_{Em}]}$$

$$(E 3.6) \quad \frac{\omega_m(s)}{V_a(s)} = \frac{K_{Tm}}{(J_m s + K_{Dm})(L_{am} s + R_a) + K_{Em} K_{Tm}}$$

and

$$(E\ 3.7) \quad \frac{\theta_m(s)}{V_a(s)} = \frac{K_{Tm}}{[(J_m s + K_{Dm})(L_{am} s + R_a) + K_{Em} K_{Tm}]s}$$

### 3.2.3 Motor & Inertial Disc Model

The following section concentrates on deriving the model of the motor with inertial disc. Their equations of motion are combined and transformed into transfer functions, thereby determining the overall motor model.

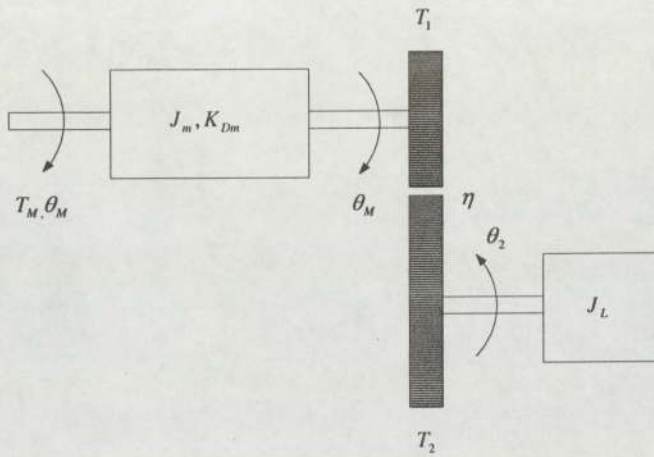


Figure 3.9, Motor & Inertial Disc Model

$$\eta N = \eta \frac{N_2}{N_1} = \eta \frac{\theta_M}{\theta_2} = \frac{T_2}{T_1}$$

$$T_M = J_m \ddot{\theta}_1 + K_{Dm} \dot{\theta}_1 + T_1$$

$$T_2 = J_L \ddot{\theta}_2 = J_L \frac{N_1}{N_2} \ddot{\theta}_1$$

Therefore

$$T_M = J_m \ddot{\theta}_1 + K_{Dm} \dot{\theta}_1 + J_L \left( \frac{N_1}{N_2} \right)^2 \frac{1}{\eta} \ddot{\theta}_1 = \left( J_m + J_L \frac{1}{\eta N^2} \right) \dot{\omega}_m + K_{Dm} \omega_m$$

The DC motor and inertial disc model is shown in **Figure 3.10** and the required transfer functions and equations are shown in (E 3.8) and (E 3.9).

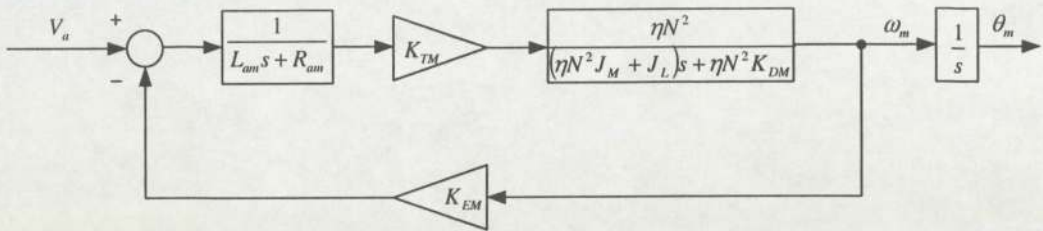


**Figure 3.10, Motor & Inertial Disc Model**

From the block diagram of the motor & Inertial Disc model, we can determine the

$\frac{\omega_m(s)}{V_a(s)}$  and  $\frac{\theta_m(s)}{V_a(s)}$  transfer functions. These are found as follows:

$$(E 3.8) \quad \frac{\omega_m(s)}{V_a(s)} = \frac{\eta N^2 K_{TM}}{\left[ (\eta N^2 J_M + J_L) s + \eta N^2 K_{DM} \right] (L_{am} s + R_{am}) + \eta N^2 K_{TM} K_{EM}}$$

$$(E 3.9) \quad \frac{\theta_m(s)}{V_a(s)} = \frac{\eta N^2 K_{TM}}{s \left[ (\eta N^2 J_M + J_{disc}) s + \eta N^2 K_{DM} \right] (L_{am} s + R_{am}) + \eta N^2 K_{TM} K_{EM}}$$

Although this model is not particularly practical for modeling of the servo motor (with PWM) used in this application, it would serve as an essential resource in modeling of a DC motor controlled by position or velocity feedback.

---

### 3.2.4 Closed Loop Experimental Modeling of the Actuator

The actuator is modeled experimentally as a closed loop system in this Section. It uses as input a PWM signal in the form of a serial pulse from MATLAB, and as output the potentiometer voltage. In essence this voltage is the angular position of the rotary potentiometer, and hence the angular position of the actuator shaft.

The signal from the potentiometer connects to one of the channels of the data acquisition card. This is required to generate a plot within MATLAB of the step response to a serial command. Several sample tests were performed, each with an input serial command of 51. The average plot created for the actuator system is shown in **Figure 3.11**. The large amount of noise in the system can be filtered partially by running the time series through a filter. Two such filtering techniques are examined: a Fast Fourier Transform (FFT), and an SVD filter.

---

Note: All filtering was done within Matlab during the acquisition of the data.

---

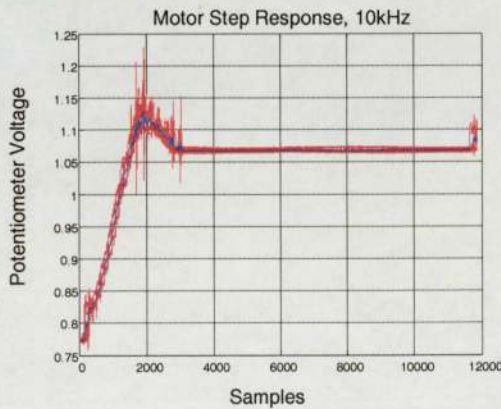


**Figure 3.11**, Motor Step Response (Red –Experimental / Blue – Average)

The Fast Fourier Transform (FFT) filtering methods overlays periodic functions to best fit the curve over the existing system. Should the “N” parameter within MATLAB be set to too large an amount, the undesired noise isn’t filtered properly, and the curve doesn’t correspond at all with the original signal. Alternatively if this parameter is set too low, more sinusoidal inaccuracies are introduced into the signal, making the plot even more irregular than the original. This is obviously undesirable.

---

The better of the two filtering methods appears to be the SVD filter. It seems to smooth out the curve adequately, without losing too much of the signal. This method relies on finding the singular values that contribute the most to the system (in our case the 2<sup>nd</sup> largest). The signal is then re-created by filtering out all other singular values of order lower than this desired cutoff.

---

Note: The spikes in the signal which seem to be inherent to the signal.

---

After some analysis of the experimental results, the damping coefficient,  $\zeta$ , is found to be 0.5629. This, like the natural frequency, was derived using the same methods discussed in **Section 3.1.2** for the flexible digit model. Essentially the damping ratio is found by examining the percentage overshoot, while the natural frequency is calculated using the settling time. The natural frequency of the system was found to be 20.53 rad/s. By considering the motor as a second order system, the overall transfer function becomes:

$$MT(s) = \frac{421.5}{s^2 + 23.11s + 421.5}$$

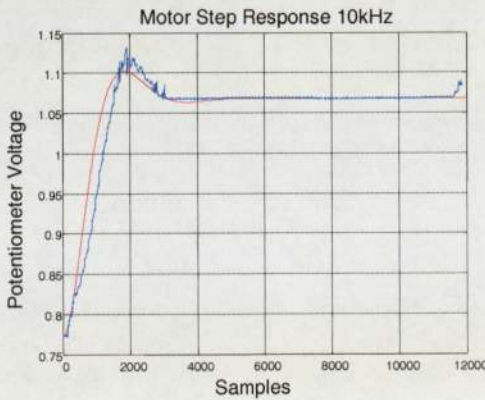


**Figure 3.12, Modeled Validation Plot**

The model for the actuator has been validated against the actual measured data and is displayed in **Figure 3.12**. The correlation between the two data sets results in an

accuracy between the actual and the modeled system of 96.81%. As with the error in the flexible digit's model, the difference between the two actuator systems can be due to the actual system being of higher order with non-dominant poles.

The  $MT(s)$  transfer function only relates the serial pulse to the potentiometer voltage. However, it is the motors angular position that is of interest. There exists a relationship between the potentiometer voltage and the angular position of the motor shaft. This is derived as follows:

$$\frac{219 * \pi / 180}{\text{Potentiometer Voltage Range}}$$

The full range of angular motion of the actuator is from 0 to 219°, which corresponds to a serial motor command of 0 and 254. **Figure 3.13** shows the relation between the motor voltage and the angular position. The motor voltage for the 0° position is 0.46688 V, and for the 219° position, 2.4755 V. The resulting relation between the angular position and the potentiometer voltage becomes:

$$\theta_M = 109.1344V_\theta - 51.162$$

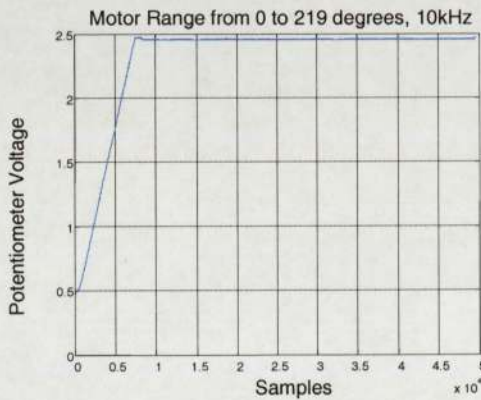


**Figure 3.13, Motor Range (0 - 219°)**

---

If we wish to transform these relations into the “s-domain”, we must first recognize that it is not a linear system. A linear system must satisfy the two following conditions of superposition and homogeneity:

$$\alpha x_1 + \beta x_2 = \alpha f(x_1) + \beta f(x_2)$$

$$f(x_1 + x_2) = f(x_1) + f(x_2)$$

Clearly this equation does not. Therefore it is imperative that it be linearized.

A system of equations can be linearized by choosing a set point or equilibrium position, and determining the slope of the curve at that position. This assumes that all points within a certain proximity of the equilibrium lie on the slope of that curve. In essence, the initial system is transformed to a new system, which is characterized by the original's derivative, thus eliminating all DC biases.

The new equation becomes:

$$(E\ 3.10) \quad \theta_M(s) = 109.1344 V_\theta(s) \quad (\text{deg.V})$$

Which leads to the following overall motor model:

$$\begin{aligned} MT(s) &= \frac{421.5}{s^2 + 23.11s + 421.5} \times 109.1344 \times \frac{\pi}{180} \\ &= \frac{802.854}{s^2 + 23.11s + 421.5} \left( \frac{\text{rad}}{\text{SerialCommand}} \right) \end{aligned}$$

---

From the pole-zero plot in **Figure 3.14**, we notice that the poles of the system lie far within the left hand plane, indicating a very stable system. The system poles essentially indicate the system is non-oscillatory, and its output to a disturbance would stabilize very quickly. The bode plot indicates that most of the energy of the system lies in frequencies below the 11.55 rad/s.

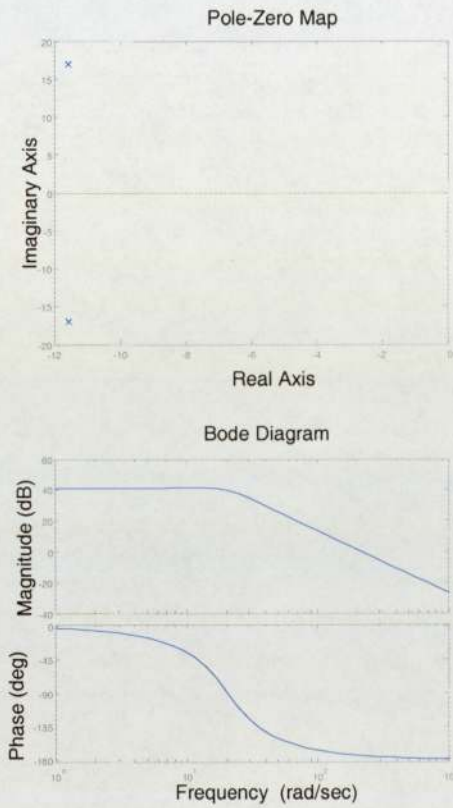


**Figure 3.14**, Motor Pole-Zero and Bode Plots

---

### 3.3 Cable Modeling

The following section outlines the modeling of the cable. The change in cable length is related to the bending moment created at the end of the endoscope. This is the result of the cable being connected on one end to the motor, and the other, to the tip of the flexible digit. The cable is considered to run the full length of the endoscope at the same eccentric distance from the neutral axis. The cable elongation can be considered negligible with respect to the digit elongation, as its stiffness is substantially greater.

If we consider that the flexible digit will deflect a certain amount due to an applied bending moment, the same can be considered in the opposite sense. A deflection in the flexible digit will create a bending moment or an eccentric force at the cable connection point. This force is the cable tension created by a change in the cable length. In other words, the cable tension is produced from the beams resistance to a deflection.

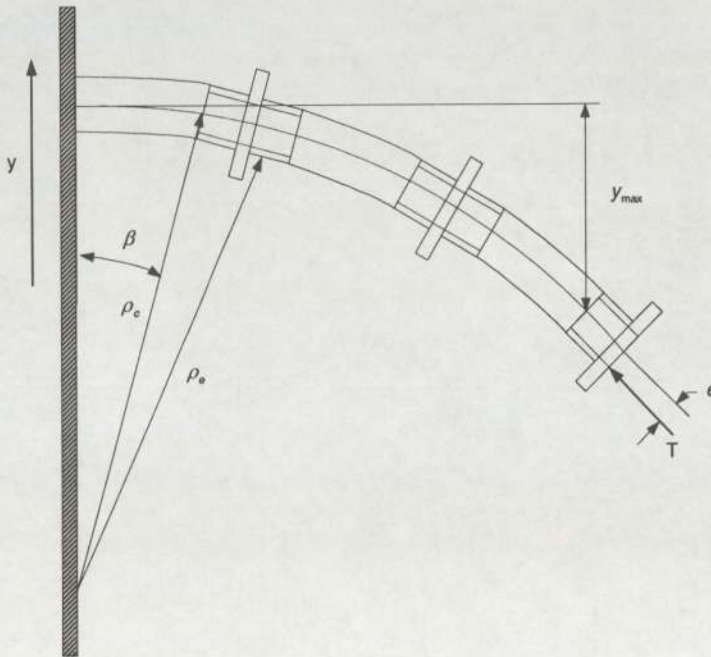


Figure 3.15, Cable Tension Applied to Endoscope

---

The cable within the endoscope chamber is shortened with the rotation of the motor shaft. The two are related as follows:

(E 3.11)  $\Delta l_M = \theta_M r_M$  where  $\Delta l_M$  is the change in cable length  
 $\theta_M$  is the change in motor angle  
 $r_M$  is the motor torque arm

$$\rho_e = \rho_c - e$$

Now for an angle  $\beta$ ,

$$\beta = \frac{l}{\rho_c} = \frac{l - \Delta l_M}{\rho_e}$$

Which becomes:

$$\frac{l}{\rho_c} = \frac{l - \Delta l_M}{\rho_c - e}$$

With a little manipulation, we get

$$\rho_c = \frac{le}{\Delta l_M}$$

Recalling that the equation for curvature is:

$$\frac{1}{\rho_c} = \frac{\frac{d^2 y}{dx^2}}{\left[1 + \left(\frac{dy}{dx}\right)^2\right]^{\frac{3}{2}}} \quad [20]$$

However for small angles  $\frac{dy}{dx} \approx 0$ , and the equation becomes:

$$\frac{1}{\rho_c} = \frac{d^2 y}{dx^2}$$

---

However, we also know that

$$(E 3.12) \quad \frac{1}{\rho_c} = \frac{M}{EI} \quad [20]$$

If we consider the flexible digit to be a beam in pure bending, we get for the general horizontal system:

$$y = \frac{Mx^2}{2EI} + \frac{w}{24EI} (x^4 - 4lx^3 + 6l^2x^2)$$

, where  $w$  is the weight of the beam

For a vertical system, as is the case for our system, this equation simplifies to:

$$y = \frac{Mx^2}{2EI}$$

However the maximum deflection occurs at the tip of the flexible digit, and this equation becomes:

$$(E 3.13) \quad y_{\max} = \frac{Ml^2}{2EI}$$

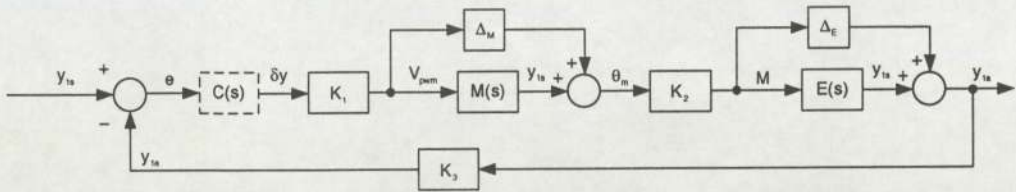
And from (E 3.12) and (E 3.13)

$$M = \frac{EI}{\rho_c} = \frac{EI\Delta l_M}{le}$$

$$(E 3.14) \quad y_{\max} = \frac{l\Delta l_M}{2e}$$

### 3.4 Conversion Coefficients

Several coefficients are required to convert between the systems transfer functions. These coefficients are the  $K_1$ ,  $K_2$  and  $K_3$  gains as shown in **Figure 3.16**, and are derived in this section based on experimental and theoretical data. The actuation cable was re-attached to both the servo motor and the flexible digits tip, in order to determine these parameters.



Note: this diagram is for the SISO case, with single strain gauge reading

Figure 3.16, Overall System

#### 3.4.1 $K_1$ Derivation

The  $K_1$  parameter describes the relationship between the motor drive commands outputted by the Matlab serial communication, and the flexible digit's deflection. This parameter was determined by measuring the full range of motion of the motor and its input commands, which in this case lie between 0 and 254. The full angular range of the motor was measured as  $219^\circ$ . This is to say that given a serial command of 0, the motor exhibits no angular rotation, whereas a serial command of 254 corresponds to an angular rotation of  $219^\circ$ .

The desired range of the motor lies between serial commands 8 and 43. This range corresponding to 0 to  $30^\circ$  of beam rotation is outputted by the Matlab serial communication program, and sent to the MILINST motor controller board. This board requires a start bit, a stop bit, and the desired serial position command. The MILINST board then sends out a constant pulse width to the servo motor based on this serial value. A 0 serial signal corresponds to 1ms pulse width (the pulse width frequency is 52Hz), whereas a 254 serial signal corresponds to a 2ms pulse width.

**Table 3.4** displays the theoretical deflection calculations for strain gauges #1 to 3, which are based on the equations from **Section 3.3**. These equations are presented again.

$$M = \frac{2EIy}{x^2}, \quad M = \frac{EI\theta_M r_M}{le}$$

and 
$$\frac{\theta_M}{\chi_{mpss}} = \frac{(219-0)}{(254-0)} = 0.8622 * \frac{\pi}{180} = 0.0150 \quad \left( \frac{\text{rad}}{\text{SerialCommand}} \right)$$

are combined to produce:

$$(E 3.15) \quad y = \frac{0.0150 r_M x^2}{2le} \Delta \chi_{mpss}$$

**Table 3.4, Motor Position and theoretical digit deflection for each strain gauge**

Desired Motor Position [0-254]	$y_{SG1}$ (mm)	$y_{SG2}$ (mm)	$y_{SG3}$ (mm)	$y_{max}$ (mm)
8	0	0	0	0
9	0.11	1.02	2.84	3.26
10	0.23	2.04	5.68	6.51
11	0.34	3.07	8.52	9.77
12	0.45	4.09	11.36	13.03
13	0.57	5.11	14.19	16.28
14	0.68	6.13	17.03	19.54
15	0.79	7.15	19.87	22.80
16	0.91	8.18	22.71	26.06
17	1.02	9.20	25.55	29.31
18	1.14	10.22	28.39	32.57
19	1.25	11.24	31.23	35.83
20	1.36	12.26	34.07	39.08
21	1.48	13.29	36.90	42.34
22	1.59	14.31	39.74	45.60
23	1.70	15.33	42.58	48.85
24	1.82	16.35	45.42	52.11

**Note:** the equilibrium position is motor position 8

*Table 3.5, Strain Gauge Location (measured from the base of the digit)*

Strain Gauge #1	45	mm
Strain Gauge #2	135	mm
Strain Gauge #3	225	mm

The same commands were issued experimentally and compared against the theoretical data. **Table 3.6** displays the experimental data, and shows the percentage error between the theoretical and experimental models. The strain gauges #2 and #3 systems are fairly similar to one another for larger deflections. The two differ at the smaller deflections because of the error associated with the resolution of the deflection measurements. The model for strain gauge #1, however, does not appear to be very accurate. This is because of the resolution of the deflection measurements and the fact that the model is based on a single section. In actuality, the digit is comprised of multiple sections.

*Table 3.6, Motor Position and Experimental digit deflection for each strain gauge*

Desired Motor Position [0-254]	$y_{SG1}$ (mm)	$y_{SG2}$ (mm)	$y_{SG3}$ (mm)	% Error SG1	% Error SG2	% Error SG3
8	0	0	0	N/A	N/A	N/A
9	0	3.5	5	N/A	70.80	43.22
10	0.5	4	6	54.58	48.90	5.37
11	0.5	5	10	31.87	38.68	14.83
12	0.5	6	14	9.16	31.87	18.89
13	0.5	7	15.5	13.55	27.00	8.42
14	0.5	8	17.5	36.26	23.35	2.67
15	0.5	8.5	20	58.97	15.84	0.64
16	0.5	9	22.5	81.69	9.16	0.94
17	0.5	10	24.5	104.40	8.02	4.28
18	0.5	10.5	27.5	127.11	2.67	3.23
19	0.5	11	29	149.82	2.20	7.68
20	0.5	11.5	32	172.53	6.64	6.46
21	0.5	13	36	195.24	2.20	2.51
22	1	14.5	39	58.97	1.33	1.91
23	1	15.5	42	70.33	1.10	1.39
24	1	16	43.5	81.69	2.20	4.42

---

$$\mathcal{X}_{mpss} = \frac{y_{SG1} + 0.4523}{0.0565}$$

$$\mathcal{X}_{mpss} = \frac{y_{SG2} + 7.2373}{0.9047}$$

$$\mathcal{X}_{mpss} = \frac{y_{SG3} + 22.164}{2.7705}$$

Linearizing and transferring these relations to transfer functions results in the following equations:

$$(E\ 3.16) \quad \mathcal{X}_{mpss}(s) = 17.6991 y_{SG1}(s)$$

$$(E\ 3.17) \quad \mathcal{X}_{mpss}(s) = 1.1053 y_{SG2}(s)$$

$$(E\ 3.18) \quad \mathcal{X}_{mpss}(s) = 0.3609 y_{SG3}(s)$$

---

### 3.4.2 K2 Derivation

The K2 parameter provides a relation between the angular position and the bending moment created by the cable tension. This relationship between the two parameters is linear, assuming the cable remains uniformly eccentric along the full length of the digit. Because we are dealing with small deflections, this assumption holds true. Therefore, as the motor rotates, the cable is shortened and deflects the flexible digit.

A change in cable length affects the curvature of the digit, and hence its deflection. The relation between the bending moment and the deflection of the digit depends on Hooke's Law. (E 3.11) demonstrates the relation between the change in cable length and the deflection; whereas (E 3.14) demonstrates the relation between the deflection and the bending moment. Combining these two equations produce:

$$M = \frac{2EIy_{\max}}{l^2} = \frac{EI\Delta l_M}{le} = \frac{EIr_M\theta_M}{le}$$

Transferring this equation into its corresponding Laplace transform produces the following:

$$M(s) = \frac{EIr_M\theta_M(s)}{le}$$

The values for the unknown parameters were calculated based on the digits dimension and inserted into the transfer function. These are outlined in

---

*Table 3.7, System Parameters*

<b>Flexible Digit Length</b>	$l$	$270 \times 10^{-3}$	m
<b>Tension Eccentricity</b>	$e$	$5.715 \times 10^{-3}$	m
<b>Inertial Disc Radius</b>	$r_m$	$11.5 \times 10^{-3}$	m
<b>Modulus of Elasticity</b>	$E$	$205 \times 10^9$	Pa
<b>Digit Moment of Inertia</b>	$I$	$5.8532 \times 10^{-14}$	$\text{m}^4$

The transfer function now becomes:

(E 3.19)  $M(s) = 0.089377 \theta_M(s)$  (Nm.rad)

---

### 3.4.3 K3 Derivation

The K3 parameter provides a relationship between the strain gauge voltage and the actual deflection of the digit. This is derived by deflecting the digit to specific desired positions, and measuring the strain gauge voltage for that position. The relation was determined in two steps. First a relation between the strain gauge voltage and the input serial pulse was determined. And secondly a relation between the deflection of the digit at the strain gauge positions and the same serial pulse was determined. The two relations are combined to produce the overall relation between the deflection and the strain gauge voltages.

Serial pulses of 8 to 24 are used for the determination of the deflection. This relation is taken from the determination of the K1 coefficient. The relation between the serial command and strain gauge voltage determined by sending serial pulses between 8 and 43 to the MILINST board and measuring the strain voltage for each strain gauges at these positions. Each new setting was allowed to settle to eliminate any transient effects. The serial value of 8 corresponds to the equilibrium position of the digit, or the position of no deflection.

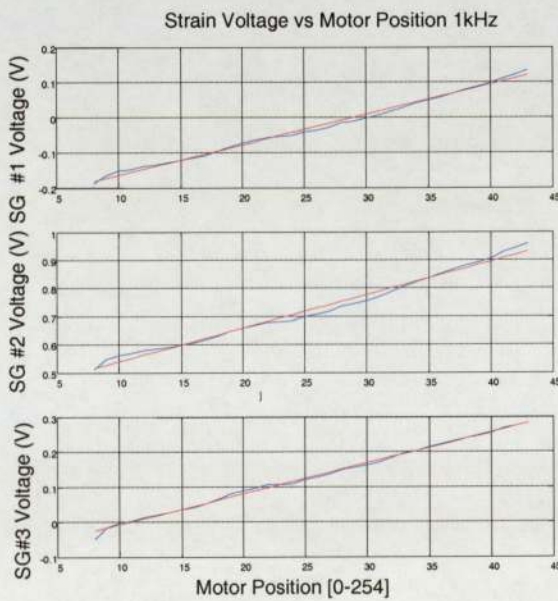


*Figure 3.17, Strain Gauge Voltage vs Motor Angular Position Plot (red – fitted line)*

---

Fitting a linear trend line to the data in **Figure 3.17** leads to the following relationships between the motor position and the strain gauge voltages:

$$(E\ 3.20) \quad V_{SG1} = 0.0086 \chi_{mpss} - 0.1896$$

$$(E\ 3.21) \quad V_{SG2} = 0.0119 \chi_{mpss} + 0.5019$$

$$(E\ 3.22) \quad V_{SG3} = 0.0088 \chi_{mpss} - 0.0357$$

Combining **(E 3.17)**, **(E 3.18)**, **(E 3.19)** with **(E 3.20)**, **(E 3.21)**, **(E 3.22)** leads to the following relations between the digits deflection and the motor's serial pulse at each strain gauge location:

$$y_{SG1} = 6.5696 V_{SG1} + 0.1246$$

$$y_{SG2} = 76.0252 V_{SG2} - 38.1571$$

$$y_{SG3} = 314.8295 V_{SG3} + 11.2394$$

Linearizing and transferring these relations to transfer functions results in the following equations:

$$(E\ 3.23) \quad y_{SG1}(s) = 6.5696 V_{SG1}(s)$$

$$(E\ 3.24) \quad y_{SG2}(s) = 76.0252 V_{SG2}(s)$$

$$(E\ 3.25) \quad y_{SG3}(s) = 314.8295 V_{SG3}(s)$$

---

### 3.5 Flexible Digit System Model (Strain Gauge #1)

The following section derives the overall system model of the flexible digit system. It is transformed into its state equations so that its stability could be analyzed. The systems transfer function is generated for only strain gauge #1.

The transfer functions of all the sub-components are combined to produce an overall transfer function of the open loop flexible digit system.

$$G(s) = K_1 K_2 K_3 MT(s) E(s) = \frac{6.757 \times 10^{13}}{s^4 + 23.65 s^3 + 537.3 s^2 + 2616 s + 4.354 \times 10^4} \left( \frac{mm}{m} \right)$$

The previous transfer function generates a deflection in millimeters. Therefore, converting the deflection to meters results in the following equation:

$$G(s) = \frac{48.7}{s^4 + 23.65 s^3 + 537.3 s^2 + 2616 s + 4.354 \times 10^4} \left( \frac{m}{Xmpss} \right)$$

---

**Note:** This transfer function does not include the K1 parameter

---

---

It is now possible to determine the system's state variable parameters from the overall transfer function. These are as follows:

$$A = \begin{bmatrix} -24 & -537 & -2616 & -43535 \\ 1 & 0 & 0 & 0 \\ 0 & 1 & 0 & 0 \\ 0 & 0 & 1 & 0 \end{bmatrix}, B = \begin{bmatrix} 1 \\ 0 \\ 0 \\ 0 \end{bmatrix}$$

$$C = [0 \ 0 \ 0 \ 6.7571 \times 10^{10}], D = [0]$$

The system does not have any transmission zeros and is therefore minimum phase. From the eigenvalues of the system and the pole-zero plot, we can also see that the plant transfer function  $G(s)$  is stable. Its eigenvalues are:

$$\lambda_G = \begin{bmatrix} -11.555 + 16.9700i \\ -11.555 - 16.9700i \\ -.2715 + 10.1594i \\ -.2715 - 10.1594i \end{bmatrix}$$

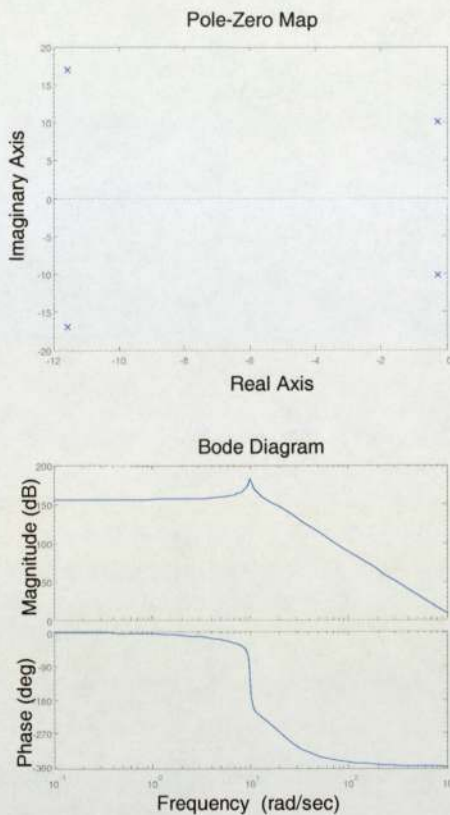


**Figure 3.18,** Pole-Zero and Bode plot of the Plant Transfer Function  $G(s)$

Both the controllability and observability matrices have a full rank of 4. This indicates the four linearly independent rows for the controllability matrix and four linearly independent columns for the observability matrix. This clearly demonstrates that the system is both controllable and observable and as mentioned previously, minimal.

For a system to be considered minimum phase, its dynamics must be globally stable. As this system is SISO, being minimum phase indicates that there exists a unique input that is capable of producing zero output. In addition, it indicates that the system has uniform relative degree. In this form, neither the numerator nor the denominator can be further differentiated, and the relative degree relates to the number of output differentiations required to produce the input [22].

---

### 3.6 Discussion

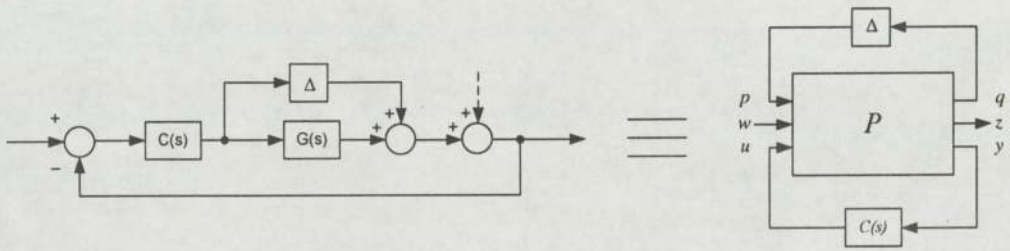
As mentioned previously, this system is for only one of the strain gauge sensors. In the future, all three strain gauge sensor readings could be combined to provide a multiple in and multiple output system (MIMO). The multiple inputs would be derived from the desired curvature. This would correlate to a desired deflection for each sensor point.

One of the concerns with this flexible system model is that the desired motor positions and deflections of the digit are discrete. The simulation sends out discrete serial pulses which are transformed to pulse widths, and in turn to a specific deflections of the beam. The operating range of the digit is between 0 and 30 deg, which corresponds to approximately fifteen discrete steps or 12.93 degrees of motor rotation. Clearly this is insufficient and will have to be altered for future configurations. Having rotation steps of this magnitude might cause the system to become unstable, when attempting to control its performance. The range of motor motion will need to be increased to produce smaller steps in the deflection. This could be accomplished by appropriate gearing or pulley system.

## 4 Controller Design

The following section outlines the procedure used in the development of the controller for the flexible cable actuated digit. The controller is designed in such a way that the overall system is robustly controlled using the sensory feedback voltages from the strain gauges. The control variable for the system is the serial motor command, while the output is the deflection of the beam.

Although many controller alternatives exist, the  $H_\infty$  controller has been chosen for this application. The reason for this choice is because of the  $H_\infty$  controller's disturbance rejection capabilities, and its ability to include a model for uncertainty in its design. The design relies on using a Linear Fractional Transformations (LFT) of the existing system, whereby a general nominal system  $P$  is derived, which characterizes this system.



Figure, Linear Fractional Transformation to a General Nominal System  $P$

Where

- $z$ : regulated or controlled variable
- $y$ : measurements
- $u$ : control input
- $w$ : sources of disturbance
- $q$ : uncertainty input
- $p$ : uncertainty output
- $\Delta$ : uncertainty model

---

The designed  $H_\infty$  controller has the robustness to control the overall system when subjected to disturbance over a range of frequencies.

---

**Note:** There are two types of uncertainty, additive and multiplicative. However, for the purpose of the design, only the additive uncertainty is examined.

---

---

## 4.1 $H_\infty$ Control Overview

The design of the  $H_\infty$  controller is completed in two stages:

- Robust Control or the  $H_\infty$  Synthesis
- Nominal Design or the Robustness Analysis

The first stage of the design, the  $H_\infty$  synthesis, relies on removing the uncertainty completely from the system ( $\Delta = 0$ ), and designing the controller based on Riccati solution to the equations. Essentially the objective is to design a controller whereby the ratio of energy output to input is minimized. In other words the criterion becomes:

$$\min_C \left\{ \max_{w \neq 0} \frac{\|\bar{z}\|_{L2}}{\|w\|_{L2}} \right\} = \min_C \|T_{zw}(P, C)\|_\infty \quad [23]$$

---

**Note:** The solution to these equations requires that the system transfer functions be represented in their state variable forms.

---

The second stage to the design includes the uncertainty in the system ( $\Delta \neq 0$ ), and determines the maximum allowable uncertainty that the new system with controller can accept before it becomes unstable. This suggests minimizing the maximum amplification gain between the uncertainty's input and output over all frequencies. The maximum gain must be below a certain value  $\gamma^{-1}$ , thereby creating the robust stability problem.

Therefore if a Linear Time Invariant (LTI)  $\Delta$  with  $\|\Delta\|_\infty$  exists, interconnected system  $T_{pq}(P, C)$  is stable if and only if:

$$\min \|T_{pq}(P, C)\|_\infty \leq \gamma^{-1}$$

---

This is called the Small Gain Theorem [23]. The maximum allowable uncertainty in the system before it becomes unstable is found by ensuring that it lies below the reciprocal of this value  $\gamma$ , and is formulated as such:

$$\|\Delta\|_{\infty} \leq \gamma$$

---

## 4.2 System Analysis

The plant model derived in **Section 3.5** was derived with the K1 parameter included to compensate for the conversion from tracking error (deflection) to the control signal (serial command). However, the controller is intended to do just this, therefore the K1 gain parameter has been removed from the plant model. The new plant model becomes:

$$G(s) = \frac{48.7}{s^4 + 23.65s^3 + 537.3s^2 + 2616s + 4.354 \times 10^4} \left( \frac{m}{Xmpss} \right)$$

This new open loop plant model is analyzed in this section. In addition, the closed loop system is constructed, and its stability observed. This closed loop transfer function includes the K1 gain however.

$$G_{cl}(s) = \frac{86.2}{s^4 + 23.65s^3 + 537.3s^2 + 2616s + 4.362 \times 10^4} \left( \frac{m}{m} \right)$$

The bode plots and root locus diagrams for both these models are shown in **Figures 4.1 to 4.4**.

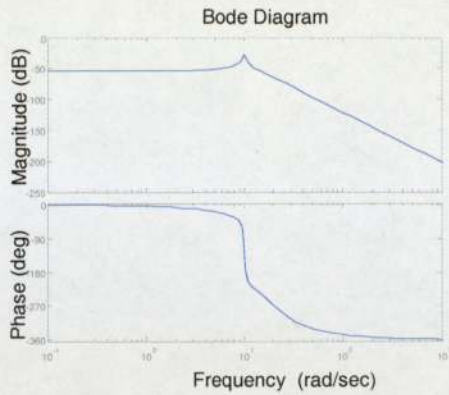


**Figure 4.1,** Bode Magnitude Plot of Closed Loop System without Controller

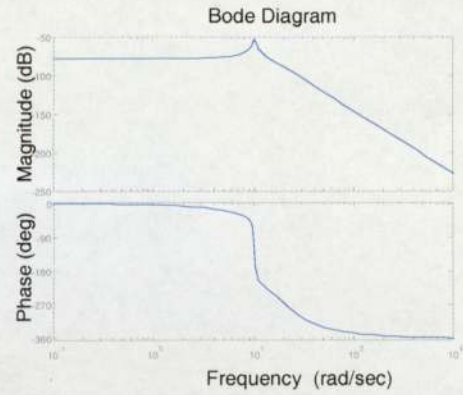


**Figure 4.2,** Bode Magnitude Plot of Plant Model

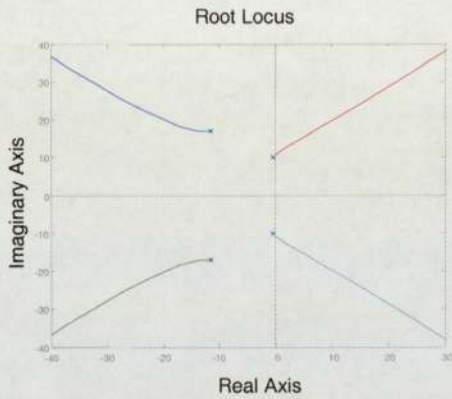


**Figure 4.3,** Root Locus Plot of Closed Loop System without Controller

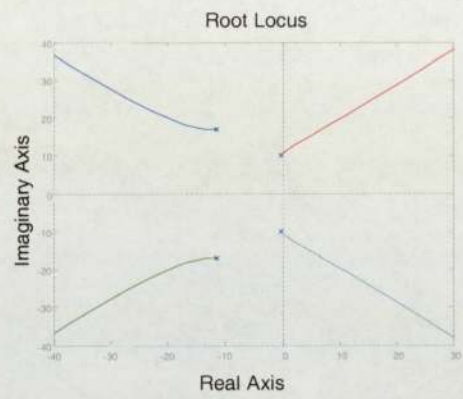


**Figure 4.4,** Root Locus Plot of Plant Model

The dominant poles of the open-loop transfer function indicate that the system gain cannot be increased much more before the system becomes unstable. These poles emerge from the effects of the flexible digit derived in **Section 3.1.2**. This proximity to instability of the system becomes just as apparent with the closed-loop transfer function. Once again, two of the system poles lie extremely close to the imaginary axis. Increasing the gain will most certainly create instability in the system.

---

**Note:** The poles of the closed loop system are almost exactly the same as the poles of the open loop system.

---

---

**Table 4.1, Poles of the Closed and Open Loop Systems**

<b>Closed-Loop Poles</b>	<b>Plant Poles</b>
-11.5587 +16.9695i	-11.5550 +16.9700i
-11.5587 -16.9695i	-11.5550 -16.9700i
-0.2678 +10.1644i	-0.2715 +10.1594i
-0.2678 -10.1644i	-0.2715 -10.1594i

Although the closed loop system with K1 gain parameter included would operate, it would not operate properly when subjected to disturbances over the desired frequencies. Therefore, a controller must be designed in such a way that it stabilizes the system poles. One such approach would be to include zeros into the system that cancel the effect of these poles, and new poles inserted that lie farther away from the imaginary axis.

---

### 4.3 Design of Controller (SISO)

When designing a robust controller, it is necessary to minimize the tracking error of the closed loop system over all frequencies of interest. One such approach is to minimize the maximum amplification gain between the disturbance (input) and the output, which in this case is the tracking error. Amplifying this signal in the frequencies of interest would satisfy this requirement. Most surgical tools are operated at frequencies below the 5 Hz or  $10\pi$  rad/s. Therefore using this value as the cutoff satisfies the requirements of this arrangement. A simple low pass filter is used to amplify the tracking error for these lower frequencies. The filter takes the following form as a transfer function:

$$F(s) = \frac{1}{s + 31.4159}$$

This transfer function is transformed into its state variable form as follows:

$$A = [-31.4159], B = [1]$$

$$C = [1], D = [0]$$

Where A, B, C, and D are the state variable coefficients derived from the state variable equations:

$$\dot{x} = Ax + Bu$$

$$y = Cx + Du$$

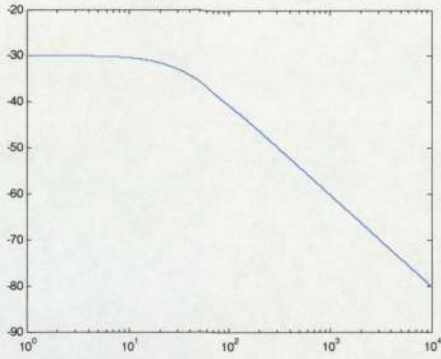


**Figure 4.5,** Singular Value Plot for  $F(s)$

The singular value plot in **Figure 4.5** demonstrates that most of the energy of this filter lies below the 31.4159 rad/s frequency. Its peak value for this filter is at -29.9474 dB.

$F(s)$  is absorbed into the nominal system  $P$ , and the objective becomes that of minimizing the maximum amplification gain with respect to the controller over all frequencies.

$$\min_C \|FT_{zw}(P, C)\|_{\infty}$$

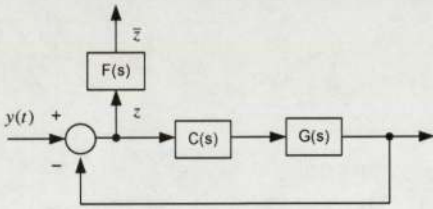


**Figure 4.6,** Block Diagram of System Including  $F(s)$

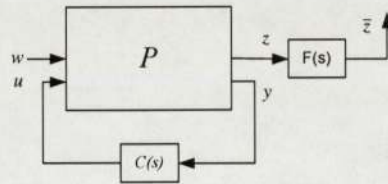


**Figure 4.7,** Nominal System  $P$ , Including  $F(s)$

#### 4.4 Nominal H-∞ Synthesis (Δ = 0)

The first part of the design of the controller is to assume that there is no uncertainty (Δ = 0) within the model. The controller is then designed by isolating it from the rest of the system (see **Figure 4.8**). Before proceeding, however, the closed loop system must be translated to a Linear Fraction Transformation (LFT). In other words the state space realization of the generalized nominal model P is determined in terms of the filter and plant's state space parameters. Therefore for a system excluding the uncertainty, the input vector is  $\begin{bmatrix} w \\ u \end{bmatrix}$ , while the output vector is  $\begin{bmatrix} \bar{z} \\ y \end{bmatrix}$ . The nominal system takes the following form:

$$P = \begin{cases} \begin{bmatrix} \dot{x} \\ \dot{x}_f \end{bmatrix} = \begin{bmatrix} A & 0 \\ -B_f C & A_f \end{bmatrix} \begin{bmatrix} x \\ x_f \end{bmatrix} + \begin{bmatrix} 0 & B \\ B_f & -B_f D \end{bmatrix} \begin{bmatrix} w \\ u \end{bmatrix} \\ \begin{bmatrix} \bar{z} \\ y \end{bmatrix} = \begin{bmatrix} -D_f C & C_f \\ -C & 0 \end{bmatrix} \begin{bmatrix} x \\ x_f \end{bmatrix} + \begin{bmatrix} D_f & -D_f D \\ I & -D \end{bmatrix} \begin{bmatrix} w \\ u \end{bmatrix} \end{cases}$$

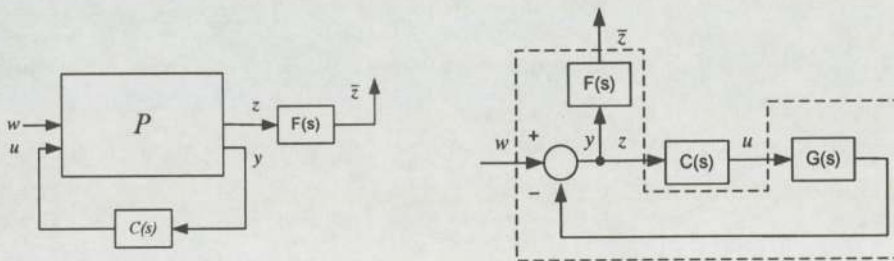


Figure 4.8, Block Diagram of Nominal System P

The optimal controller C(s) for this system with two inputs and two outputs, is designed using the Robust Control and LMI Toolbox within MATLAB. The “*hinfric*” command computes the best H<sub>∞</sub> performance and central controller. This controller is designed in such a way that it internally stabilizes the plant P(s) using a Riccati-based approach to solve the equations. The objective of the design is to minimize the maximum energy between regulated control variable (tracking error  $\bar{z}$ )

and the disturbances. In other words, the maximum gain of the transfer function between these two variables is minimized over all frequencies. As explained in **Section 4.1**, the objective is:

$$\min_C \left\{ \max_{w \neq 0} \frac{\|\bar{z}\|_{L2}}{\|w\|_{L2}} \right\} = \min_C \|T_{\bar{z}w}\|_{\infty}$$

The designed controller becomes:

$$K(s) = \frac{6.963 \times 10^7 s^4 + 1.649 \times 10^9 s^3 + 3.742 \times 10^{10} s^2 + 1.822 \times 10^{11} s + 3.032 \times 10^{12}}{s^5 + 215.7 s^4 + 2.261 \times 10^4 s^3 + 1.458 \times 10^6 s^2 + 5.921 \times 10^7 s + 9.43 \times 10^8}$$

$$\left( \frac{\text{SerialCommand}}{m} \right)$$

The poles and transmission zeros of this controller are listed in **Table 4.2** and its singular value and root locus plots in **Figures 4.9** to **4.11**.

*Table 4.2, Pole and Transmission Zeros for the Controller*

Poles of K(s) (x 10 <sup>4</sup> )	Zeros of K(s) (x 10 <sup>4</sup> )
-31.4159	-11.5550 + 16.9700i
-19.7364 + 65.3488i	-11.5550 - 16.9700i
-19.7364 - 65.3488i	-0.2715 + 10.1594i
-72.4288 + 34.5735i	-0.2715 - 10.1594i
-72.4288 - 34.5735i	

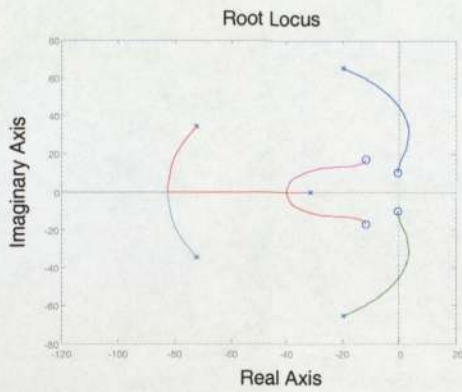


**Figure 4.9,** Root Locus Plot of the Controller

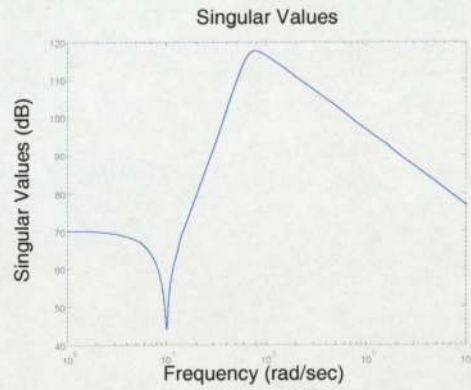


**Figure 4.10,** Singular Value Plot of the Controller

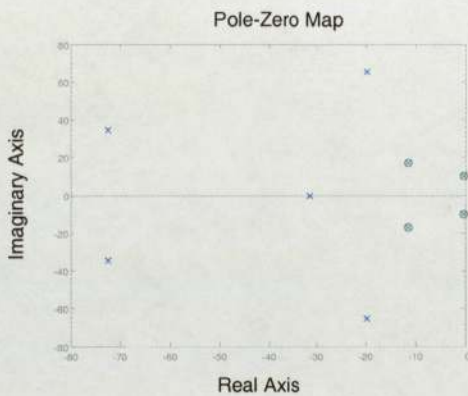


**Figure 4.11,** Exploded Pole-Zero Plots of the Plant and Controller

There will be a pole/zero cancellation as the dominant poles of the plant are the zeros of the controller. The new dominant poles of the system will become  $-19.74 + 65.35i$  and  $-19.74 - 65.35i$ . The controller is stable, as all its poles lie in the left hand plane of the pole-zero plots. In addition, all the transmission zeros of the controller lie in the left-hand plane, making the system minimal phase.

The LFT of the system with the desired deflection as the input, and the tracking error as the output, produces the  $T_{zw}$  transfer function. This system also excludes the uncertainty in the plant model. The input vector is  $[w]$ , while the output vector is  $[z]$ , and the  $T_{zw}$  nominal system therefore becomes:

$$T_{zw} = \left\{ \begin{array}{l} \begin{bmatrix} \dot{x} \\ \dot{x}_k \end{bmatrix} = \begin{bmatrix} A & BC_k \\ -B_k C & A_k \end{bmatrix} \begin{bmatrix} x \\ x_k \end{bmatrix} + \begin{bmatrix} 0 \\ B_k \end{bmatrix} [w] \\ [z] = [-C \quad 0] \begin{bmatrix} x \\ x_k \end{bmatrix} + [I][w] \end{array} \right\}$$

The maximum tracking error is defined as the maximum singular value over all frequencies ( $\|T_{zw}\|_{\infty}$ ). The singular values for  $T_{zw}$  are plotted in **Figure 4.12**. The maximum gain of the system is found to be 2.2645 dB, occurring at 51.769 rad/s.

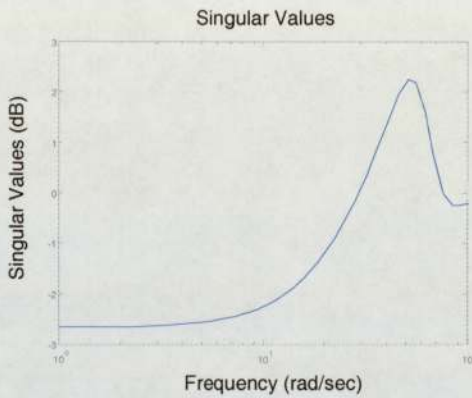


**Figure 4.12**, Singular Value Plot of  $T_{zw}$

Clearly from **Figure 4.12**, the tracking error is quite small at lower frequencies, and as expected, larger at higher frequencies. Most of the system's energy is in these higher frequencies, frequencies above 31.4159 rad/s.

Therefore as expected, the emphasis on the minimization on the tracking error for frequencies lower than 31.4159 rad/s has been achieved with the low pass filter.

---

## 4.5 Analysis of $T_{yw}$ and $T_{uw}$ transfer functions

The following section will examine the step responses of the closed loop transfer function,  $T_{yw}$ , and the control variable to input variable signal transfer function,  $T_{uw}$ .

The LFT form and state space representation for these two transfer functions is as follows:

$$T_{yw} = \left\{ \begin{array}{l} \begin{bmatrix} \dot{x} \\ \dot{x}_k \end{bmatrix} = \begin{bmatrix} A & BC_k \\ -B_k C & A_k \end{bmatrix} \begin{bmatrix} x \\ x_k \end{bmatrix} + \begin{bmatrix} 0 \\ B_k \end{bmatrix} [w] \\ [y_s] = [-C \quad 0] \begin{bmatrix} x \\ x_k \end{bmatrix} + [0][w] \end{array} \right\}$$

$$T_{uw} = \left\{ \begin{array}{l} \begin{bmatrix} \dot{x} \\ \dot{x}_k \end{bmatrix} = \begin{bmatrix} A & BC_k \\ -B_k C & A_k \end{bmatrix} \begin{bmatrix} x \\ x_k \end{bmatrix} + \begin{bmatrix} 0 \\ B_k \end{bmatrix} [w] \\ [z] = [0 \quad C_k] \begin{bmatrix} x \\ x_k \end{bmatrix} + [0][w] \end{array} \right\}$$

There exist two concerns with the step responses of these transfer functions. The first is with the signal taking too long to settle, and the second is with the level of the control signal. A large controlling signal could certainly saturate the actuator. The response for each system is shown in **Figures 4.13 to 4.16**. It is apparent that both step responses settle fairly quickly, however, the initial activation level of  $T_{uw}$  is well outside acceptable limits. This might not cause too much of a problem for this system as the actuator is controlled by a serial command from MATLAB. It is impossible for this variable to exceed the 0 and 254 boundaries. If the actuator was a position controlled DC motor, however, the initial values would most certainly saturate it.

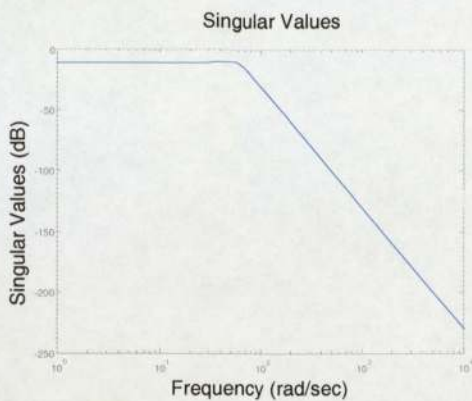


**Figure 4.13**, Singular Value Plot of  $T_{yw}$

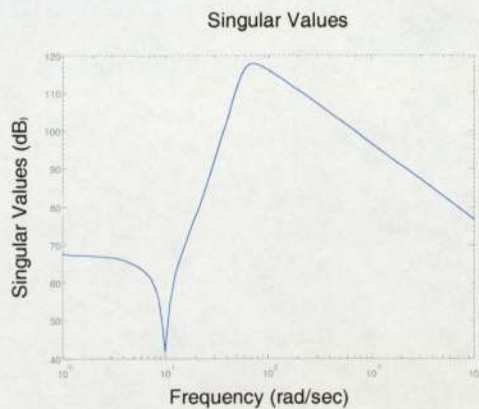


**Figure 4.14**, Singular Value Plot of  $T_{uw}$

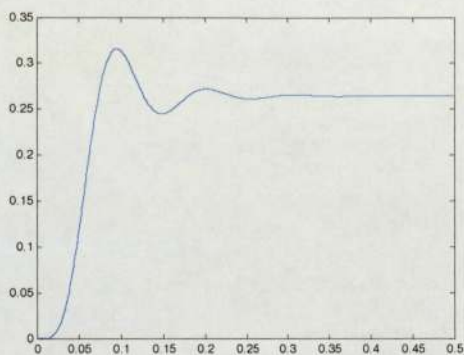


**Figure 4.15**, Step Response of Closed Loop System  $T_{yw}$

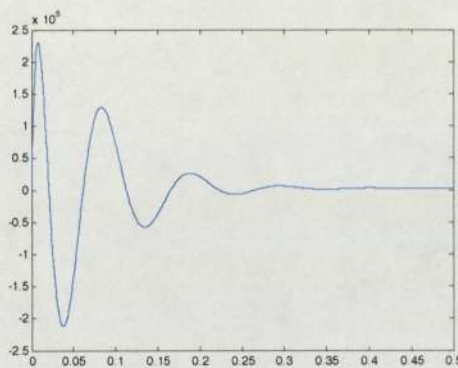


**Figure 4.16**, Step Response of Closed Loop System  $T_{uw}$

The settling times from both systems are less than 30 ms. This is just above the pulse 19 ms period of the servo-motors. The magnitude of the control variable from  $T_{uw}$ , however, is a definite concern. The actuation level of the signal reaches values of  $2 \times 10^5$ . This is even more apparent with the singular values plot, as the amplification gain at frequencies below the 5 Hz, is already above 60 dB. This would most certainly cause problems were it not for the serial command boundaries. However, even with these boundaries, at these levels, the system would not be controlled properly. Perhaps a new filter should be examined that will reduce these values. A variety of filters are examined in Section. However, for the purpose of explaining the  $H_\infty$  design, the 5 Hz filter will continue to be used.

## 4.6 Robustness Analysis ( $\Delta \neq 0$ )

The next stage of the  $H_\infty$  design is to determine the robustness of the controller and system. As explained in **Section 4.1**, this analysis now includes uncertainty in the system model ( $\Delta \neq 0$ ). It also requires determining the transfer function,  $T_{pq}$ , and ensuring system robustness even under the influence of model uncertainty. This is accomplished by determining the maximum uncertainty that the system can tolerate before becoming unstable. In order to do this, the closed loop system is first transformed as a LFT, and the state space realization of the generalized nominal model  $P$  is determined. The transfer function is derived in terms of the state space parameters for the controller and plant.

Additive uncertainty is assumed in the derivation. This means that for the system model excluding this uncertainty, the input vector is  $[p]$ , while the output vector is  $[q]$ . The nominal system therefore takes the form:

$$T_{pq} = \left\{ \begin{array}{l} \begin{bmatrix} \dot{x} \\ \dot{x}_k \end{bmatrix} = \begin{bmatrix} A & BC_k \\ -B_k C & A_k \end{bmatrix} \begin{bmatrix} x \\ x_k \end{bmatrix} + \begin{bmatrix} 0 \\ -B_k \end{bmatrix} [p] \\ [q] = \begin{bmatrix} 0 & C_k \end{bmatrix} \begin{bmatrix} x \\ x_k \end{bmatrix} + [0][p] \end{array} \right\}$$

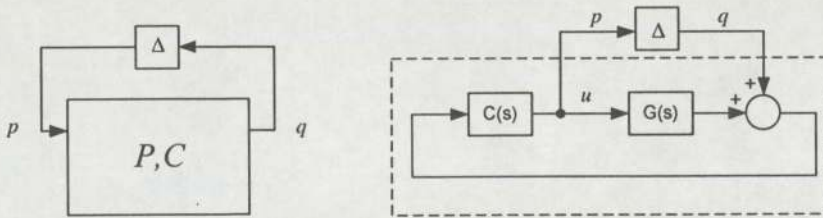
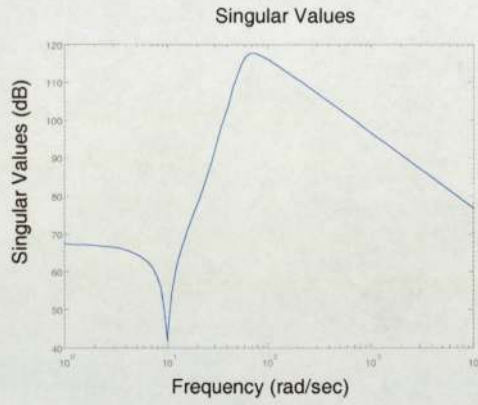


Figure 4.17, Block Diagram of Nominal System ( $P,C$ )

As explained previously,  $\|T_{pq}\|_\infty \leq \gamma^{-1}$  and  $\|\Delta\|_\infty \leq \gamma$ , where  $\|\Delta\|_\infty$  is the maximum additive uncertainty, and  $\gamma$  is an arbitrary number which should be less than 1.  $\gamma$  is

---

found by determining the maximum singular value for  $T_{pq}$  over all frequencies. From **Figure 4.18**, the maximum singular value is 117.8315 dB. Therefore the model's uncertainty must be lower than 0.0085 or 0.85 %, for the overall system to remain stable under all conditions. Clearly this is too small amount of model error. Other controllers should be examined that would allow for a high error tolerance.



**Figure 4.18**, Singular Value Plot for  $T_{pq}$

---

## 4.7 Alternative Filters Analysis

As demonstrated in **Section 4.5**, the step response and singular value plots for  $T_{uw}$  indicate that the motor will saturate. Therefore several other filters are examined in this section: a 0.5 Hz, a 39 Hz, and a 50 Hz lowpass filters.

The same procedures used for the controller design of the 5Hz filter have been replicated for these, and the step response plots for  $T_{uw}$  are shown in **Figures 4.19** to **4.22**.

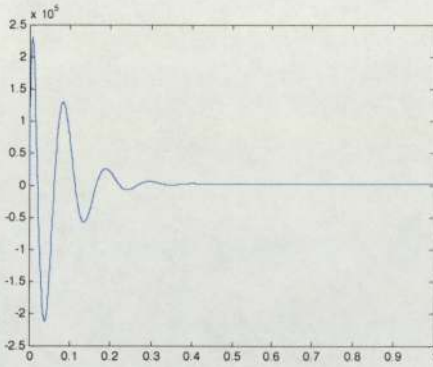


*Figure 4.19,  $T_{uw}$  plot for 5Hz (0.85% error tolerance)*

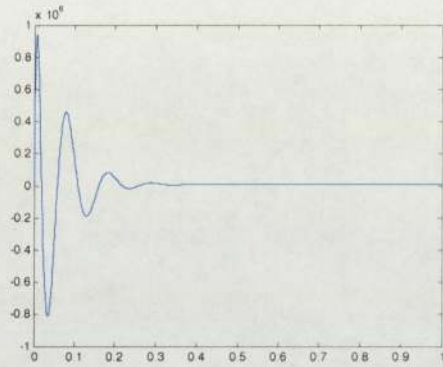


*Figure 4.20,  $T_{uw}$  plot for 0.50 Hz(0.78% error tolerance)*

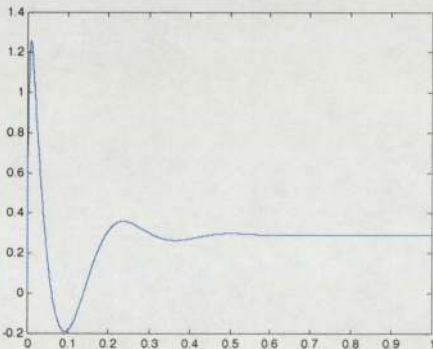


*Figure 4.21,  $T_{uw}$  plot for 39 Hz (22.48% error tolerance)*

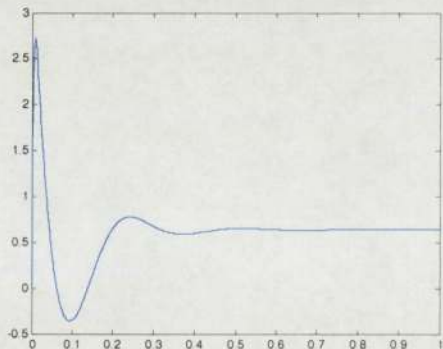


*Figure 4.22,  $T_{uw}$  plot for 50 Hz (2.6% error tolerance)*

---

From the step response plots, we immediately notice the 0.5 Hz bandpass filter is ineffective for two reasons. Firstly because its cutoff frequency lies well below the desired operating frequency of 5 Hz, and secondly because the control signal is amplified in excess of  $0.9 \times 10^6$ . The step response plots for the 39 Hz and 50 Hz filters are far more desirable as the control signal is well within desirable limits. The only setback of using these filters is that the system's response is a slightly slower. This is hardly noticeable however, and is considered well within acceptable limits.

The results for the maximum acceptable uncertainty, that the system can handle, however is highest for the 39 Hz filtered system. It allows for a 22.48% error before the system becomes unstable. The new transfer function for the controller becomes:

$$K(s) = \frac{416.5s^4 + 9852s^3 + 2.238 \times 10^5 s^2 + 1.09 \times 10^6 s + 1.813 \times 10^7}{s^5 + 298s^4 + 1.463 \times 10^4 s^3 + 4.347 \times 10^5 s^2 + 7.223 \times 10^6 s + 6.277 \times 10^7}$$
$$\left( \frac{\text{SerialCommand}}{m} \right)$$

The poles and transmission zeros of this controller are listed in **Table 4.3** and its singular value and root locus plots are shown in **Figures 4.23** and **4.24**.

**Table 4.3, Controller Poles and Transmission Zeros**

Poles of $K(s)$ ( $\times 10^2$ )	Zeros of $K(s)$ ( $\times 10^4$ )
-2.4504	-11.5550 + 16.9700i
-0.0914 + 0.2256i	-11.5550 - 16.9700i
-0.0914 - 0.2256i	-0.2715 + 10.1594i
-0.1732 + 0.1150i	-0.2715 - 10.1594i
-0.1732 - 0.1150i	

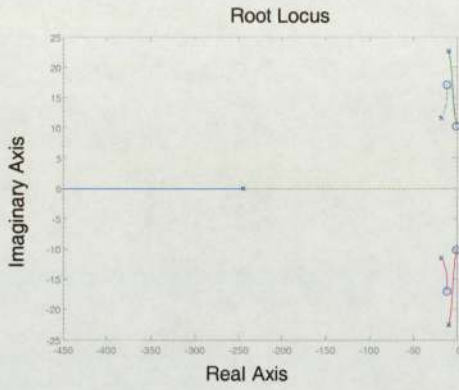


**Figure 4.23, Root Locus Plot of the Controller**

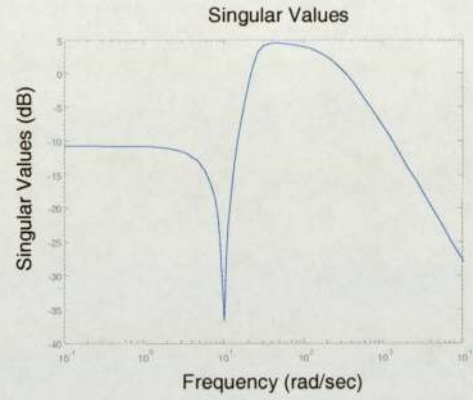


**Figure 4.24, Singular Value Plot of the Controller**

---

## 4.8 Discussion

The  $H_{\infty}$  controller has been designed by solving the Riccati equations of the LFT for which maximum tracking error of the system has been minimized for frequencies below the 5 Hz requirement.

An uncertainty analysis was also completed, demonstrating the amount of uncertainty the plant model can accept before the overall system becomes unstable. Invariably there will be errors within the model, however, as shown, the designed controller can accept up to 22.5% error before the overall system becomes stable. Therefore this controller is acceptable in controlling the overall system robustly over a variety of frequencies.

---

## Chapter 5

### 5 Digital Controller Design

During a design or during normal operation of a system, it is often necessary to change certain parameters of a controller. This derives from the fact that after it has been designed and implemented in a system, the system might change with time. These changes might be due to deterioration of parts or to different operating environments. Therefore if a controller was designed and manufactured using electronic circuitry, we would have to alter its circuit every time to compensate for these changes. However, with the advancements in computers and data acquisition cards (DACs), it is possible to implement the controllers in discrete time using computer programs. The continuous signals from the external circuitry are discretized into digital signals and processed through the digital controller. As long as the sampling rate of the DACs is sufficiently small, and the clock speed of the computer implementing the controlling program fast enough, virtually the same results as with a continuous controller can be achieved. The advantage being that the parameters of the system can be altered very easily.

The following section outlines the procedure used in the digitization of the continuous controller from **Section 4.7**. The flexible digit system requires digitization of its controller, as it is integrated within MATLAB, and controls the actuator through serial communication to the MILINST servo-driver board. **Figure 5.1** demonstrates the block diagram layout of the overall system with digital controller.

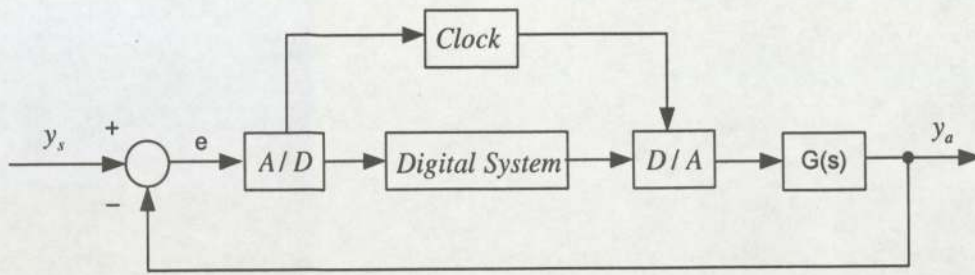


*Figure 5.1, Block Diagram Representation of the Overall System*

The following steps are completed by the MATLAB program before finally sending the control variable to the actuator:

- Data acquisition of the strain gauge voltages
- Perform the required control algorithms
- Output the controlled serial pulse to the MILINST servo-driver board.

---

## 5.1 Digital Controller Design

This section concentrates on converting the transfer function of the controller to digital space first using the trapezoidal approximation and then next implementing it directly using state space equations.

### 5.1.1 Trapezoidal method

The trapezoidal method relies on approximating the integration by a trapezoid as shown in **Figure 5.2**. The derivation for variable “s” is then substituted directly into the continuous transfer function of the controller.

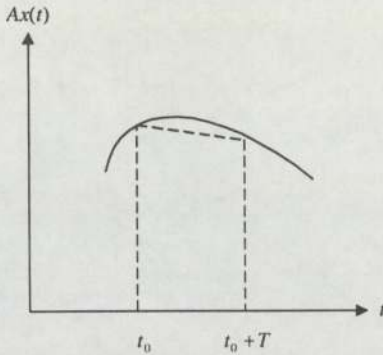


Figure 5.2, Trapezoidal Approximation of Digital Controller

$$x(t_0 + T) - x(t_0) \approx A \frac{x(t_0 + T) + x(t_0)}{2} T$$

With  $e(t) = 0$ , results in  $sX(s) = AX(s)$

Which gives

$$(E 5.1) \quad s = \frac{2}{T} \frac{z-1}{z+1} \quad [24]$$

Recall that the Laplace transform of the controller for the 39 Hz filter is:

$$K(s) = \frac{416.5s^4 + 9852s^3 + 2.238 \times 10^5 s^2 + 1.09 \times 10^6 s + 1.813 \times 10^7}{s^5 + 298s^4 + 1.463 \times 10^4 s^3 + 4.347 \times 10^5 s^2 + 7.223 \times 10^6 s + 6.277 \times 10^7}$$

The discretization procedure requires substituting (E 5.1) into this transfer function. This new equation will now be in terms of the sampling time,  $T$ , and the new discrete variable  $z$ . The trapezoidal approach works best for lower degree systems. However because this system is of degree 5, the substitution becomes quite tedious. The digitization of an arbitrary controller of degree 1 has been carried out in **Appendix E** to demonstrate the procedure. This same procedure could be carried out for the controller designed in **Section 4.7**. However, this would require upon implementation to MATLAB, the values for the error and control variables taken at five time steps prior to the present. This is not only difficult to implement, but produces erroneous results for these first few time steps as well.

The characteristics of the digital controller can also be altered by choosing different sampling times. Good practice recommends having a sampling frequency ( $1/T$ ) of about 10 times the bandwidth frequency (in Hz) of the closed loop transfer function [24]. In our case the band width (-3dB) occurs at around 24.3 rad/s or 38.67 Hz. In other words the sampling period should be less than 0.0259 sec.

**Figure 5.3** demonstrates the effect of sampling time on the closed loop system performance.

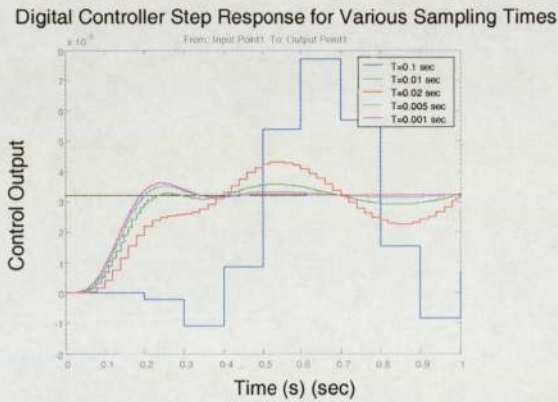


**Figure 5.3,** Step Response of Closed Loop System with Digital Controller

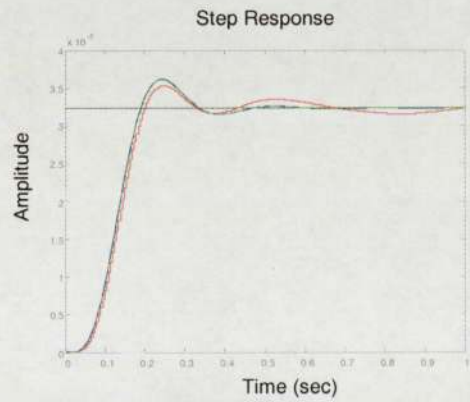


**Figure 5.4,** Step Response Comparison of Closed Loop System Comparison

Decreasing the sampling time, achieves a system response close to the continuous model. This is to be expected, as if we wanted to achieve the desired response, we

---

would have to decrease the sampling time to 0 seconds. We also notice that as we increase the sampling time, we get increasingly oscillatory responses, with higher settling times and larger percentage overshoot. Comparing the 1 ms sampling time digital model with the continuous model (see **Figure 5.4**), we notice that they are almost identical. Sampling times above the 5 ms value do not characterize the system appropriately however.

### 5.1.2 State Space Method

The second method of digital controller implementation uses the continuous state variable equations as a basis. There is, however, no way that a digital computer can compute the infinite number of points. The state equations can therefore be discretized in the following manner.

$$\begin{aligned}\dot{x} &= Ax + Bu \\ y &= Cx + Du\end{aligned}$$

By definition:

$$\dot{x}(t_0) \cong \lim_{\alpha \rightarrow 0} \frac{x(t_0 + \alpha) - x(t_0)}{\alpha}$$

This leads to:

$$x(t_0 + \alpha) - x(t_0) = [Ax(t_0) + Bu(t_0)]\alpha$$

or

$$x(t_0 + \alpha) = (I + \alpha A)x(t_0) + \alpha Bu(t_0)$$

where  $\alpha$  is the integration step size.

Tailoring this equation for a program results in the following [24]:

$$x((k+1)\alpha) = (I + \alpha A)x(k\alpha) + \alpha Bu(k\alpha)$$

where  $k$  is the total number of steps in the time range.

This equation is called the Euler Forward Algorithm, and although it's the simplest, it is the least accurate method of computing the response. The step size can be made very small, however, this would constitute many computations. An ideal sampling interval  $\alpha$  is computed by using a step input to the equation with arbitrary step size. The procedure is repeated for step size of  $\alpha/2$  and the results compared with the previous. If the error is large then the procedure is repeated again. A final step size is achieved once the error between  $\alpha$ 's is within acceptable limits. Figure demonstrates the step response of the digital controller for various time steps. As all time steps chosen produce almost the exact same results, the time step of 5 ms should be chosen for the digital system. Note however that a system with a step time above 10 ms results in a very instable system (see **Figure 5.6**).

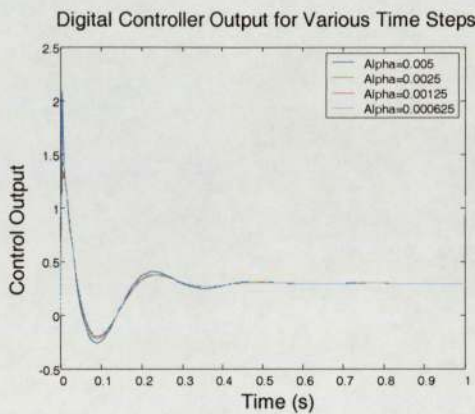


**Figure 5.5,** Step Response of Digital Controller (0.6 ms – 5 ms Sampling Times)

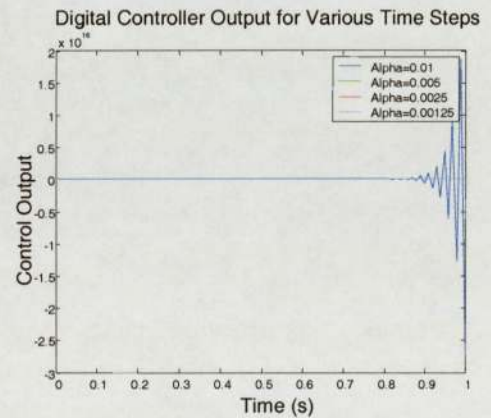


**Figure 5.6,** Step Response of Digital Controller (1 ms – 10 ms Sampling Times)

---

## 5.2 Implementation of the Digital Controller

The digital controller has been integrated into the overall system using the state space method. Although the data acquisition rate of the card is sufficient and the processing time for the controller with respect to the serial output control is negligible, the time to process the serial command to the MILINST servo driver board is too large. This inevitably slows the whole process down. The processing time should be no more than 1 ms, which would allow for the proper sampling rate and conversion to a pulse width modulation. However, as the sampling rate is increased, the signal becomes increasingly unstable and requires more time to settle.

The serial commands are sent to the MILINST board at a frequency of 20 ms. This becomes the limiter on the system. Although the data acquisition card's sampling rates are lower than this value, the controlling process can never be under the 20 ms restriction. **Figure 5.7** demonstrates that a sampling rate of 20 ms produces very erroneous and unstable results. There exists an enormous error between the continuous and discrete models.

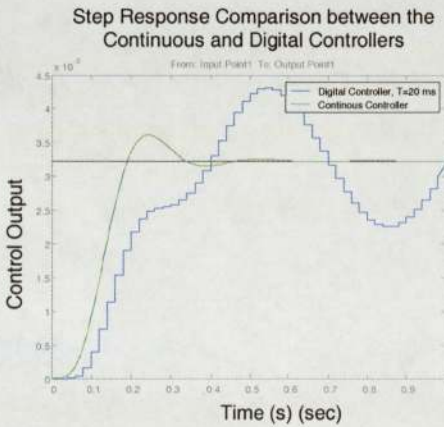


*Figure 5.7, Step Response Comparison*

Ideally the pulse width modulation signal should be outputted directly from MATLAB. However, because of Windows latencies, it is impossible to ensure a

---

stable pulse using this method either. Achieving real time results with sampling times of this magnitude is virtually impossible for a system operating within the MATLAB and Windows environments. One such feasible solution would be to control the system outside of the Windows environment. Another would be to use a motor that does not require pulse width as form of control.

---

### **5.3 Discussion**

It has been found that the digital controller cannot be properly integrated into the flexible digit system. The inherent sampling time constraints cause the system become highly unstable. These constraints come from the serial communication between the MATLAB program and the MILINST servo driver board. Future designs should incorporate either the pulse width directly as output from the controller, control of the servo outside of the windows environment, or use a DC motor with position control.

---

## Chapter 6

### 6 Tactile Sensing of the Non-Actuated Digit

The following Chapter describes the method of using sensors positioned along the steerable, cable-activated system as tactile sensing points. The system attempts to mimic a three section endoscope actuated with a cable to produce bending in a single axis.

However, for the purpose of deriving information from the sensing points, the actuation was disabled. The information from these sensors can be used to determine the shape, the position and magnitude of a load applied to the endoscope. This would be extremely useful for relaying information back to the surgeon as to what might be occurring within the body during operations. There are several methods of predicting these characteristics on systems such as this. One such method, and the one used for in this study, is the use of a neural network.

Strain gauges are certainly capable of satisfying the sensory needs and have been used on this system for the deflection measurements of the flexible digit. Their measurements are very susceptible to variations within similar measurements, but their sensitivity is improved by connecting the gauges in a  $\frac{1}{2}$  bridge configuration. Recall from **Section 2.3.1** that the relation between the measured voltage and the elongation of the gauge is:

$$\frac{V_m}{V_s} = \frac{GF}{4} \times 2\epsilon$$

Fibre-Bragg sensors have also proven themselves as been satisfactory for this type of arrangement and are demonstrated in [25]. These sensors clearly offer many benefits over their strain gauge counterparts. Their benefits present themselves in terms of their cost, size, multiplexing ability, electrical immunity, long term stability, and fatigue durability.

---

## 6.1 Creating the Neural Network

Neural networks allow us to replicate to a certain degree animal systems. Touch for instance is the combination of many sensors within the human body that relays information back to the brain as to the location, and force applied. Individuals will develop a specific sense of touch that will be optimized for the job they have. And each individual will be different from the next. Neural networks work in a similar fashion, where weights and biases are combined and optimized to fit a specific application. Just like humans, the network needs to be trained for these applications, and retrained should the system change. One of the benefits of the neural networks is that they allow us to explore independent functions within a system or a combination of systems, and optimize them to work as a single unit.

The following section will outline the steps taken to create the neural network that predicts the position of a palpation or obstruction along the endoscope using three sensing points. The network will be created using the NETLAB, a MATLAB second party software. The experimental data was collected from three separate tests, combined, normalized and run through an optimization program to determine the optimum number of hidden neurons. In addition the number of iterations necessary to converge to a solution within acceptable limits was established.

---

## 6.2 Neural Networks

The neural network designed in this section uses the NETLAB software toolbox [26]. This toolbox has been written for MATLAB and can be modified within the same to assist with the design. There exist various types of neural networks, however, a single layer feed-forward neural network is chosen for the flexible digit application. This technique uses linear regression to produce a generalized model. The model consists of a linear combination of input variables, with weights and biases comprising the parameters of the model that have been passed through an activation function. The type of activation function used depends on the modeled data and the desired result.

The four standard steps in the design of a neural network are shown in **Figure 6.1**.

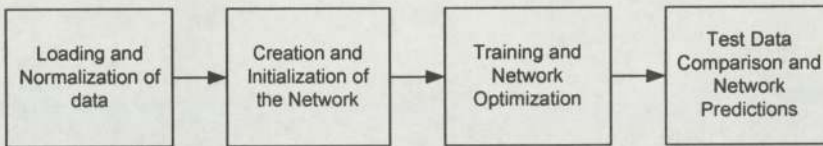


*Figure 6.1, Standard steps for implementing a neural network*

Effectively the information that could be extracted from the three sensors are:

1. Load Position
2. Load Magnitude
3. Load Contact

Although for this report, only the position of the load is examined.

### 6.2.1 Neural Network Strategies

There are three strategies that can be employed when predicting the output of a neural network: a combined neural network strategy (**Figure 6.2**), a parallel neural network strategy (**Figure 6.3**) and a cascaded neural network strategy (**Figure 6.4**).

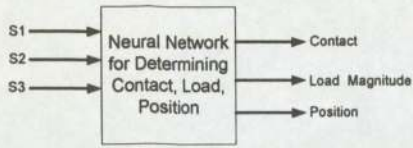


**Figure 6.2,** A Combined Neural Network to predict three output parameters

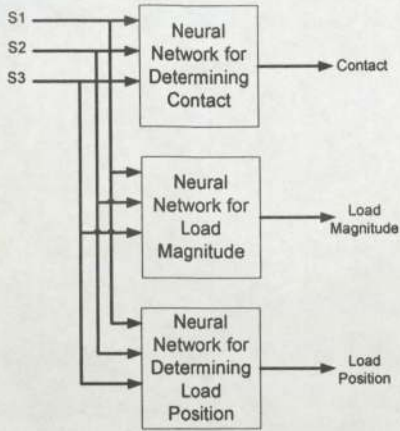


**Figure 6.3,** A Parallel Neural Network (three nets to predict three output parameters)

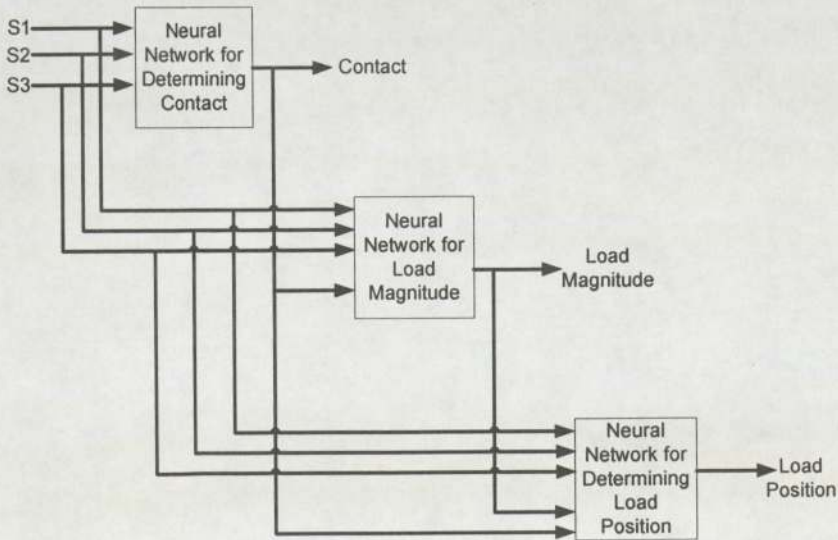


**Figure 6.4,** Cascaded Neural Network (three nets to predict three output parameters)

---

As shown in **Figure 6.4**, cascaded neural networks rely on the output of the previous network. Consequently an unsatisfactory previous network will further compound the errors within the existing network, resulting in even greater error in the overall network's prediction. Therefore, for the purpose of this Thesis, we are only considering the parallel Neural Network with load position prediction.

---

### 6.3 The Activation Function

Activation functions for the hidden units are required in order to introduce nonlinearity into the network. Without nonlinearity, the network would be no more powerful from the hidden units than just plain input and output system; a linear function of linear functions is again a linear function. It is the nonlinearity that makes multilayer networks so powerful. Almost any nonlinear function can be used as an activation function. The exception, however, are polynomials.

The activation function in the neuron is usually chosen to resemble a smooth step function. Essentially for back-propagation learning, it is desirable to have the activation function as differentiable and bounded. The most common choices are the Gaussian functions, and sigmoidal functions, such as logistic, hyperbolic tangent (see **Figure 6.5**).

These functions specify the output unit of the neural network. Choices in NETLAB for a single layer feed-forward neural network include *linear*, *logistic* and *softmax*. The linear regression ensures that the output will be in continuous numerical form. This means the output will be predicted up to a certain amount of measurable resolution. The hyperbolic tangent activation function was chosen for this application as it produces negative and positive values. Consequently it yields faster training than a function that only produces positive values, such as the logistic functions. It can achieve this because of better numerical conditioning.

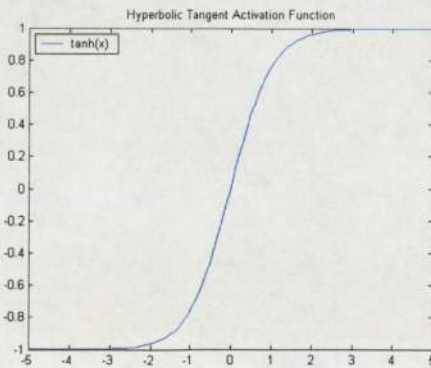


**Figure 6.5**, Hyperbolic Tangent Activation Function

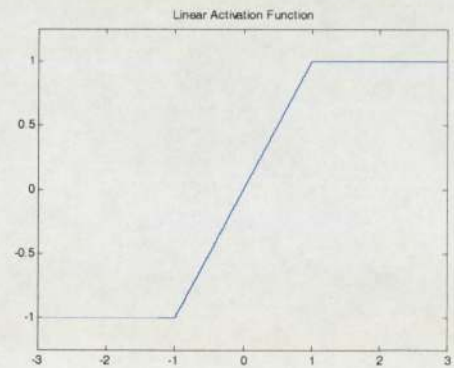


**Figure 6.6**, Linear Saturated Activation Function

---

## 6.4 Experimental Explanation

For a neural network to be able to predict the outputs based on the predetermined inputs, it is necessary to acquire a decent amount of data. Therefore three different weights were hung along the flexible digit at sixteen different positions. And, at each position and weight, the procedure was completed twenty-five times. This produced 1275 data points for training, validation, and testing of the neural network.

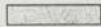
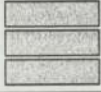
The sensor data was collected from six  $120\ \Omega$  strain gauges ( $GF \approx 0.8$ ) positioned along the flexible digit as shown in **Figure 1.1**. The strain gauges were combined into three pairs connected in half bridge configurations, and produced resistance changes as the flexible digit was deflected. The leads of the strain gauges were then connected to a Fylde FE-366-TA amplifier with an internal low-pass filter set to a cut-off frequency of 470 Hz. The amplifier converted the resistance change to a useful voltage reading. The three voltage readings were then read into MATLAB through the PCI-DAS1602/16 data acquisition card.

---

## 6.5 Load Positions and Weights

As explained previously, three different loads were positioned along the length of the flexible digit. These point loads were categorized as 7.5g, 12.5 g, and 25 g weights. Each weight was positioned along the digit in sixteen different positions as show in **Figure 6.8**. Position 1 is considered to be at the tip of the flexible digit. Each of the positions, with the exception of position 16, are 1 cm apart from one another.

The loads are categorized as in **Figure 6.7**. The first set of test data relied on taking three plastic weights, each weighing 2.5 g and positioning them at the sixteen positions. The second and third data sets replaced the plastic weights with lead weights, each weighing 12.5g, and once again positioned along the flexible digit at the sixteen positions. The sensor outputs were measured for all loaded positions and weights twenty-five times to ensure repeatability results. In addition, a no load condition was measured at the start of every test. This would assist in the determination of the load/no load and load magnitude prediction networks.

		
Single Load (Lead) Load 1 (12.5 g)	Double Load (Lead) Load 2 (25 g)	Triple Load (Plastic) Load 3 (7.5 g)

*Figure 6.7, Load Configurations*

*Table 6.1, Position and Load Combinations*

Position of load from the tip of the flexible digit	Load Type
0	Load 0 (No Load)
1 (0 cm)	Load 1, Load 2 & Load 3
2 (1 cm)	Load 1, Load 2 & Load 3
3 (2 cm)	Load 1, Load 2 & Load 3
4 (3 cm)	Load 1, Load 2 & Load 3
5 (4 cm)	Load 1, Load 2 & Load 3
6 (5 cm)	Load 1, Load 2 & Load 3
7 (6 cm)	Load 1, Load 2 & Load 3
8 (7 cm)	Load 1, Load 2 & Load 3
9 (8 cm)	Load 1, Load 2 & Load 3
10 (9 cm)	Load 1, Load 2 & Load 3
11 (10 cm)	Load 1, Load 2 & Load 3
12 (11 cm)	Load 1, Load 2 & Load 3
13 (12 cm)	Load 1, Load 2 & Load 3
14 (13 cm)	Load 1, Load 2 & Load 3
15 (14 cm)	Load 1, Load 2 & Load 3
16 (24 cm)	Load 1, Load 2 & Load 3

**Note:** The distance is measured from tip of flexible digit

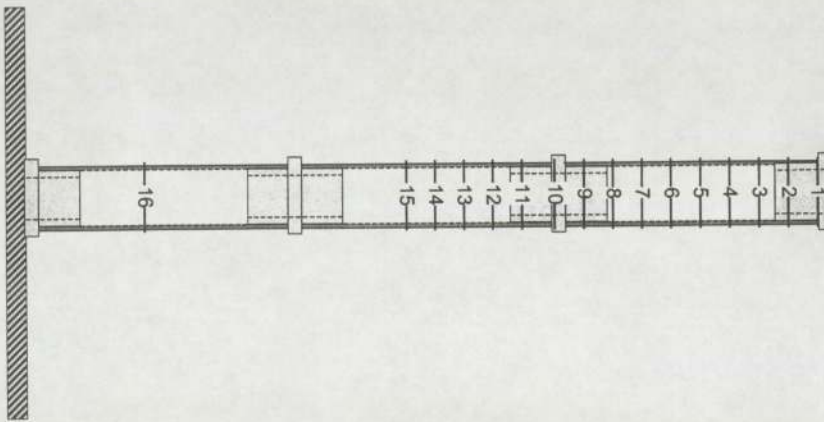


*Figure 6.8, Load positions along the flexible digit*

---

## 6.6 Data Normalization

In order to eliminate the chance of network training getting stuck on a local optimum, it is essential that the data be normalized. The normalization of the data ensures that all the network weights are closest to their optimum values. If this process is not completed, and not all the inputs are set as equally important, then the network weights won't have similar values. This process also ensures that the data can be initialized randomly.

The first step to normalizing the data is to set up it in the appropriate format. This requires randomizing the data, and then separating it into training data components ( $\frac{1}{2}$  of the data), validation data components ( $\frac{1}{3}$  of the data), and test data components (the remaining  $\frac{1}{6}$  of the data). We normalize the data by calculating the mean and the variance of the training data. The data from all sets are then normalized with respect to the mean and variance found from the training data set. The rescaled variables are found as such:

$$(E\ 6.1) \quad \tilde{x}_i = \frac{x_i - \bar{x}_i}{\sigma_i}, \quad [26]$$

where

$\bar{x}_i$ , is the mean of the training data,

$\sigma_i^2$ , is the variance of the training data

Figure 13 shows the data from the three strain gauge sensors for all three weights in its non-normalized form. We can see that the data demonstrates a linear pattern for specific weights as they are moved along the digit. Therefore we expect the neural network to act as a linear system with training. **Figure 6.10** demonstrates the normalization and randomization of the data for the same sets.

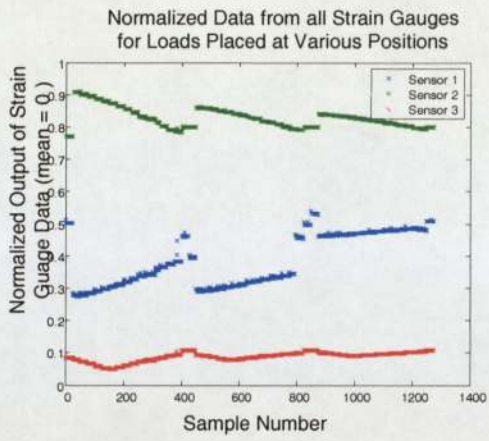


**Figure 6.9,** Non-Normalized data for all the strain gauges, loads, and load position

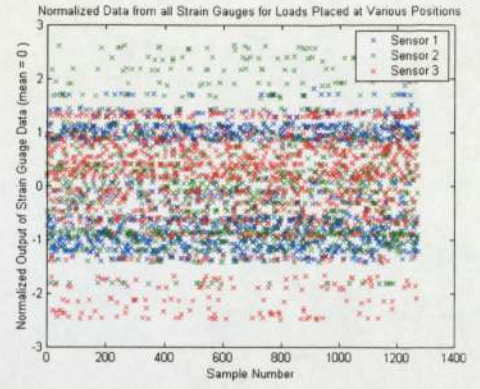


**Figure 6.10,** Normalized data for all the strain gauges, loads and load position

---

## 6.7 Data Optimization

The optimization process is completed after normalization of the data. This process optimizes the neural network using the training data and determines the optimum weights and number of hidden nodes that reduce the error between the actual data and the predicted. The procedure used for this optimization is called early stopping. It ensures that the network isn't over-trained by choosing too many or too few epochs (1 epoch is 50 iterations).

In order to do this, we must first determine the number of inputs and outputs to the system. In our case, the inputs are the strain gauge sensor data, and the output as the position along the beam at which the weight was applied to the flexible digit.

The next step is to determine the range of hidden nodes that we wish the network to determine for us. The training error is plotted on the same graph as the validation error for each of these number of hidden node configurations. A local minimum is achieved for the validation error as it clearly converges to a minimal error. The point at which the validation error and the training error are minimums, is the point at which the number of epochs or iterations are optimal. In effect, this ensures that we do not choose too many iterations for convergence. By doing so reduces computational time, as well as ensures that we do not over-train the network. **Figure 6.11** demonstrates the effects of under training and overtraining the network with respect to the validation error.

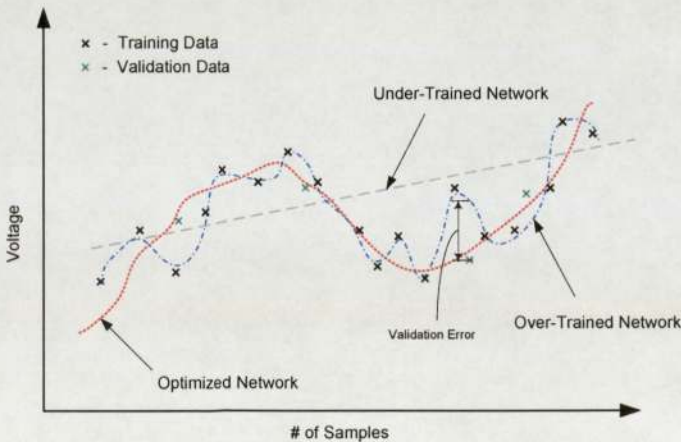


*Figure 6.11, Examples of Trained Networks*

---

## 6.8 Training the Neural Network

The training input feeds into the neural network and from the optimization program, creates weights and biases based on the data. The training output is already predetermined and is the target for the network. The program initializes the weights and biases based on the targeted data. These weights multiplied by the sensor inputs, produce an output. Based on the magnitude difference of the mean squared error between from the target value and the calculated, the program calculates new weights and biases, and then reruns the neural network with the sensor data again until this error has been minimized sufficiently. The method by which the program completes this is called the gradient of steepest descent.

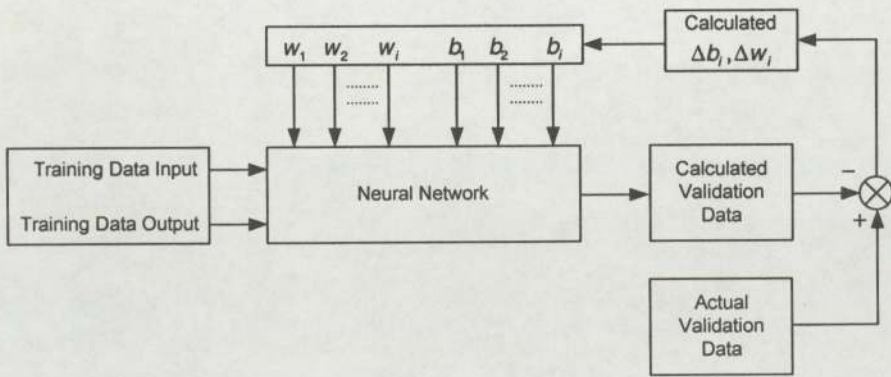


*Figure 6.12, Neural Network Back Propagation Training Scheme*

The network is then optimized even further by considering the validation data. The validation input data is fed into the previously calculated network, using the same weights and biases, and compared against the validation output data. The difference between the calculated validation output and the experimental validation output is the validation error. As expected, in non-linear networks, this data should reach a local minimum and then diverge, as the data is being over-trained or over-fitted. This is essentially because the more you train the data, the more the network will try to fit the curve, increasing the error between some points. The point at which the validation error reaches a minimum is the point at which the training should be stopped to minimize any noise from the data. This is called the early stopping point.

In the case of linear networks however, there are cases where there is no local minimum. This indicates that the input data is stable and extremely close to the training data. Essentially the error is minimized. We would expect our system to follow this trend as the data appears to be linear as discussed in **Section 6.6**.

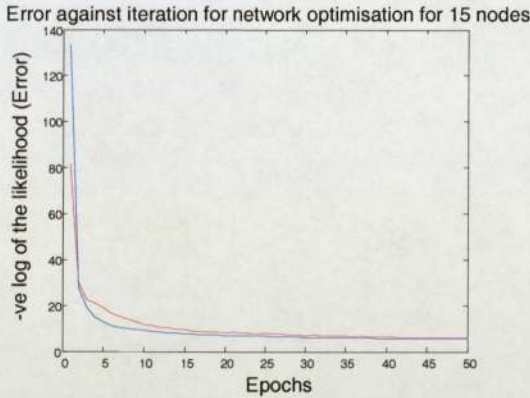


**Figure 6.13**, Error against iterations for 15 nodes, 50 epochs

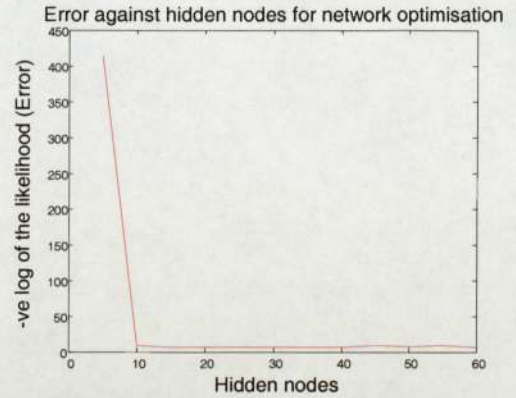


**Figure 6.14**, Error for 5 to 60 hidden nodes

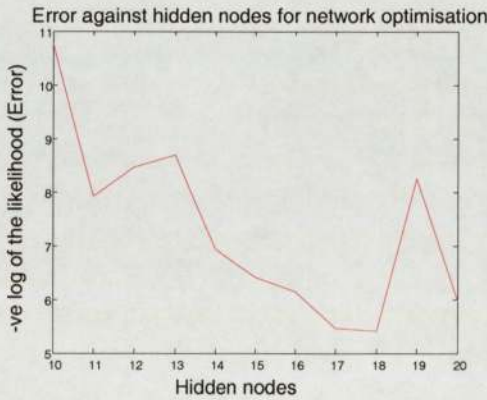


**Figure 6.15**, Error for 10-20 hidden nodes

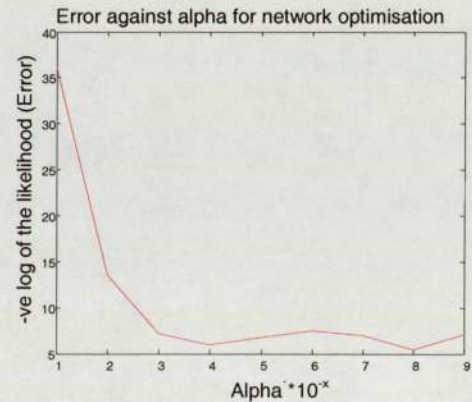


**Figure 6.16**, Error for Learning Gradient between  $10^1$ - $10^9$

We can see from **Figure 6.14** that the optimum number of hidden nodes following the optimization procedure has been determined as being from 10-60. As the error seems to be reasonably the same, we should choose the lowest number of hidden nodes to save time on the computational side of the network. Therefore, we have chosen the number of hidden nodes between 10 and 20 nodes. The optimization procedure was

---

completed once more for this 10-20 nodes configuration, this time in 1 node increments (see **Figure 6.15**). The results show that the lowest error occurs with 18 nodes.

The next step was to vary the power of the learning gradient, which had been set by default to  $10^{-7}$ . The learning gradient was then varied from  $10^{-1}$  to  $10^{-9}$  while keeping the hidden nodes constant at 18. The optimum learning gradient is found to be  $10^{-8}$  (see **Figure 6.16**). This information can be used now for the testing of the neural network.

It should be noted that the calculated optimum number of hidden nodes is only for the current system with three sensors. This would likely change for a system with fewer or more sensors.

---

## 6.9 Testing of the Optimized Network

Once the neural network has been optimized for certain weights and biases, it is now possible to validate its efficiency using the test data. The number of hidden nodes determined by the optimization procedure, as well as the test input data, is fed into the testing program at this stage. The resulting prediction of the output is then compared against the experimental test output data. The two data sets were plotted against each other as shown in **Figure 6.17**. The red points are the actual test points, whereas the blue are the predicted data from the neural network. Clearly this is quite confusing, as it is hard to distinguish between points. Therefore a plot demonstrating the percentage error between the two data sets at every point was generated (see **Figure 6.18**). The percentage error between the actual and the predicted generally lies under 10%, with the exception of a few, thus indicating decent matching of the two data sets.

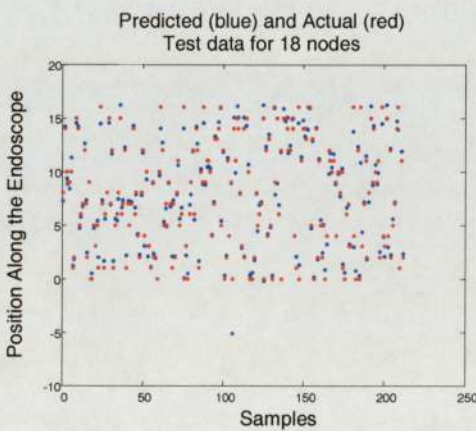


**Figure 6.17**, Predicted and Actual Test Data for Position determination

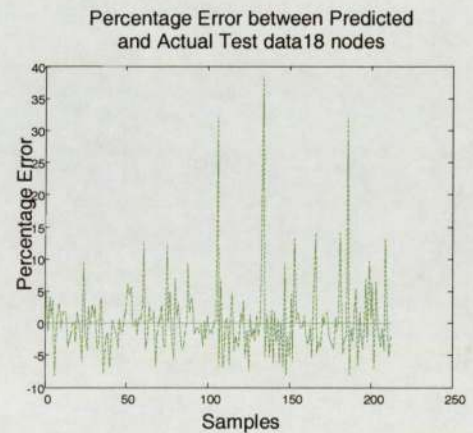


**Figure 6.18**, Percentage Error between the Actual and Predicted Test Data

We can also establish a relation between the data sets by determining the correlation coefficient. This coefficient effectively determines the correlation between the two sets in terms of a value between 0 and 1; 0 signifying very little correlation, and 1 as a perfect correlation between two data sets. The “corr2” command within MATLAB

---

calculates the correlation coefficient between the two data sets. This correlation coefficient is calculated as follows:

$$\varphi = \frac{\sum_m \sum_n (A_{mn} - \bar{A})(B_{mn} - \bar{B})}{\sqrt{(\sum_m \sum_n (A_{mn} - \bar{A})^2)(\sum_m \sum_n (B_{mn} - \bar{B})^2)}} \quad [27]$$

where  $\varphi$  is the correlation coefficient,

$A$  is the test output generated by the Neural Network

$B$  is the actual test output

$\bar{A}$  is the mean of  $A$

$\bar{B}$  is the mean of  $B$

Essentially this gives us a valid representation of the overall error between the two data sets as a percentage. For the test data collected, and for the network with 18 hidden nodes, and a learning gradient of  $10^{-8}$ , the correlation coefficient is found to be 0.9823, which corresponds to a 98.23 % accuracy. This suggests that the system is extremely reliable at discriminating location of point loads along the surface of the flexible digit. In fact, it could be considered robust at predicting palpations along an endoscope over time, if low enough frequencies are considered. The accuracy of the predictions, however, would be expected to be reduced with an activated system. The same procedures have been duplicated in **Chapter 7** for the actuated system.

The sensitivity of the system could be improved even further by considering full bridge configurations for the strain gauges. However, it might not even be necessary, as the accuracy is already extremely high. The question arises: will the accuracy of the predictions be reduced substantially when dealing with higher sampling frequencies? In addition, it would be interesting to determine if the network could be optimized even further to identify features acting on its member, and possibly even discriminate against stiffness variations. These studies could be carried out in the future.

---

## 6.10 Discussion

It has been shown that network networks can predict quite accurately position of a load along the flexible digit when it's non-actuated. This has indicated that the system could be optimized to detect palpations over time at low frequencies with activation. The accuracy of the predictions, however, would be expected to be reduced when activated.

It has also been shown that the system exhibits linear characteristics, which become apparent during training of the network with the lack of a local minimum.

---

## Chapter 7

### 7 Tactile Sensing of the Actuated Digit

The following Chapter describes the method of using sensors positioned along the steerable, cable-activated system as tactile sensing points. Unlike the methods in **Chapter 6**, however, information has been derived from the sensing points while the actuation of the digit has been enabled. The information from these sensors is used to predict the position of an applied load to the digit using a neural network.

The actuation adds an extra element of stiffness to the system which is produced from the cable tension. The cable tension and hence the stiffness is also increased as weights are loaded onto the digit. The system stiffness therefore is not constant, as the weights as well as the actuation affect it. Although this stiffness will affect the accuracy of the predictions to some extent, the difference in accuracies between the actuated and non-actuated system's neural networks is expected to be minimal. Besides neural networks are designed to predict non-linear systems and therefore should not have any difficulty with the predictions of the variable stiffness system.

In addition, the stiffness affects the sensitivity of the system. A higher stiffness implies that the digit will no longer be able to deflect as it did with the non-actuated system and lower weights. Consequently the digit will therefore not be able to exhibit the same sensitivity to these lower loads, and the weights used for the non-actuated system could not be used during the actuated experimental procedures.

One of the concerns of applying point loads to the actuated system is that the system was designed to operate in a vertical fashion. Horizontally, the digit deflects with its own weight. This horizontal arrangement coupled with the attached cable will also affect the stiffness of the system. The cable will therefore be initially tensed by the weight of the digit.

---

Another concern is the possibility of non-linearity's included in the system from the deflections exceeding the small angle deflection's assumption. The maximum actuated deflections are slightly in excess of  $30^\circ$ . The linearity will therefore be reduced, as the system is considered linear up to the  $30^\circ$  mark. This reduction in linearity could perhaps also lower the accuracy of the predicted results.

---

## 7.1 Experimental Explanation

As explained in Section, for a neural network to be able to predict the outputs based on the predetermined inputs, it is necessary to acquire a decent amount of data. The experimental data collection was carried out in a similar fashion to the non-actuated system. However, only two different weights were hung along the flexible digit, whereas for the non-actuated system there were three. Each weight was positioned at ten different positions along the digit and at three different actuation levels. In addition, the procedure was completed twenty-five times at each position and weight, producing 1500 data points for training, validation, and testing of the neural network.

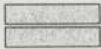
The sensor data was collected from six  $120\ \Omega$  strain gauges ( $GF \approx 0.8$ ) positioned along the flexible digit as shown in **Figure 1.1**. The strain gauges were combined into three pairs connected in half bridge configurations, and produced resistance changes as the flexible digit was deflected. The leads of the strain gauges were then connected to a Fylde FE-366-TA amplifier with an internal low-pass filter set to a cut-off frequency of 470 Hz. The amplifier converted the resistance change to a useful voltage reading. The three voltage readings were then read into MATLAB through the PCI-DAS1602/16 data acquisition card.

---

## 7.2 Load Positions and Weights

As explained previously, two different loads were positioned along the length of the flexible digit. These point loads were categorized as 25 g, and 37.5 g weights. Each weight was positioned along the beam in ten different positions as show in **Figure 7.2**. In addition, the motor was actuated by providing serial commands of 0, 20, and 40. Position #1 is considered to be at the tip of the flexible digit, and each of the positions are 2 cm apart from one another.

The loads are categorized as in **Figure 7.1**. The first set of test data relied on taking two lead weights, each weighing 12.5 g, and positioning them at the ten positions and at the three motor actuation levels. The second data set used three 12.5 g lead weights, and once again positioned along the endoscope at the ten positions and at the three motor actuation levels. The sensor outputs were measured for all loaded positions, weights, and actuation levels twenty-five times to ensure repeatability results. In addition, a no load condition was measured at the start of every test. This could assist in the determination of the load/no load and load magnitude prediction networks.

	
Double Load (Lead) Load 1 (25 g)	Triple Load (Lead) Load 2 (37.5 g)

*Figure 7.1, Load Configurations*

**Table 7.1, Position and Load Combinations**

Position of load from the tip of the flexible digit	Load Type
0	Load 0 (No Load)
1 (0 cm)	Load 1 & Load 2
2 (2 cm)	Load 1 & Load 2
3 (4 cm)	Load 1 & Load 2
4 (6 cm)	Load 1 & Load 2
5 (8 cm)	Load 1 & Load 2
6 (10 cm)	Load 1 & Load 2
7 (12 cm)	Load 1 & Load 2
8 (14 cm)	Load 1 & Load 2
9 (16 cm)	Load 1 & Load 2
10 (18 cm)	Load 1 & Load 2

**Note:** The distance is measured from tip of flexible digit

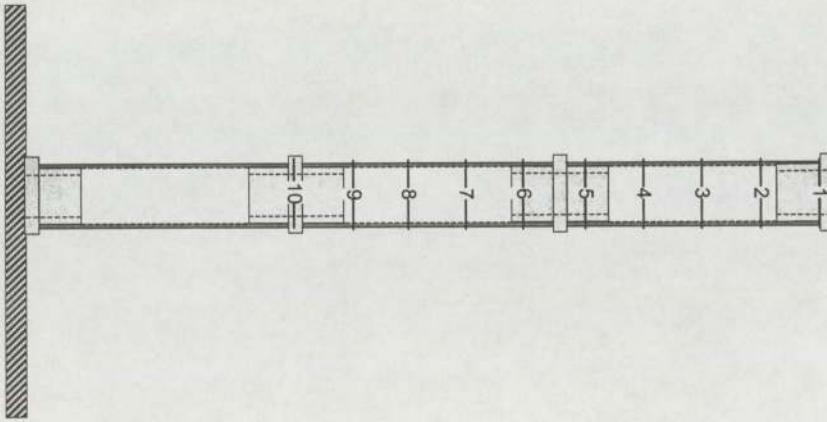


**Figure 7.2, Load positions along the Flexible Digit**

---

### 7.3 Data Normalization

As explained in **Section 6.6**, it is essential that the data be normalized to avoid the chance of the training network getting stuck on a local optimum. The mean and the variance of the training data is determined using **(E 6. 1)**, and all training, validation, and test data components normalized to this mean and variance. The data values are then randomized and separated into the training data components ( $\frac{1}{2}$  of the data), validation data components ( $\frac{1}{3}$  of the data), and test data components (the remaining  $\frac{1}{6}$  of the data).

**Figure 7.3** shows the data from the three strain gauge sensors for both weights in its non-normalized form. We can see that the data demonstrates essentially a linear pattern for specific weights as they are moved along the digit. This indicates that the variability in the stiffness due to the weight position is minimal and does not affect the system terribly. Therefore we expect the training of the neural network to act like a linear system.

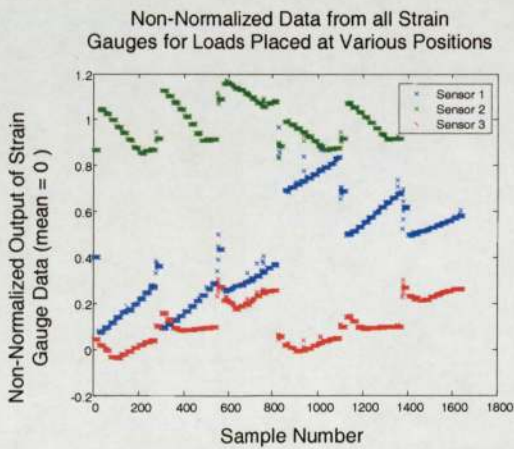


**Figure 7.3**, Non-Normalized data for all the strain gauges, loads, and load position

---

## 7.4 Training the Neural Network

As explained in **Section 6.8**, the neural network is created using the training and validation data. Weights and biases are produced from the actual data using a feed-forward method. Matching the actual data is the network target. The calculated network coefficients are then used to confirm the validity of the network against the actual data by determining the validation error.

Based on **Figure 7.4**, we notice that the system exhibits linear behavior as the validation error does not reach a local minimum or early stopping point. The lack of this minimum indicates that the input data is stable and extremely close to the training data as the error converges to a specific value. The linearity of the network was introduced in **Section 6.6**, and supported in **Section 7.3** even with the inclusion of the non-linear stiffness.

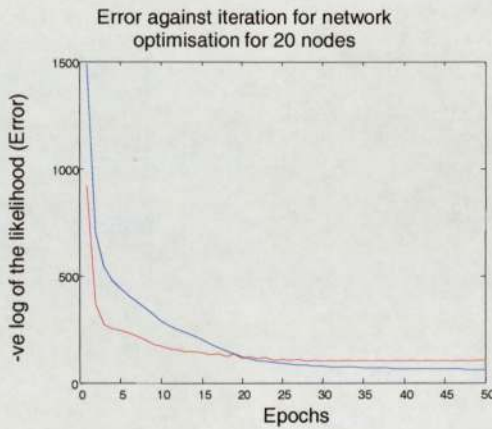


**Figure 7.4**, Error against iterations for 20 nodes, 50 epochs

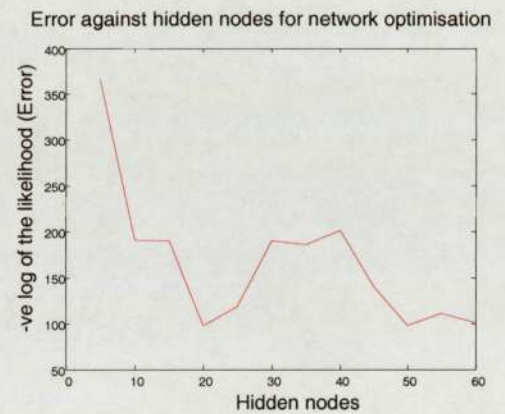


**Figure 7.5**, Error for 5 to 60 hidden nodes

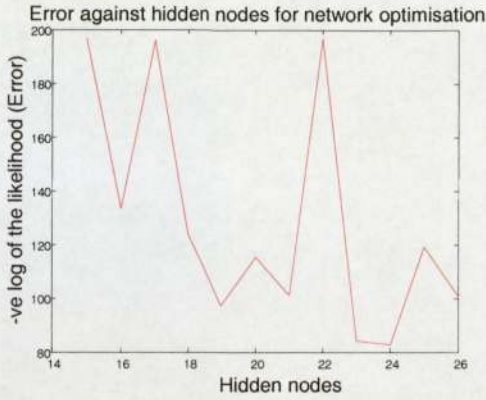


**Figure 7.6,** Error for 15-25 hidden nodes

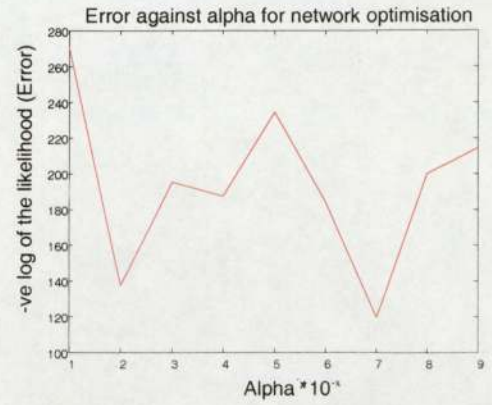


**Figure 7.7,** Error for Learning Gradient between  $10^{-1}$ - $10^{-9}$

The first optimization cycle calculated the training errors for networks with 5 to 60 hidden nodes, in five node increments. We can see from **Figure 7.5** that the optimum number of hidden nodes following the optimization procedure has been determined as being somewhere between 15 and 25. The training procedure is therefore repeated for 15 to 25 nodes in one node increments (see **Figure 7.6**). The optimization procedure has shown that the lowest error occurs with 24 hidden nodes. This is very similar to the optimum number of hidden nodes for the non-actuated system.

The next step was to vary the power of the learning gradient, which had been set by default to  $10^{-7}$  previously. The learning gradient was then varied from  $10^{-1}$  to  $10^{-9}$  while keeping the hidden nodes constant at 24. The optimum learning gradient is found to be  $10^{-7}$  (see **Figure 7.7**). This information is now used for the testing of the neural network.

---

## 7.5 Testing of the Optimized Network

This next section uses the information from the neural network derived in **Section 7.4** to measure the accuracy of the predicted results. The input test data is fed into the neural network and output data is generated. The number of hidden nodes and learning gradient determined by the training and validation optimization procedures are used with the test input data to generate predicted test output data. The resulting prediction is then compared with the actual test data. The two data sets were plotted against each other as shown in **Figure 7.8**. The red points are the actual test points, whereas the blue are the predicted data from the neural network. Similar to the non-actuated correlation plots, it is hard to distinguish between output points. The percentage error plot in **Figure 7.9** demonstrates more clearly the percentage error between the actual and predicted systems. As shown, the percentage error between the two generally lies under 15%, with the exception of a few, thus indicating decent matching of the two data sets.

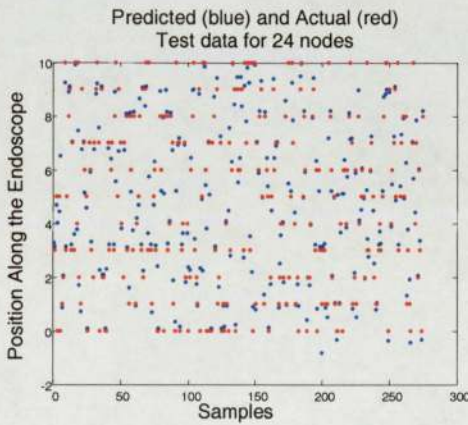


**Figure 7.8,** Predicted and Actual Test Data for Position determination

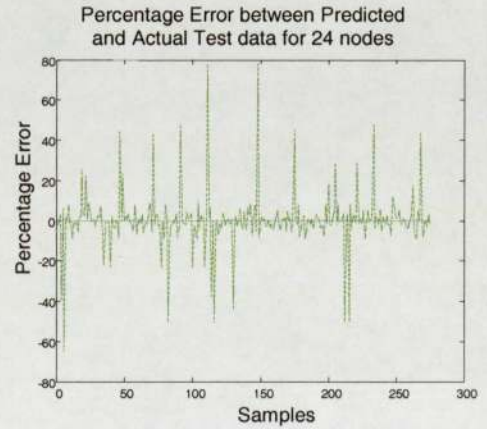


**Figure 7.9,** Percentage Error between the Actual and Predicted Test Data

---

This correlation coefficient between the actual and predicted test data is calculated as demonstrated in Section. Recall that:

$$\varphi = \frac{\sum_m \sum_n (A_{mn} - \bar{A})(B_{mn} - \bar{B})}{\sqrt{(\sum_m \sum_n (A_{mn} - \bar{A})^2)(\sum_m \sum_n (B_{mn} - \bar{B})^2)}} \quad [27]$$

This coefficient provides a valid representation of the overall accuracy between the two data sets expressed as a percentage. For the test data collected, and for the network with 24 hidden nodes, and a learning gradient of  $10^{-7}$ , the correlation coefficient is found to be 0.8998, which corresponds to a 89.98 % accuracy between the predicted and actual systems. This correlates to a decrease in accuracy from the non-actuated system of about 9%, suggesting that the system is still extremely reliable at discriminating the location of point loads along the surface of the flexible digit. And, just as with the non-actuated system, the neural network could be considered robust at predicting palpations along the flexible digit over time, if low enough frequencies are considered.

The network has therefore demonstrated that it has the ability to discriminate against stiffness variations without much reduction in the accuracy of the results. As the accuracy is still apparent in the predictions, the results derived from the actuated system emphasize the redundancy of the sensor positions. These results also ensure that the actuated system is reliable and robust for a variety of non-ideal situations. The flexible digit's ability to excel in these situations makes it ideal for medical use.

As presented in **Section 6.9**, the sensitivity of the system could be improved even further by considering full bridge configurations for the strain gauges. In addition, the network could be geared towards identifying features acting on its member. This could provide an extra sense of feature detail back to the surgeon. These studies could be carried out in the future.

---

## 7.6 Discussion

The accuracies achieved for the actuated system demonstrates that even with non-linearity's introduced into the system, it can still operated with extremely acceptable results. This could prove quite beneficial when dealing with an optimized system that discriminates against load width, and variability in the stiffness of the detected objects.

In the detection and prediction of the endoscopic system, it might be undesirable to eliminate certain behavior types over others. This is where a neural network could shine, as it has demonstrated its potential to excel in bio-medical applications, which consists primarily of non-ideal situations. This holds an incredible advantage over machine use which is predictable and ideal.

---

## Chapter 8

### 8 Conclusion

This thesis has presented the design, the manufacturing, and implementation of the cable actuated flexible digit with novel tactile feedback. A brief literature review of smart sensing techniques used in minimally invasive surgical tools was presented (**Chapter 1**), followed by the design of the physical system (**Chapter 2**). The device was designed to mimic a three section flexible digit capable of predicting loads. Strain gauges were used as tactile feedback to measure the digit's deflection. Each of the components of the system were modeled (**Chapter 3**) so that a robust controller could be designed (**Chapter 4**). The controller which differs from existing systems by using the deflection of the member as feedback was digitized, so that it could be integrated within software (**Chapter 5**). Although the computational ability of the provided computer proved inadequate for the required sampling time, the controller proved to be theoretically effective at controlling the digit over the desired frequencies. The system's ability to predict and discriminate load positions was also examined using neural networks. This was performed initially for a non-actuated system (**Chapter 6**), followed by an actuated system (**Chapter 7**).

Although the system demonstrated an acceptable stability, there still exist a few issues that need to be addressed. A sensitivity and stability analysis should be conducted into the effects of all system parameters. This would certainly assist with the understanding of future systems. The devices should also be redesigned to incorporate feedback of all three strain gauges, and increase the motor step resolution. Most importantly, an appropriate software platform for integration of the digital controller should be used to avoid latency and data acquisition issues.

The benefits of the neural network are exemplified with their ability to predict highly non-linear systems found in bio-medical applications. The accuracy achieved from both non-actuated and actuated neural networks indicate that the system could be optimized to detect low frequency palpations, to identify variability in tissue stiffness, and to discriminate against distributed loads.

---

In summary a predictive tool in measurement and detection of surface loads has been developed which mimics existing minimal invasive surgical motions. Much work remains to be done to the device before incorporating it in the operating room. However, the findings of the thesis look promising for future development.

---

## References

- [1] Mark H. Lee, "*Tactile Sensing: New Directions, New Challenges*", The International Journal of Robotics Research, pp 636-637, July 2000.
- [2] István Nagy, Hermann Mayer, Alois Knoll, "*The Endo[PA]R System for Minimally Invasive Robotic Surgery*", Paper from the Institute for Information, TUM-INFO-12-I0320-0/1.-FI, pp 1-8, 2003.
- [3] Lee, M. H., Nicholls, "*Tactile sensing for Mechatronics – state of the art survey*", Mechatronics 9, H. R., pp 1-31, 1999.
- [4] <http://www.tekscan.com/medical/catalog.html>, 2004.
- [5] X. Ma and P. Brett, "*The performance of a 1-D Distributive Tactile Sensing System for Detecting the Position, Intensity and Width of a Contacting Load*", IEEE Trans. On Instrumentation and Measurement, vol 51(2), pp. 331-336, April 2002.
- [6] X. Ma and P.N. Brett, "*A novel distributive tactile sensing technique for determining the position, width and intensity of a distributed load*", IEEE Trans. on Instrumentation and Measurement Systems, vol. 51, no. 2, pp311-336, April 2002.
- [7] Brett, P.N., Stone, "*A technique for measuring contact force distribution in minimally invasive surgical procedures*", R.S.W., Proc. IMechE, Part H, No. H4, Vol. 211, 1997.
- [8] P. Tongpadungrod, D. Rhys and P.N. Brett, "*An approach to optimize the critical sensor locations in one-dimensional novel distributive tactile surface to maximise performance*", Int. Journal. of Sensors and Actuators, vol. 1, no. 105, pp.47-54, June 2003.
- [9] P. Dario, B. Hannaford, and A. Menciassi, "*Smart surgical tools and augmenting devices*", IEEE Transactions on Robotics and Automation, vol. 19, pp. 782-792, 2003.
- [10] R. H. Taylor and D. Stoianovici, "*Medical robotics in computer-integrated surgery*", IEEE Transactions on Robotics and Automation, vol. 19, pp. 765-781, 2003.
- [11] F. Tendick, S. Sastry, R.S.Fearing, and M.Cohn, "*Applications of micromechatronics in minimally invasive surgery*", IEEE/ASME Transactions on Mechatronics, vol. 3, pp. 34-42, 1998.
- [12] K. J. Robello, "*Applications of MEMS in Surgery*", Proceedings of the IEEE, vol. 91, pp. 43-55, 2004.

- 
- [13] R. D. Howe, W. J. Peine, D. A. Kantarinis, and J. S. Son, "Remote Palpation Technology", IEEE Engineering in Medicine and Biology Magazine, vol. 14, pp. 318–323, 1995.
- [14] E. P. Scilingo, D. De Rossi, A. Bicchi, and P. Iaconi, "Sensors and devices to enhance the performances of a minimally invasive surgery tool for replicating surgeon's haptic perception of the manipulated tissues", Proceedings of IEEE International Conference on Engineering in Medicine and Biology society, pp. 961–964, 1997.
- [15] A. Bicchi, G. Canepa, D. De Rossi, P. Iaconi, and E.P.Scilingo, "A sensorized minimally invasive surgery tool for detecting tissutal elastic properties", Proceedings of IEEE International Conference on Robotics and Automation, pp. 884–888, 1996.
- [16] P.Dario, M.C. Carrozza, M. Marcacci, S. D'Attanasio, B. Magnami, O. Tonet, and G. Megali, "A Novel Mechatronic Tool for Computer-Assisted Arthroscopy", Proceedings of IEEE International Conference on Engineering in Medicine and Biology society, pp 15-29, 2000.
- [17] S. D'Attanasio, O. Tonet, G. Megali, M. C. Carrozza, and P. Dario, "A semiautomatic handheld mechatronic endoscope with collision-avoidance capabili-References 49 ties", Proceedings of IEEE International Conference on Robotics and Automation, pp. 1586–1591, 2000.
- [18] B K Y Tam, "A Novel Tactile Sensing Digit for use in Clinical Applications ", PhD Thesis, Birmingham: Aston University, December, 2004.
- [19] K Hoffmann, "The Strain Gauge; a Universal Tool of the Experimental Stress Analysis", Hottinger Baldwin Messtechnik, pp 4-10.
- [20] Ferdinand P. Beer, E Russell Johnston Jr., "Mechanics of Materials, Second Edition", McGraw Hill, Singapore, 1992.
- [21] Richard C. Dorf, Robert H. Bishop, "Modern Control Systems – Ninth Edition", Prentice Hall, Upper Saddle River, 2000.
- [22] Daniel Liberzon, A. Stephen Morse, Eduardo D. Sontag, "Output–Input Stability and Minimum-Phase Nonlinear Systems", IEEE Transactions on Automatic Control, Vol 47, No 3, March 2002.
- [23] K. Zhou, J.C Doyle, "Essentials of Robust Control", Prentice Hall, pp 129-161, 1997.
- [24] Chi-Tsong Chen, "Analog and Digit Control System Design: Transfer-Function, State-Space, and Algebraic Methods", Saunders College Publishing, Fort Worth, 1993.

- 
- [25] B. Cowie, D.J. Webb , B.K.Y Tam, P.S Slack, P.N. Brett, "Fibre Bragg grating and resistive strain gauges for tactile sensing: a comparison", to be presented at OFS (Optical Fibre Sensors Conference), 2005.
- [26] Ian T. Nabney, "*Netlab Algorithms for Pattern Recognition*" , Springer, 2002, pp 29-30.
- [27] Image Processing Toolbox – Preliminary Documentation, Mathworks Inc, 2004.
- [28] Maxon Precision Motors, Inc., 2003/2004 Catalogue, pp 1-219, 2004.
- [29] "*Multifunction Analog and Digital I/O Board – User Manual*", Revision 3, Measurement Computing Corporation, August, 2001.

---

## Appendix A: Nomenclature

$e$	:	Tension Eccentricity
$m$	:	Mass of the Digit Element
$l$	:	Length of Flexible Digit
$\Delta l_M$	:	Change in Cable Length
$r_m$	:	Inertial Disc Radius
$r_M$	:	Radius of Cable Attachment Point on Motor Pulley
$t$	:	Time
$w$	:	Distributed Weight of Digit
$\omega_n$	:	Natural Frequency
$x$	:	Position along the Flexible Digit
$y$	:	Deflection
$A$	:	Cross Sectional Area
$E$	:	Modulus of Elasticity
$E(s)$	:	Flexible Digit's Transfer Function
$F(s)$	:	Filter Transfer Function
$G(s)$	:	Plant Transfer Function
$G_{CL}(s)$	:	Closed Loop Transfer Function
$GF$	:	Gauge Factor
$I$	:	Moment of Inertia of Digit
$J_{disc}, J_L$	:	Disc Inertia
$J_M$	:	Motor Rotor Inertia
$K(s)$	:	Controller Transfer Function
$K1$	:	Motor Deflection to Serial Command Coefficient
$K2$	:	Angular to Bending Moment Coefficient
$K3$	:	Digit Deflection to Digit Deflection Coefficient
$K_{EM}$	:	Motor Back EMF Constant
$K_{DM}$	:	Motor Internal Damping Coefficient
$K_{TM}$	:	Motor Torque Constant
$L_{AM}$	:	Motor Armature Inductance

---

$M$	:	Applied Moment
$MT(s)$	:	Motor Transfer Function
$N$	:	Gear Ratio
$N_1$	:	Number of Teeth of Motor Gear
$N_2$	:	Number of Teeth of Inertial Disc Gear
$P$	:	Applied Force
$R$	:	Resistance in Wheatstone Bridge
$R_{AM}$	:	Motor Armature Resistance
$\delta R$	:	Change in Resistance
$\delta S$	:	Change in Strain
$T_g, T_1$	:	Inertial Disc Gear Torque
$T_m, T_2$	:	Motor Gear Torque
$T_s$	:	Settling Time
$V$	:	Shear Force
$V_a$	:	Motor Applied Voltage
$V_m$	:	Measure Voltage from Wheatstone Bridge
$V_s$	:	Supply Voltage to Wheatstone Bridge
$V_Y, V_{SG}$	:	Strain Gauge Voltage
$V_\theta$	:	Motor Potentiometer Voltage
$\beta$	:	Rotation Angle of Digit
$\varepsilon$	:	Measured Strain from Wheatstone Bridge
$\zeta$	:	Damping Coefficient
$\theta_m$	:	Angular Position of Motor
$\theta_2$	:	Angular Position of Inertial Disc Gear
$\omega_m$	:	Angular Velocity of Motor
$\lambda_G$	:	Eigenvalues of the Plant Model
$\eta$	:	Efficiency
$\rho_m$	:	Material Density
$\rho_c$	:	Radius of Curvature of Digit

---

- 
- $\rho_e$  : Radius of Curvature of Cable  
 $\chi_{mpss}$  : Motor Serial Command

### LTI System Variables

- $P$  : Nominal System  
 $C$  : Controller of LTI system  
 $T_{uw}$  : Transfer Function of Control Input to Disturbances  
 $T_{pq}$  : Transfer Function of Uncertainty Output to Input  
 $T_{yw}$  : Transfer Function of Measurements to Disturbances  
 $T_{zw}$  : Transfer Function of Uncertainty Controller Variable to Disturbances  
 $\gamma$  :  $H_{\infty}$  Criterion Coefficient  
 $z$  : Regulated or Controlled Variable  
 $y$  : Measurements  
 $u$  : Control Input  
 $w$  : Sources of Disturbance  
 $q$  : Uncertainty Input  
 $p$  : Uncertainty Output  
 $\Delta$  : Uncertainty Model

# Appendix B: Flexible Digit Mechanical Drawings

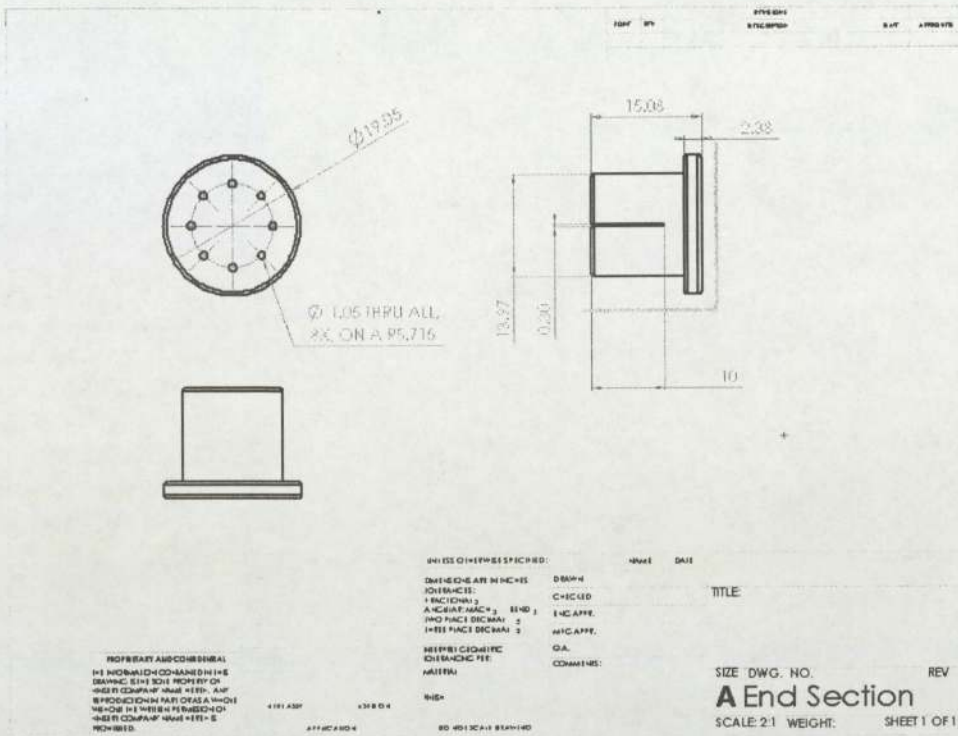


Figure B.1, End Section

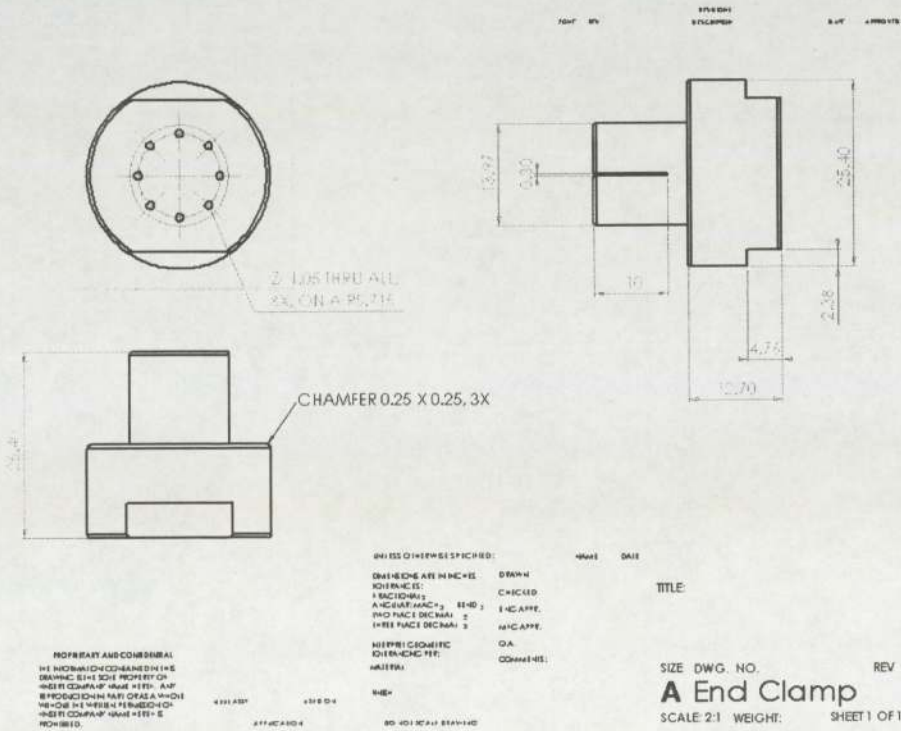


Figure B.2, End Clamp

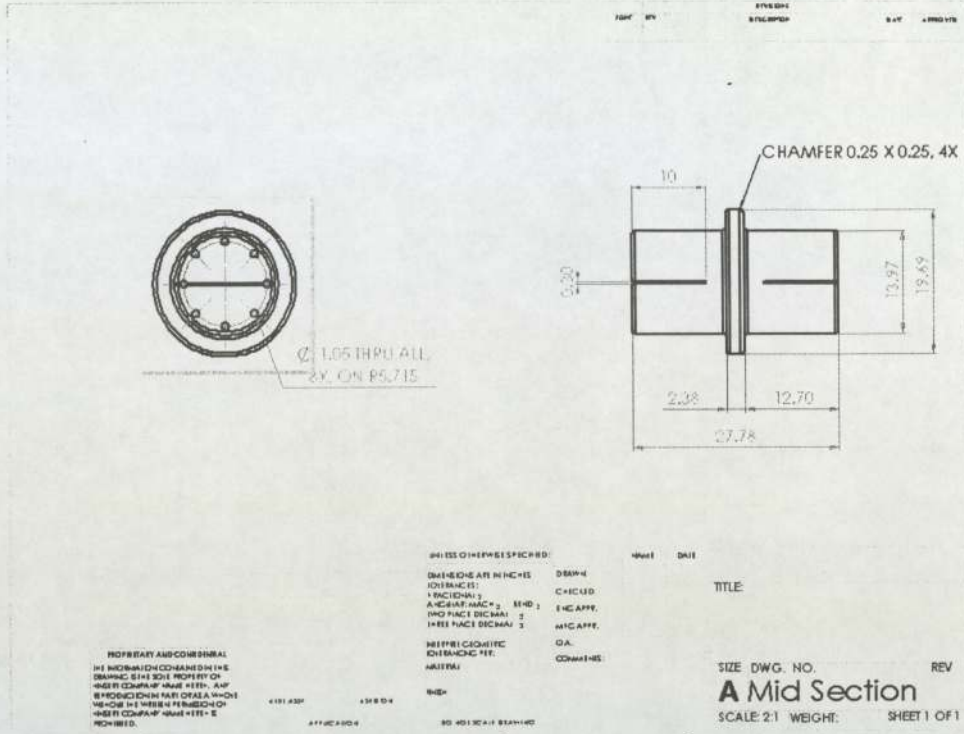


Figure B.3, Mid Section

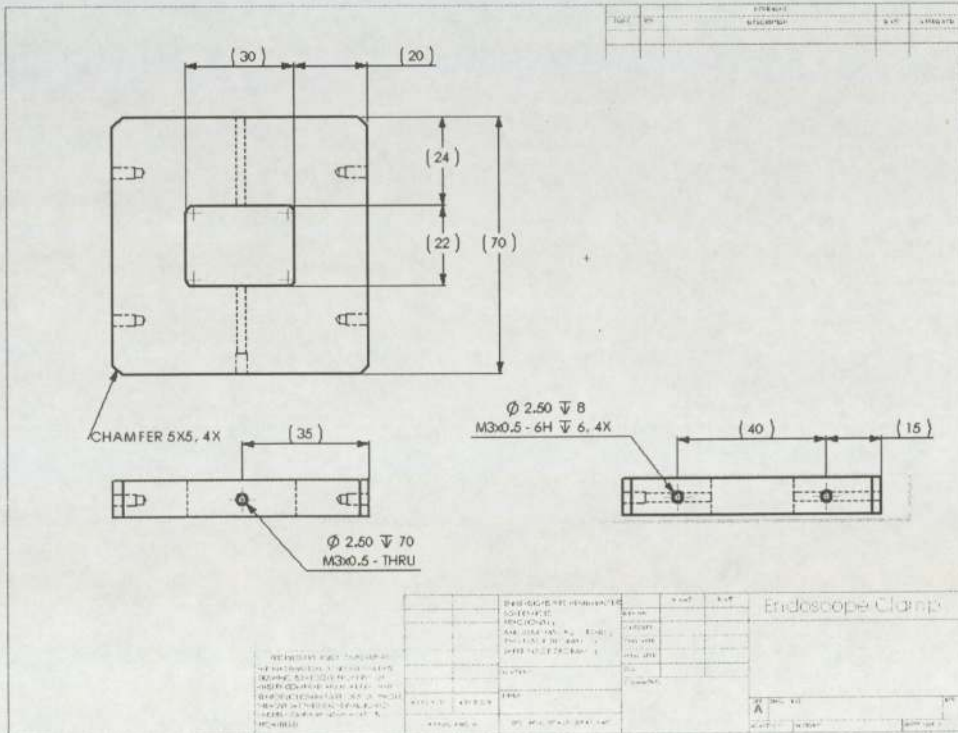


Figure B.4, Mounting Base

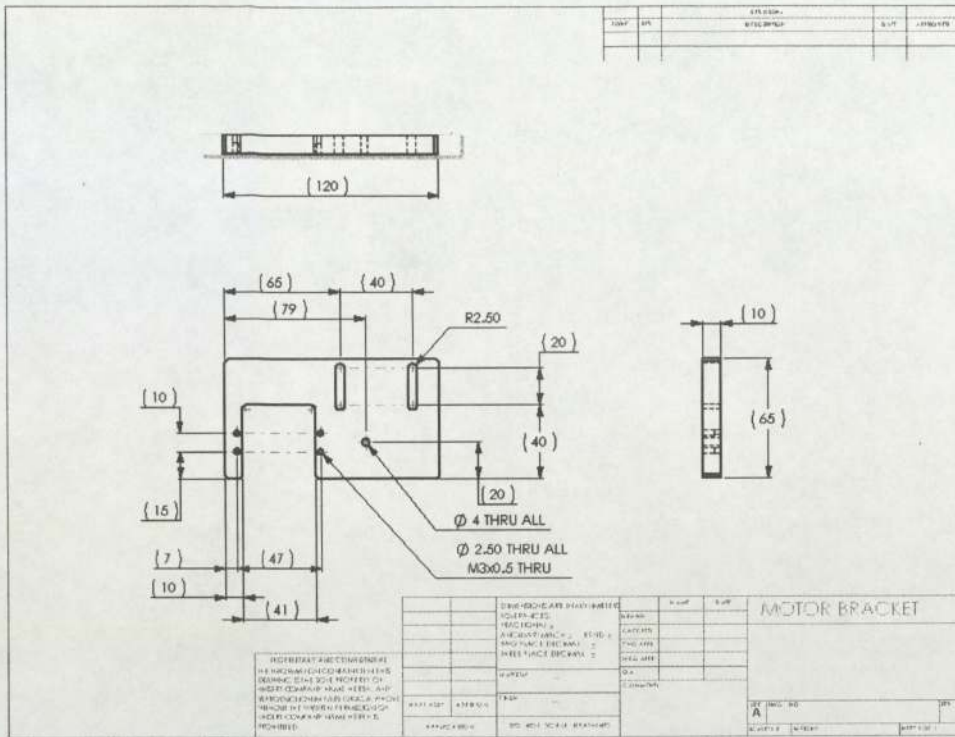


Figure B.5, Motor Bracket

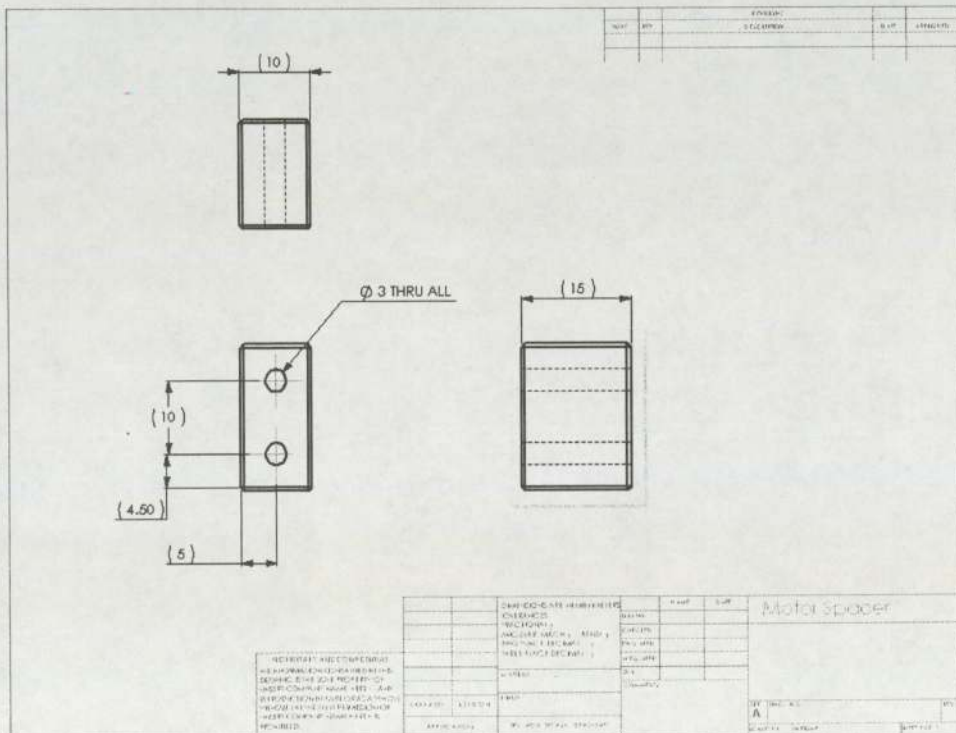


Figure B.6, Motor Spacer

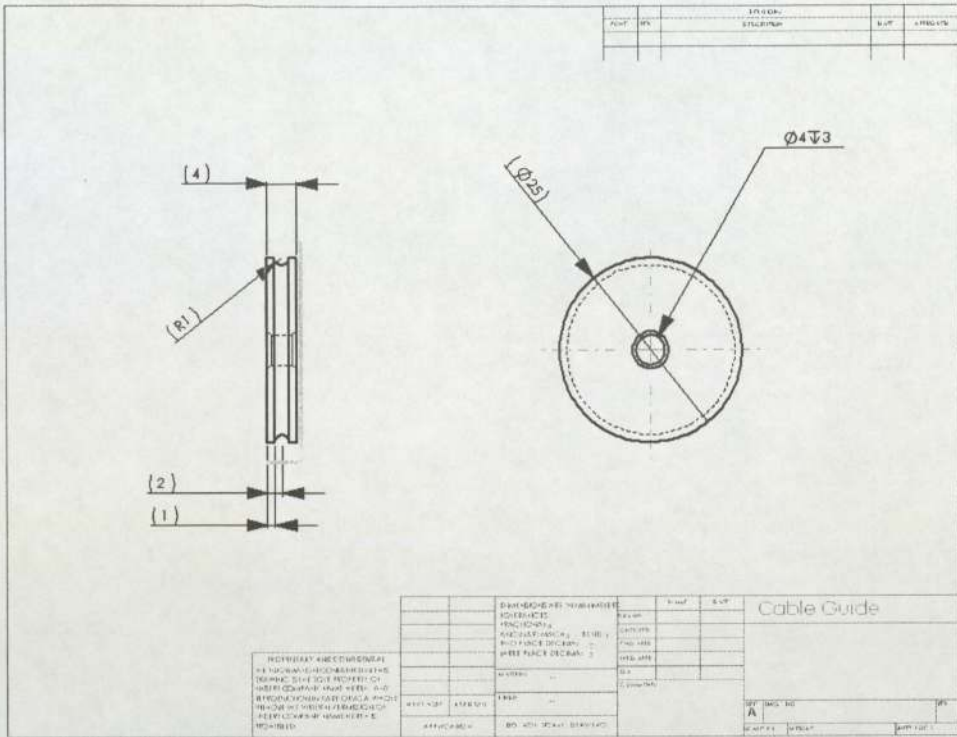


Figure B.7, Cable Guide

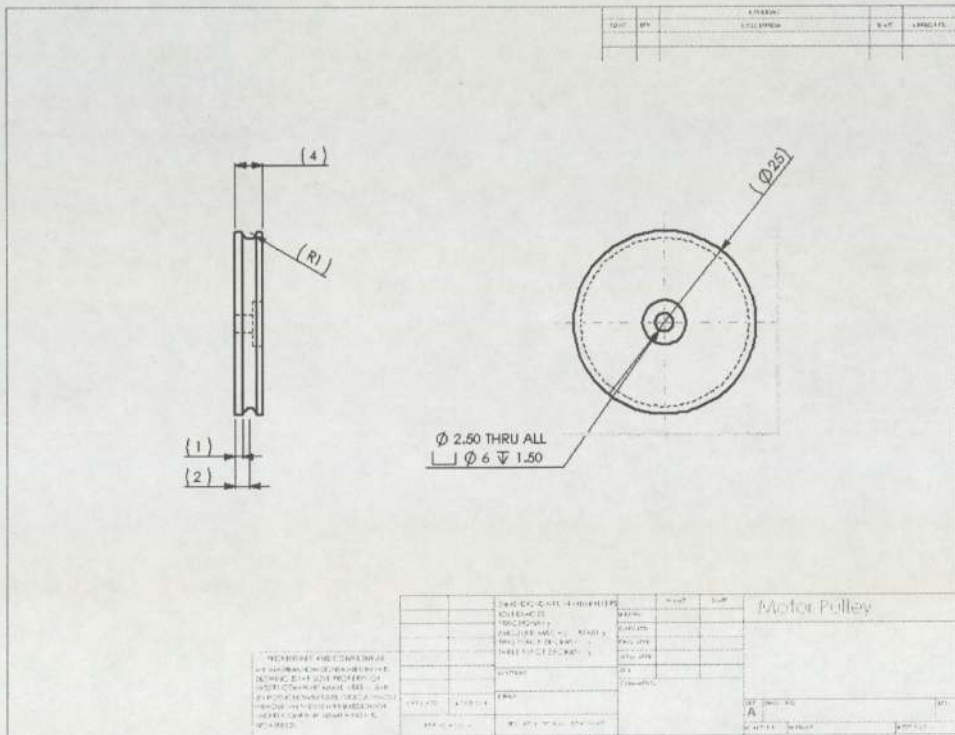


Figure B.8, Motor Pulley

---

## Appendix C: Alternative Motor Selection

The Maxon motor and its components would fulfill the requirements of the flexible digit system. However, in addition, we would require a power driver circuit, a method of retrieving the feedback from the shaft encoder, as well as software position control.

---

### DC Motor

A-Max 26  
Shaft Diameter: 3mm  
Motor Size: 26mm  
Nominal Voltage: 12V  
Maximum Continuous Torque: 17 mNm  
P/N 110209  
pp 116

---

---

### Shaft Encoder

HEDS 55\_  
Counts Per Turn: 500  
No. of Channels: 2+1  
3mm Dia shaft  
P/N 110511  
pp 217

---

---

### Planetary Gearhead

Sample Calculation(with safety Factor 10):  
 $(10 * 0.981 * 10^3) / 17 \text{mNm} = 577:1$  ratio  
GP 26 B  
Gearhead Size: 26mm Dia  
Gearhead Shaft: 4.5mm Dia  
Gearhead Ratio: 690:1  
P/N 144058  
pp 193

---

[28]

## Appendix D: PCI-DAS1602/16 Connector Diagram

Analog Ground	1	● ●	51	Digital A0
Analog Input Ch 0 High	2	● ●	52	Digital A1
Analog Input Ch 0 Low / 8 High	3	● ●	53	Digital A2
Analog Input Ch 1 High	4	● ●	54	Digital A3
Analog Input Ch 1 Low / 9 High	5	● ●	55	Digital A4
Analog Input Ch 2 High	6	● ●	56	Digital A5
Analog Input Ch 2 Low / 10 High	7	● ●	57	Digital A6
Analog Input Ch 3 High	8	● ●	58	Digital A7
Analog Input Ch 3 Low / 11 High	9	● ●	59	Digital B0
Analog Input Ch 4 High	10	● ●	60	Digital B1
Analog Input Ch 4 Low / 12 High	11	● ●	61	Digital B2
Analog Input Ch 5 High	12	● ●	62	Digital B3
Analog Input Ch 5 Low / 13 High	13	● ●	63	Digital B4
Analog Input Ch 6 High	14	● ●	64	Digital B5
Analog Input Ch 6 Low / 14 High	15	● ●	65	Digital B6
Analog Input Ch 7 High	16	● ●	66	Digital B7
Analog Input Ch 7 Low / 15 High	17	● ●	67	Digital C0
Analog Ground	18	● ●	68	Digital C1
NC	19	● ●	69	Digital C2
NC	20	● ●	70	Digital C3
NC	21	● ●	71	Digital C4
NC	22	● ●	72	Digital C5
NC	23	● ●	73	Digital C6
NC	24	● ●	74	Digital C7
NC	25	● ●	75	NC
NC	26	● ●	76	NC
NC	27	● ●	77	NC
NC	28	● ●	78	NC
NC	29	● ●	79	NC
NC	30	● ●	80	NC
NC	31	● ●	81	NC
NC	32	● ●	82	NC
NC	33	● ●	83	NC
NC	34	● ●	84	NC
D/A GND 0	35	● ●	85	NC
D/A OUT 0	36	● ●	86	NC
D/A GND 1	37	● ●	87	NC
D/A OUT 1	38	● ●	88	NC
CLK 4	39	● ●	89	PC Ground
GATE 4	40	● ●	90	PC +12V
OUT 4	41	● ●	91	PC Ground
A/D External Pacer	42	● ●	92	PC -12V
Analog Trigger In	43	● ●	93	NC
D/A External Pacer	44	● ●	94	NC
A/D External Trigger	45	● ●	95	A/D Internal Pacer Output
NC	46	● ●	96	D/A Internal Pacer Output
NC	47	● ●	97	External D/A Pacer Gate
PC +5V	48	● ●	98	NC
SSH OUT	49	● ●	99	External Interrupt
PC Ground	50	● ●	100	PC Ground

Figure D.1. PCI-DAS1602/16 Connector Diagram [29]

---

## Appendix E: Trapezoidal Method

The following demonstrates the transformation of a controller of degree 1 using the bilinear or trapezoidal method.

Assume

$$C(s) = \frac{1 + As}{1 + Bs}$$

$$C(z) = \frac{(2 \times A + T)z + (T - 2 \times A)}{(2 \times B + T)z + (T - 2 \times B)} = \frac{U(z)}{E(z)}$$

Multiplying out produces,

$$U(z)[(2 \times B + T)z + (T - 2 \times B)] = E(z)[(2 \times A + T)z + (T - 2 \times A)]$$

Now dividing by  $z$

$$U(z)[(2 \times B + T) + (T - 2 \times B)z^{-1}] = E(z)[(2 \times A + T) + (T - 2 \times A)z^{-1}]$$

Therefore

$$u(k)(2B + T) + u(k-1)(T - 2B) = e(k)(2A + T) + e(k-1)(T - 2A)z$$

$$u(k) = \frac{1}{(2B + T)} [-u(k-1)(T - 2B)z + e(k)(2A + T) + e(k-1)(T - 2A)]$$

Where  $u(k-1)$  is the output of the controller at one time period before the present time.

$e(k-1)$  is the input to the controller at one time period before the present time.

$e(k)$  is the present input to the controller.